CHARACTERIZATION OF SUBSURFACE DNAPL MOVEMENT WITH GROUND PENETRATING RADAR AND INVERSE MULTIPHASE FLOW SIMULATIONS

by

Raymond H. Johnson

A thesis submitted to the Faculty and Board of Trustees of the Colorado School of Mines in partial fulfillment of the requirements for the degree of Doctor of Philosophy (Geological Engineering).

Golden, Colorado

Date_____

Signed:_____
Raymond H. Johnson

Approved:_____
Dr. Eileen P. Poeter
Thesis Advisor

Approved:_____
Dr. John E. McCray
Thesis Co-advisor

Golden, Colorado

Date:_____

_____
Dr. Murray Hitzman
Professor and Head,
Department of Geology
and Geological Engineering

ABSTRACT

The presence of dense non-aqueous phase liquid (DNAPL) source zones in the subsurface is a limiting factor in the remediation of sites affected by the uncontrolled release of DNAPLs. For successful remediation, the distribution of the DNAPL source zone must be characterized and the DNAPL locations in relation to material permeability contrasts at large and small scales will determine the effectiveness of alternative remedial techniques. The goal of this research is to provide the necessary information to determine the best remedial strategies. Four related investigations evaluate the potential for using ground penetrating radar and inverse multiphase flow simulations to characterize subsurface DNAPL movement and identify the strengths and limitations of the procedure. The following four paragraphs are the abstracts from each of those investigations, which are presented in Chapters 2 through 5 of this dissertation.

For accuracy, an iterative Bruggeman-Hanai-Sen (BHS) mixing model with an air/water/sand system must consider which two-material end member (air/sand or water/sand) to use as the matrix. For a given porosity, a new weighted BHS model provides the best match to measured data. Two BHS curves, one with air/sand as the matrix and one with water/sand as the matrix, are weighted based on the water saturation.

Perchloroethylene (PCE) saturations determined from GPR surveys are used as observations for inversion of multiphase flow simulations of a PCE injection experiment, allowing for the estimation of optimal intrinsic permeability values. Synthetic simulations reveal that saturation data alone are sufficient to estimate optimal intrinsic permeability values, but the character and magnitude of error in the saturation data are critical to accurate estimation. The resulting fit statistics and analysis of residuals (observed minus simulated PCE saturations) are used to improve the conceptual models of permeability zones and capillary pressure-saturation relationships. Remaining bias in the residuals is attributed to the violation of assumptions (lack of flat, infinite, horizontal

layers) in the one-dimensional GPR interpretation due to multidimensional influences. However, this bias does not affect the calculation of the optimal permeability values. The effort to improve model fit and reduce residual bias decreases simulation error even for an inversion based on biased observations. This effort is thus warranted and provides information on bias in observation data when this bias is otherwise difficult to assess.

Ground penetrating radar (GPR) is used to track a DNAPL injection in a laboratory sand tank. Before data reduction, GPR data provide a qualitative measure of DNAPL saturation and movement. One-dimensional (1D) GPR modeling provides a quantitative interpretation of DNAPL volume within a given thickness during and after the injection. This is confirmed qualitatively by visual inspection of cores and two-dimensional GPR modeling. DNAPL saturation in sub-layers of that thickness could not be quantified because calibration of the 1D GPR model is non-unique when both permittivity and depth of multiple layers are unknown. Accurate quantitative interpretation of DNAPL volumes using 1D GPR modeling requires: 1) identification of a suitable target that produces a strong reflection and is not subject to any multidimensional interference; 2) knowledge of the exact depth of that target; and 3) use of two-way radar-wave travel times through the medium to the target to determine the permittivity of the intervening material, which eliminates reliance upon reflection amplitude. With geologic conditions that are suitable for GPR surveys (i.e., shallow depths and low electrical conductivities), the procedures in this laboratory study can be adapted to a field site to identify DNAPL source zones after a release has occurred.

A laboratory-scale DNAPL injection is monitored using ground penetrating radar (GPR). Saturation of DNAPLs, determined using the GPR data, provides calibration data for multiphase flow simulations. This paper investigates the value of GPR-derived DNAPL saturations as observations for inversion of multiphase flow simulations for the purpose of characterizing subsurface heterogeneities. The capillary pressure-saturation function and intrinsic permeability of the #45 Ottawa sand used in the experiment is measured, but the permeability varies over an order of magnitude once it is sifted into a

tank. Inverse multiphase fluid flow simulations are used to estimate intrinsic permeabilities and the resulting fit statistics and analysis of residuals (observed minus simulated DNAPL saturations and observed minus simulated injection rates) are used to improve the conceptual model of permeability heterogeneities. An inverted simulation with homogeneous sand produces a permeability value that is 15% less than the measured vertical permeability. However, the fit statistics and residuals indicate an incorrect conceptual model of permeability. Additional simulations are explored using different conceptual models of permeability zones. These simulations indicate the importance of fine-scaled permeability variations and lead to an improved fit of simulated versus observed DNAPL mass distribution and injection rates. Inversion of the multiphase flow simulation is non-unique with respect to the geometry and permeability values of those zones. These fine-scaled permeability variations are imaged by the GPR data, but the interpretation of the geometry of the zones is non-unique. Future application of GPR and inverse multiphase flow simulations to determine DNAPL flow must include a procedure to minimize this geometry non-uniqueness in order to completely identify smaller-scale permeability contrasts.

TABLE OF CONTENTS

LIST OF FIGURES

LIST OF TABLES

ACKNOWLEDGEMENTS

I acknowledge my advisor, Eileen Poeter, for her guidance and continued scientific advice. In addition, I thank my co-advisor, John McCray, for his input on multiphase flow issues, and the rest of my committee (L. Graham Closs, Ning Lu, and Kadri Dagdelen) for supporting all of my efforts. Assistance from Mike Powers and our discussions of ground penetrating radar theory have been invaluable. I thank Bernard Kueper and Jason Gerhard for providing and assisting me with the use of their multiphase flow code, 3D2PHASE. I also acknowledge Robert Horton for his continued motivational support and the use of his laboratory for making dielectric permittivity measurements. My wife, Anna, provided continued support and was someone I could always count on to listen when my research did not go as planned.

Funding for this project has been provided by the USGS and the U.S. EPA through interagency agreement #DW14936568-01-0. I acknowledge the support and patience of Aldo Mazzella of the U.S. EPA who initiated much of this work. The U. S. Silica Company provided the sand used for this research and Thunderhead Engineering provided PetraSim, a preprocessor for T2VOC that was used for the sand tank multiphase flow simulations.

Chapter 1

INTRODUCTION

1.1 Research Overview

Dense non-aqueous phase liquids (DNAPLs) are often source zones for dissolved constituents in ground water at sites affected by DNAPL contamination. Successful remediation of such sites requires the identification of the DNAPL source zones and the identification of possible pathways for current and/or future DNAPL movement. Direct detection methods are expensive and risk the mobilization of DNAPL, making indirect detection with geophysical methods an attractive alternative.

The objective of this research is to characterize subsurface DNAPL movement with ground penetrating radar (GPR) and inverse multiphase flow simulations. This objective is addressed in four related investigations (Chapters 2, 3, 4 and 5). GPR data provide qualitative information on the subsurface movement of DNAPL at a field site where DNAPL is intentionally injected (Sander and others, 1992; Sander, 1994; Brewster and others, 1995; and Greenhouse and others, 1993). Sneddon and others (2002) present a procedure for interpreting DNAPL saturations from this injection with time and space. The accuracy of the mixing model used in that procedure is examined and an improvement using DNAPL saturations is provided (Chapter 2). The accuracy of the interpreted DNAPL saturations and initial conceptual model of permeability zones provided by Sneddon and others (2002) is examined using fit statistics and residual saturation distributions from inverse multiphase flow simulations. Alternate conceptual models of the permeability zones and different capillary pressure-saturation relationships improve the calibration, but saturation residual bias persists in a channel zone. This remaining bias is attributed to the one-dimensional GPR interpretation, where

multidimensional influences are not considered (Chapter 3). A laboratory-scale sand tank is developed and DNAPL is intentionally injected and monitored with GPR. Given the known geometry, multidimensional influences in the resulting GPR data and GPR modeling results are identified and provide a better understanding of interpreting DNAPL saturations from GPR data (Chapter 4). Inverse multiphase flow simulations of the laboratory scale DNAPL injection indicate the value, along with the limitations, of interpreting DNAPL volumes from GPR data. These simulations demonstrate how analysis of the biased residuals improves the conceptual model of geologic influences on DNAPL flow (Chapter 5).

Information resulting from this research is applicable to future field investigations and remediation of DNAPL source zones. The location and subsurface movement of DNAPLs can be characterized using GPR and inverse multiphase flow simulations, within the limits of the procedure. Understanding the strengths and limitations of this procedure will allow future investigations to proceed more efficiently and be more cost effective (Chapter 6).

1.2 Chapters as Publications

Chapters 2 through 5 of this thesis will be submitted as separate stand-alone publications with the same titles. Chapter 2 will be submitted to the *Journal of Applied Geophysics*. Chapter 3 was originally submitted to *Water Resources Research* before the research relating to Chapters 2, 4, and 5 was completed. The submitted article was declined for publication with the encouragement for re-submittal upon revisions to clarify the research approach and the addition of more information on the cause of biased residuals in the inverted multiphase flow simulations. Chapter 3 was improved by addressing the reviewers' comments and a laboratory-scale DNAPL injection provided additional insight that could address the strengths and limitations of the research

procedure. Chapter 3 in its present form will be re-submitted to *Water Resources Research*. Chapter 4 is currently in review for publication as a USGS Open File Report and should be available soon. Chapter 5 will be submitted to the *Journal of Contaminant Hydrology*. The final version of the submitted article may include a brief summary of the information provided in Chapter 4, which is not included in the present version of Chapter 5 to reduce repetition.

Chapter 2

ACCURACY OF THE ITERATIVE USE OF THE BRUGGEMAN-HANAI-SEN MIXING MODEL TO DETERMINE THE PROPORTIONS OF A MIXTURE OF AIR, WATER AND SAND

2.1 Abstract

For accuracy, an iterative Bruggeman-Hanai-Sen (BHS) mixing model with an air/water/sand system must consider which two-material end member (air/sand or water/sand) to use as the matrix. For a given porosity, a new weighted BHS model provides the best match to measured data. Two BHS curves, one with air/sand as the matrix and one with water/sand as the matrix, are weighted based on the water saturation.

2.2 Introduction

In many environmental applications, indirect testing of the subsurface with geophysical instruments is preferred over direct sampling in order to decrease the disturbance of existing subsurface conditions. Indirect testing is particularly useful for analyzing the conditions of unconsolidated material surrounded by multiple fluids, where any direct measurements could redistribute those fluids. Specific examples include the determination of water and air saturations with depth in agricultural settings, and the determination of non-aqueous phase liquid (NAPL), water, and/or air saturations in areas of suspected contamination. In the latter case, the vertical and horizontal extent of the NAPL spread is important for designing remediation.

Ground penetrating radar (GPR) is one geophysical method that can detect varying saturations of multiple fluids in the subsurface indirectly. GPR modeling programs have been developed to analyze the geophysical properties of materials with depth in the subsurface (Powers and Olhoeft, 1995; Olhoeft, 1998). In this paper, only the geophysical property of dielectric permittivity (defined below) is discussed in detail. The GPR model simulates the reflected radar wave that results from specified subsurface conditions, thereby defining the location of materials with different bulk permittivity values. Mixing models are needed to determine the proportions of the combined materials (i.e, mixtures of air, water and sand) that would produce the associated bulk permittivities.

A variety of mixing models exist, such as empirically based formulas (Topp and others, 1980) and simple volumetric averaging methods (Sihvola, 1999). The Bruggeman-Hanai-Sen (BHS) mixing model (Bruggeman, 1935; Hanai, 1968; Sen and others, 1981) was selected for this research because of its successful application in previous research to two-material systems (Kutrubes, 1986; Olhoeft, 1987). The BHS model is unique because it uses a spherical shape factor to represent a porous medium. Sen and others (1981) developed the final BHS mixing model based on models developed by Bruggeman (1935) and Hanai (1968) and tested the model by measuring the permittivity of fused glass beads of various sizes with different pore fluids, representing "rocks" of variable porosity. The pore fluids (i.e., water, methanol and air) were used one at a time and not in combination, so the resulting system consisted of only two materials. The original purpose of the BHS mixing model was to determine the porosity of a rock sample from the measured bulk permittivity, based on known permittivity values for the fluid and the solid.

Three-material systems with clay, sand and organic liquids have been evaluated by Canan (1999). In this case, the BHS mixing model was not adequate due to clay/organic chemical interactions. In addition, the corrections for air gaps created by incomplete saturation of a two-material system lead to the creation of a complex three-material

formula by Huang and Shen (1983) which was also used by Kutrubes (1986). The objective of the research presented here is to avoid the use of more complex formulas and iteratively use the original two-material BHS model to include a third, non-reactive material. Sneddon and others (2002) iteratively applied the BHS model to determine perchloroethylene (PCE) saturations from a GPR survey of an intentional spill in a water-saturated sand aquifer. However, the interpreted PCE saturations were not independently verified. The research presented here evaluates the accuracy of using the BHS mixing model for a three-material system of air, water, and sand by comparing model results with measured values.

2.3 Background

In general, the permittivity of a material is an indication of its insulating capacity. When a material is placed between two charged metal plates, the ability of that material to store the electrical charge is defined as the material's dielectric permittivity. When a charge is applied to two parallel plates, the resulting device is a capacitor. The resulting capacitance, or the ability to store a charge, for a parallel-plate capacitor is defined by:

$$C = \varepsilon \frac{A}{d} \tag{2.1}$$

where: C = capacitance, ε = material permittivity, A = area, and d = distance between the plates. The material permittivity is often given as a relative permittivity, compared to the permittivity of free space ($\varepsilon = K\varepsilon_0$), where K = relative dielectric permittivity and ε_0 = the permittivity of free space. The relative dielectric permittivity is often referred to as the dielectric constant and the permittivity of air is generally assumed to be the same as that of free space. The dielectric constant value can vary with temperature and frequency, so

the use of the term relative dielectric permittivity is preferable, where the terms “relative” and “dielectric” are often implicit. In addition, energy losses in the electric field of a capacitor due to electrical conductivity may occur at lower frequencies and are accounted for in the imaginary component of the dielectric permittivity. The combined real and imaginary components of permittivity are referred to as the complex dielectric permittivity. The term “complex” is often omitted but implied. The complex dielectric permittivity of a material or a mixture of materials can be calculated directly with Equation 2.1 and measurements of capacitance from a parallel-plate capacitor. The complex relative dielectric permittivity can also be determined using the ratio of the capacitance measured in a fixed-geometry capacitor for the measured material relative to the capacitance measured for air.

Use of a parallel-plate capacitor with a guarded electrode to measure permittivity using ASTM method D150 is quick and easy with a frequency range of approximately 1 Hz to 1 MHz (ASTM, 1998). Laboratory measurements indicate that a mixture of distilled water and dry sand quickly becomes electrically conductive. This results in conductive losses with an associated increase in the imaginary component of the permittivity, as the real and imaginary permittivity components become less than 90 degrees out of phase. To avoid this problem, a resonance method is used to provide measurements at higher frequencies, which are also more typical of a GPR survey (1 MHz to 1 GHz). This procedure uses precision-ground air lines that produce very specific electromagnetic transmission properties. These air lines are essentially a coaxial cable with air as the initial insulator. Using a computer controlled network analyzer, the changes produced by filling the air lines with another material can be related to the complex relative dielectric permittivity of the new material (along with other electromagnetic properties). Accuracy of the relative dielectric permittivity measurements using the air-line system is confirmed by wiring the air line to form two electrodes to measure the capacitance created by the intervening material. With the end connectors attached to reduce stray capacitance, the relative dielectric permittivity of the

intervening material is measured as the ratio of the capacitance in the 10-cm air line filled with a material and the capacitance created using air alone. The resulting values are well within the error associated with interpreting the values from the resonance method of the air-line system, as discussed in the next section.

The analysis in this paper focuses specifically on an air/water/sand system. However, the procedures and theory presented here are applicable to any sand and multiple fluid system. An air/water/sand system is evaluated due to the non-hazardous nature of the materials and the ease of packing an air line with dry sand and subsequently adding water. Addition of an organic liquid to an air line packed with water-saturated sand would be ideal for the study of various NAPLs. However, the non-wetting nature of most NAPLs to a water-saturated sand system requires the design of an air line system to allow for NAPL injection. Development of such an apparatus is ongoing.

2.4 Detailed Measurement Procedure

The equipment used to measure the relative dielectric permittivity of air/water/sand mixtures consists of a Hewlett-Packard network analyzer attached to a precision ground 10-cm General Radio air line (GR-900, Figure 2.1) using semi-rigid coaxial cables. An HP Basic code controls operation of the system. The software controls electronic measurement and calculation of electrical responses used to calculate permittivity values. The measurement procedure includes an initial detailed calibration (once the machine is warmed up) using known shorts and loads on the cables with and without the air line. A measurement is made using air, which is assigned a relative dielectric permittivity of 1.0 for reference to all other measurements. Teflon end plugs at each end of the air line allow retention of the material to be measured (Figures 2.1c and 2.1d). These plugs are included in the calibration measurement. Details on the theory, procedure, and use of the

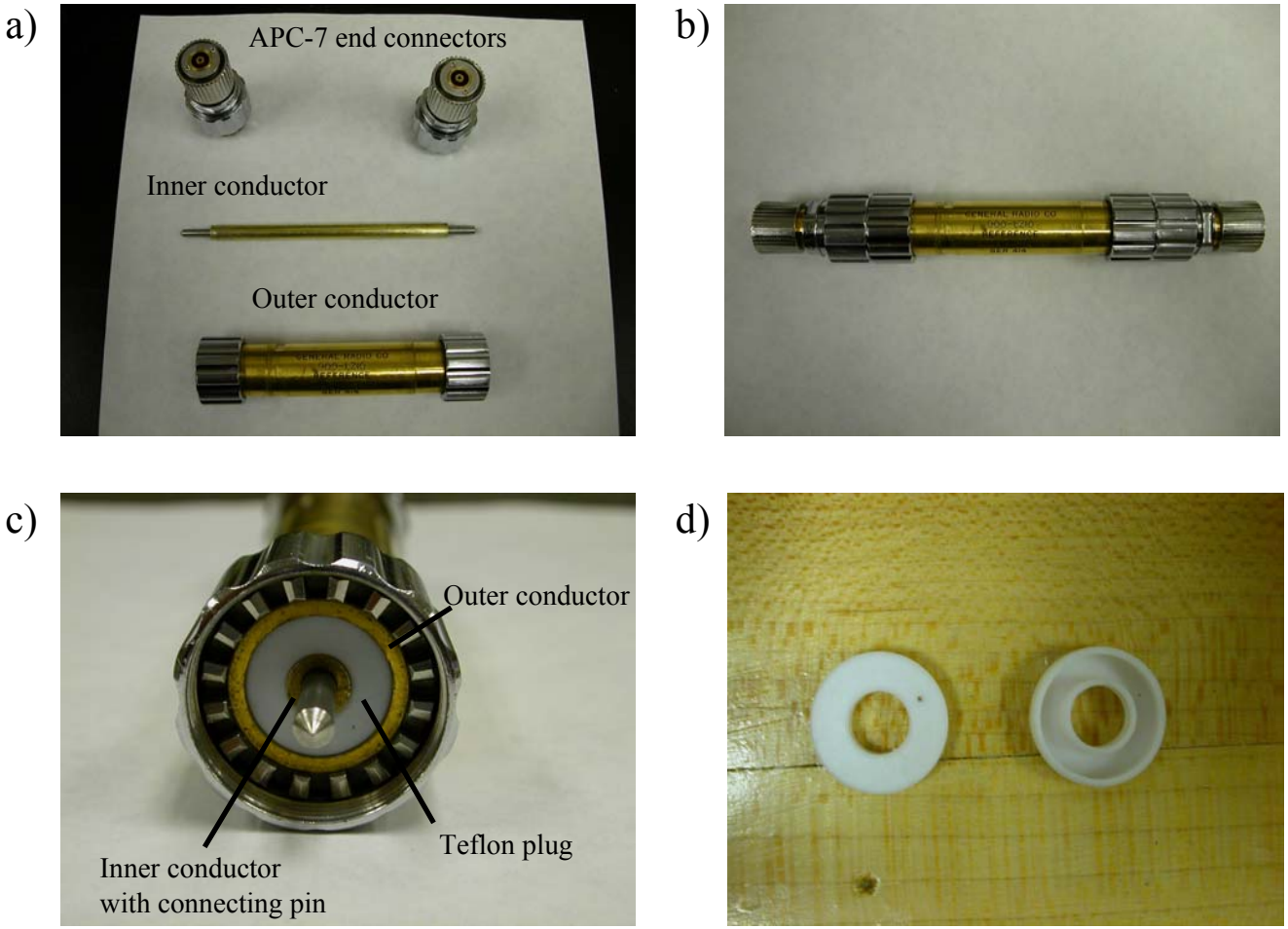

Figure 2.1: 10-cm air line: a) pieces of air-line system; b) assembled air line; c) end of air line with Teflon plug inserted; and d) Teflon plugs.

air line system along with a discussion of measurement errors are discussed in Kutrubes (1986).

Air lines are available in a variety of lengths. A 10-cm length provides for a reasonable range of frequencies and ease of water saturation, while reducing the influence of the Teflon plugs on the permittivity measurements. As discussed in Kutrubes (1986), a shorter air line allows for measurement of permittivity at higher frequencies. Longer air lines limit the frequency range because the sample resonates when the frequency of the transmitted waves approach the natural frequency of the medium. For example, an empty 10-cm airline first resonates at 750 MHz, while dry quartz sand with a permittivity of 2.66 first resonates at approximately 460 MHz. For 70% water-saturated sand with a permittivity near 14, the sample first resonates at a frequency near 200 MHz. A shorter air line first resonates at a higher frequency for the same material and uniform saturation is attained more easily, but the Teflon plugs have a greater influence on the permittivity measurements, resulting in increased error.

The airline itself has a 0.4042-cm wide gap between the solid center cylinder (0.6204-cm outer diameter) which is surrounded by a hollow metal tube with a 1.4288-cm inner diameter (Figure 2.1). The addition of materials in the gap between the cylinder and the tube creates new electromagnetic properties that are detected by the network analyzer. Dry sand is easily poured into the gap and contained using the Teflon end plugs (Figure 2.1). These end plugs are as small as possible, but their presence creates some error. The relative permittivity of Teflon is generally close to 2.1 (von Hippel, 1954), so the error is minimal for materials with a relative permittivity similar to Teflon, but increases for higher permittivity materials.

When #45 Ottawa silica sand from U. S. Silica Company is introduced into the air-line gap, the porosity is determined from the mass of the added sand, the specific gravity of the sand (in this case 2.65 g/cm^3), and the volume of the gap (minus the Teflon caps). A small syringe introduces water through the Teflon plugs to increase saturation in approximately 5% increments and the relative dielectric permittivity for each water

addition is measured. Exact water saturation is calculated by the increase in mass after each addition. Water is a wetting fluid on dry sand, so injection is not difficult, but homogeneous distribution of the water within the sand could not be guaranteed. Water is injected at both ends of the air line to improve the potential for attaining uniform saturation. Achieving full water saturation is difficult because of entrapped air pockets, so the air line was placed under water with an applied vacuum before the final measurement at a saturation of 97.26%. Measured complex relative dielectric permittivity, as a function of frequency, for dry sand and 70% water-saturated sand are shown in Figure 2.2. Permittivity is reported as the stable value occurring at higher frequencies. Measured complex relative dielectric permittivity for #45 Ottawa sand, with a 37.8% porosity, is shown with error bars at various saturations in Figure 2.3.

The permittivity error bars ("y" axis) in Figure 2.3 represent the instrument error in measuring the relative dielectric permittivity. As illustrated in Figure 2.2, the relative dielectric permittivity stabilizes at higher frequencies, but slight variations are interpreted as error in the instrumentation and not a change in permittivity with frequency. The permittivity error bars in Figure 2.3 are based on the total variation of permittivity above 20 MHz. The permittivity value is the most reasonable value based on the plateau of the permittivity versus frequency relationship. Error in the permittivity associated with the Teflon plugs is assumed to be accounted for by this instrumentation error. The maximum frequency for measurement is the resonant frequency of the sample in a 10-cm airline. The minimum measurement frequency (20 MHz) is selected to be above the frequency where background noise is observed and above the frequency where a shift in phase (increase in imaginary component of permittivity) occurs due to the electrically conductive nature of the samples with higher water saturation. This phase shift results in the increasing complex permittivity values below 20 MHz seen for the 70% water-saturated shown in Figure 2.2. Permittivity values below 0.5 MHz are below the measurable range of the air line instrumentation. However, permittivity values at these

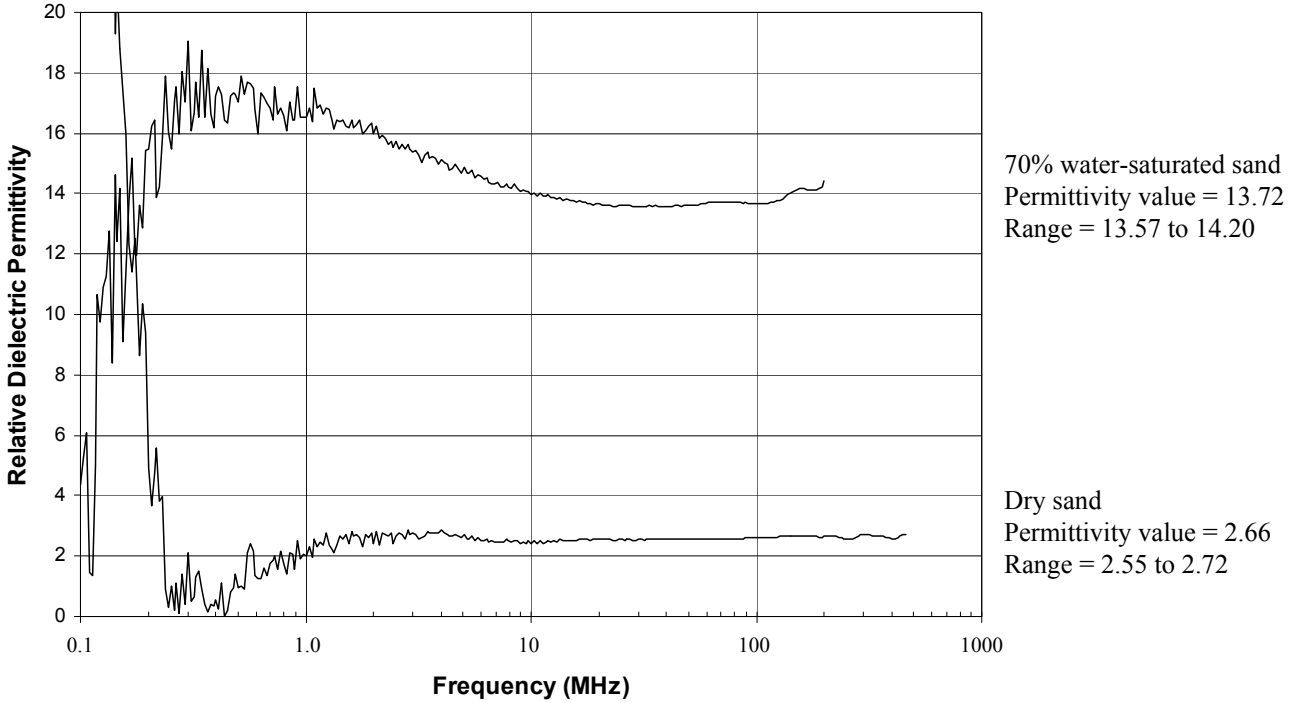

Figure 2.2: Relative dielectric permittivity data for dry sand and 70% water-saturated sand.

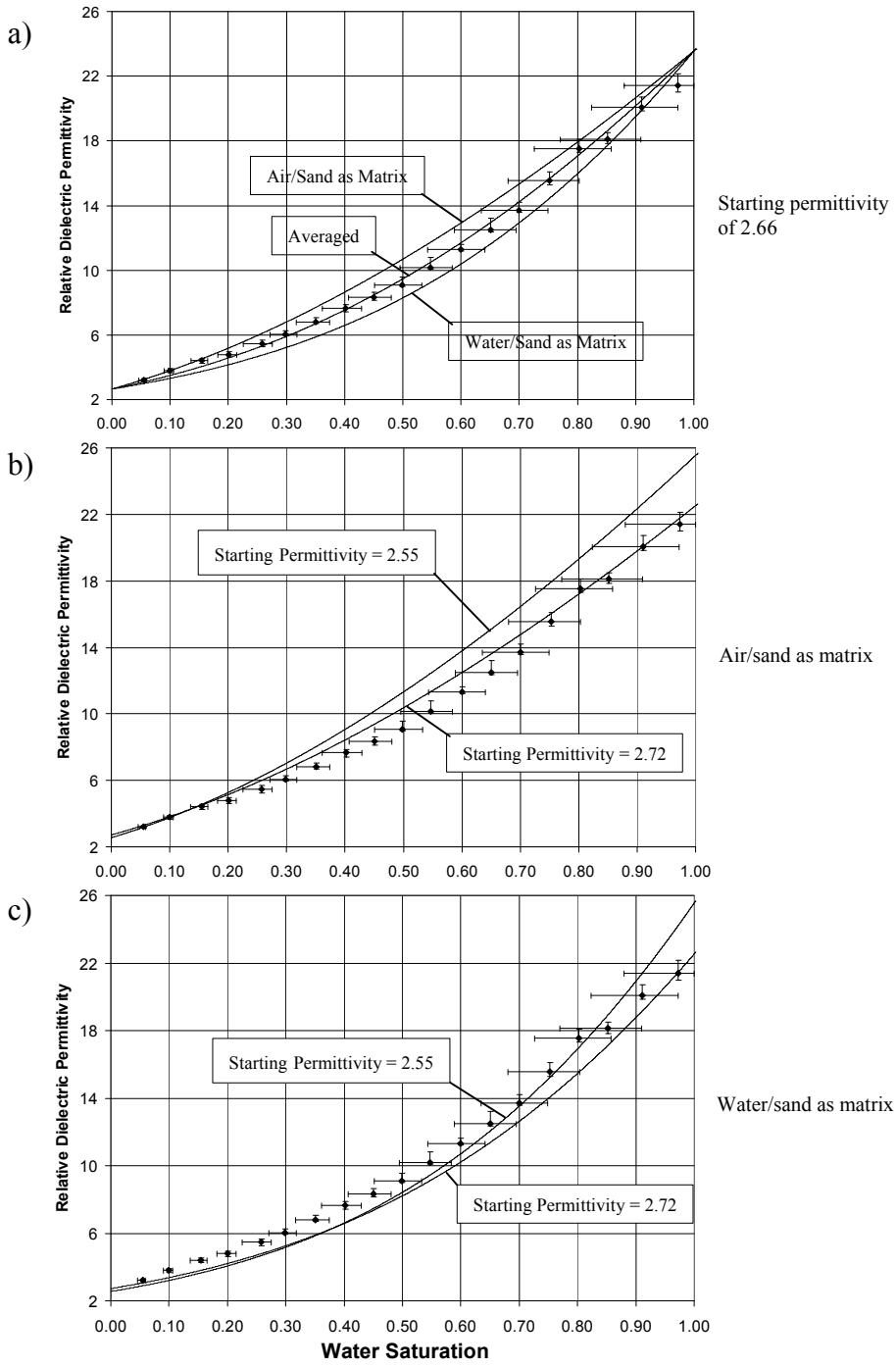

Figure 2.3: Diagrams of various BHS curves and measured data for a porosity of 37.8%: a) air/sand as the matrix, water/sand as the matrix, and their average, with a single starting permittivity for the BHS curve; b) air/sand as the matrix with two representative starting permittivities for the BHS curve; and c) water/sand as the matrix with two representative starting permittivities for the BHS curve. The air line measured permittivities are the same for all three diagrams.

lower frequencies can be measured using the air lines wired as a capacitor, as discussed above.

The saturation error bars ("x" axis) in Figure 2.3 represent the error in water saturation associated with the Teflon plugs. The volume of the two Teflon plugs was measured using water volume displacement, giving a value of 0.5 cm^3. For the plotted saturation values and a calculated porosity of 37.8%, the measured plug volume of 0.5 cm^3 is subtracted from the volume within the air line. The low saturation value on the saturation error bars is calculated by considering the plug volume to be additional air space. During the attachments of the end connectors on the air lines, the plugs can be pushed in farther than flush with the end of the air line. In this situation, the total volume displaced by the plug is greater than the measured plug volume, which produces a slightly lower porosity and higher water saturation for the actual air/water/sand mixture. A reasonable total volume of 0.9 cm^3 for the end plug with added air space produces the maximum saturation values for the saturation error bars. These possible saturation errors are more significant in absolute value for measurements at larger saturation values (Figure 2.3).

2.5 Data Interpretation

A procedure for analyzing three-material mixtures using relative permittivity values is presented by Sneddon and others (2002). This paper explains the iterative procedure for extending the BHS curve to three materials with a PCE/water/sand system. Although the system discussed in the present paper is air/water/sand, the principles are the same where air is now the non-wetting fluid. Sneddon and others (2002) used interpreted values of relative permittivity to determine the porosity of the mixture and the magnitude of PCE saturation. The actual values of porosity and PCE saturation were not confirmed by independent analysis. Thus, the purpose of the measurement of air/water/sand mixtures

is to confirm that the iterative procedure used with the BHS curve produces accurate results. As shown by Sneddon and others (2002), the iterative use of the BHS curve for a three-material system involves an initial interpretation of porosity based on pure sand and pure water as end members. The same procedure is again followed using water-saturated sand and PCE-saturated sand as end members based on the calculated porosity. Intermediate amounts of PCE saturation fall on the new BHS curve with the water/sand and PCE/sand end members at the given porosity.

For this research, the procedure discussed above is followed for air/water/sand mixture instead of a PCE/water/sand mixture. The accuracy of the procedure is evaluated because the actual air/water/sand proportions are known to be within a defined range (Figure 2.3). The BHS equation is as follows:

$$\theta = \frac{(\varepsilon^*_{matrix} - \varepsilon^*_{comp})(\varepsilon^*_{fluid} / \varepsilon^*_{comp})^C}{(\varepsilon^*_{matrix} - \varepsilon^*_{fluid})} \tag{2.2}$$

where:

θ = fractional porosity

ε^*_{matrix} = complex relative dielectric permittivity of the matrix

ε^*_{fluid} = complex relative dielectric permittivity of the fluid

ε^*_{comp} = complex relative dielectric permittivity of the composite mixture

C = shape factor (1/3 for spherical grains)

The relative dielectric permittivity of quartz sand is 4.5 at a frequency of 1 MHz (Olhoeft, 1981) and is generally assumed to be temperature and frequency independent. The relative dielectric permittivity of water is temperature and frequency dependent, but a value of 80 was used based on laboratory temperatures of 20-22 degrees Celsius and measurement frequencies of 1 MHz to 1 GHz. A value of 80 for distilled water in

laboratory conditions was confirmed at 1 MHz in a liquid parallel-plate capacitor with guard rings using ASTM method D150 (ASTM, 1998). Permittivity values decrease dramatically for water at frequencies greater than 10-20 GHz. A detailed formula for the variations of the relative dielectric permittivity of water with temperature and frequency can be found in Hasted (1973). A value of 1.0 is used for the dielectric permittivity of air.

For the initial measurement of the dry sand, the relative dielectric permittivity was 2.66 with a range of values from 2.55 to 2.72 based on variation of the curve plateau shown in Figure 2.2. Using the BHS model with sand as the matrix and air as the fluid, the calculated porosity was 37.94%. For the range of permittivity values the porosity value was 40.78% to 36.43%, respectively. The measured porosity of the dry sand, based on the volume of the gap in the air line minus 0.5 cm^3 for the Teflon plugs, yields a value of 37.8%. For a porosity of 37.8%, the air/sand end member of the iterative BHS curve is 2.66 and the water/sand end member is 23.56, which is determined using the calculated porosity and a BHS curve with sand as the matrix and water as the fluid. However, for the iterative BHS curve it is not clear which end member to use as the matrix, air/sand or water/sand. In Figure 2.3a, BHS curves are shown with air/sand as the matrix and with water/sand as the matrix. The average of the two curves is also shown. The BHS curves for the range of initial air/sand permittivity values with air/sand as the matrix is presented in Figure 2.3b and with water/sand as the matrix in Figure 2.3c.

The measured data indicate the use of air/sand as the matrix at low water saturations (0 to 15% water saturation), and the use of the water/sand as the matrix at high water saturations (85 to 100% water saturation) for the best fit, although the error at high saturation makes this latter determination less clear. For intermediate saturations, the use of a BHS curve based on the average of the air/sand matrix and the water/sand matrix curves provides the best fit. These data suggest that for three-material systems, alternate BHS curves should be used based on the degree of saturation. This variation consists of using the dominant fluid/sand end member as the "matrix" and the less dominant fluid/sand end member as the "fluid," to represent the pore space. This "dominance" is

determined by which fluid (air versus water) is found in greater amounts. At low water saturations, the air/sand system is the most dominant material and is treated as the matrix, while the water/sand permittivity represents the pore space. At high water saturations, the water/sand system is the most dominant material, thus representing the matrix, while the air/sand permittivity represents the pore space. A gradual transition from one curve to the other is most appropriate, so the following formula for calculating saturation is proposed:

$$S = (1 - S)(S_{A/S}) + (S)(S_{W/S}) \tag{2.3}$$

where: S = water saturation, $S_{A/S}$ = water saturation determined from the BHS curve with air/sand as the matrix, and $S_{W/S}$ = water saturation determined from the BHS curve with water/sand as the matrix. Equation 2.3 can be rearranged to directly determine the water saturation as follows:

$$S = \frac{S_{A/S}}{1 + S_{A/S} - S_{W/S}} \tag{2.4}$$

The resulting "weighted" BHS curve is shown in Figure 2.4 with the measured data.

In summary, the determination of water saturation within a porous medium using geophysical data would proceed using the following steps: 1) permittivity of all of the mixture materials (in this case air, water and sand) needs to be known (measured or established values); 2) permittivity of the mixture needs to be measured directly or determined using geophysics; 3) porosity of the porous medium needs to be measured or calculated using the permittivity values from 1 and 2 above and Equation 2.2; 4) permittivity values for the air/sand and water/sand end members are calculated using the porosity value and permittivity values of the individual materials in Equation 2.2; 5) measured permittivity of the composite mixture and permittivity values of the air/sand

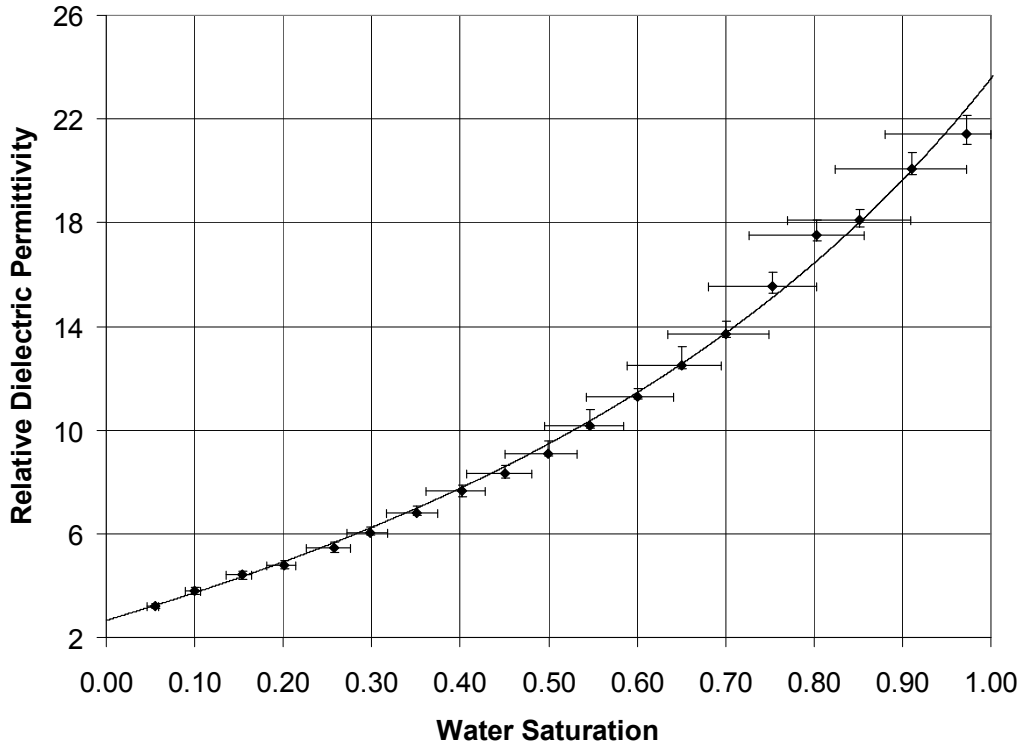

Figure 2.4: Weighted BHS curve using Equation 2.4 and measured permittivities for a porosity of 37.8%.

and the water/sand end members are used two times in Equation 2.2 to calculate water saturations, the first time with the air/sand end member as the matrix and the second time with the water/sand end member as the matrix, where the porosity in Equation 2.2 now represents the water saturation with the respective end members [$S_{A/S}$ and $S_{W/S,}$ respectively]; and 6) water saturation [S] is determined using the calculated $S_{A/S}$ and $S_{W/S}$ in Equation 2.4.

2.6 Conclusions

This research demonstrates that the Bruggeman-Henai-Sen mixing model can be applied successfully to a three-material system with air, water and sand. For accuracy, an iterative BHS model with an air/water/sand system must consider which two-material end member (air/sand or water/sand) to use as the matrix. For a given porosity, a new weighted BHS model provides the best match to measured data. Two BHS curves, one with air/sand as the matrix and one with water/sand as the matrix, are weighted based on the water saturation.

2.7 Future Research

A measurement of permittivity using ground penetrating radar typically represents an average permittivity for a series of geologic layers. As shown by Johnson and Poeter (2003), the determination of the permittivity of individual layers using GPR is non-unique, so an average permittivity over a specified thickness is used to determine dense non-aqueous phase liquid (DNAPL) saturations. In this case, the need for using slightly different BHS curves with different mixture saturations is not as clear because the average saturation represents a series of layers that may have substantially different

saturations. Even within one geologic layer, DNAPL saturation is likely to gradually increase with depth due to gravity-capillary equilibrium conditions. Future research will be necessary to determine if the procedure outlined in this paper is applicable to measurements representing three-component mixtures in a bulk unit with varying saturations. This future research will involve the direct measurement of three-material systems with NAPL/water/sand mixtures, including the development of a measurement apparatus to allow for the injection of NAPLs into a water-saturated sand system.

2.8 References

ASTM, 1998, Standard test methods for AC loss characteristics and permittivity (dielectric constant) of solid electrical insulation, 19 p.

Bruggeman, D. A. G., 1935, Berechnung verschiedener physikalischer konstanten von hetarogenen substanzen: *Ann. Phys. Lpz.*, **24**, p. 636-679.

Canan, Birsen, 1999, Dielectric properties of mixtures of clay-water-organic compounds, M.Sc. Thesis, Dept. of Geophysics, Colorado School of Mines, Golden, 332 p.

Hanai, T., 1968, Electrical properties of emulsions, *in* Sherman, P., Ed., Emulsion science: Academic Press.

Hasted, J. B., 1973, *Aqueous dielectric,* London, Chapman & Hall, 302 p.

Huang, F. S. C., and Shen, L. C., 1983, Analysis of error due to presence of gaps in the measurement of rock samples in a coaxial line, *Geophysics*, **48**, pp. 206-212.

Johnson, R. H., and Poeter, E. P., 2003, Interpreting DNAPL saturations in a laboratory-scale injection with GPR data and direct core measurements, U. S. Geological Survey Open File Report, in review.

Kutrubes, D. L., 1986, Dielectric permittivity measurements of soils saturated with hazardous fluids: M.Sc. Thesis, Dept. of Geophysics, Colorado School of Mines, Golden, 300 p.

Olhoeft, G.R., 1981, Electrical properties of rocks, *in* Physical Properties of Rocks and Minerals, in Touloukian, Y. S., Judd, W. R., and Roy, R. F., eds.: New York, McGraw-Hill, pp. 257-330.

Olhoeft, G.R., 1987, Electrical properties from 10-3 to 10+9 Hz --physics and chemistry, *in* Physics and Chemistry of Porous Media II, American Institute of Physics Conf. Proc. 154, Ridgefield, CT, 1986, J.R. Banavar, J. Koplik, and K.W. Winkler, eds., NY, AIP, pp. 281-298.

Olhoeft, G. R., 1998, GRORADAR™: Acquisition, processing, modeling, and display of ground penetrating radar data: ver. 4.0, software distributed on CD-ROM at Seventh International Conference on Ground Penetrating Radar, (http://g-p-r.com).

Powers, M. H. and Olhoeft, G. R., 1995, GPRMODV2: one-dimensional full waveform forward modeling of dispersive ground penetrating radar data, version 2.0: U. S. Geological Survey Open File Report 95-58, 41 p. + floppy diskette.

Sihvola, A. H., 1999, Electromagnetic mixing formulas and applications, *IEEE electromagnetic waves series*, **47**, Institution of Electrical Engineers, London.

Sen, P. N., Scala, C., and Cohen, M. H., 1981, A self-similar model for sedimentary rocks with application to the dielectric constant of fused glass beads, *Geophysics*, **46**, pp. 781-795.

Sneddon, K. W., Powers, M. H., Johnson, R. H., and Poeter, E. P., 2002, Modeling GPR data to interpret porosity and DNAPL saturations for calibration of a 3-D multiphase flow simulation, U. S. Geological Survey Open File Report 02-451, 29 p.

Topp, G. C., Davis, J. L., and Annan, A. P., 1980, Electromagnetic determination of soil water content: Measurements in coaxial transmission lines: *Water Resources Research*, **16**, pp. 574-582.

von Hippel, A. R., 1954, *Dielectric materials and applications,* NY, Wiley and Sons, Inc. 438 p.

Chapter 3

INVERSE MULITPHASE FLOW SIMULATION TO EVALUATE CONCEPTUAL MODELS, ESTIMATE INTRINSIC PERMEABILITIES AND IDENTIFY BIAS IN FIELD DATA, FOR A FIELD-SCALE DNAPL INJECTION IN BORDEN SAND GIVEN TIME-LAPSE GPR DATA

3.1 Abstract

Perchloroethylene (PCE) saturations determined from GPR surveys are used as observations for inversion of multiphase flow simulations of a PCE injection experiment, allowing for the estimation of optimal intrinsic permeability values. Synthetic simulations reveal that saturation data alone are sufficient to estimate optimal intrinsic permeability values, but the character and magnitude of error in the saturation data are critical to accurate estimation. The resulting fit statistics and analysis of residuals (observed minus simulated PCE saturations) are used to improve the conceptual models of permeability zones and capillary pressure-saturation relationships. Remaining bias in the residuals is attributed to the violation of assumptions (lack of flat, infinite, horizontal layers) in the one-dimensional GPR interpretation due to multidimensional influences. However, this bias does not affect the calculation of the optimal permeability values. The effort to improve model fit and reduce residual bias decreases simulation error even for an inversion based on biased observations. This effort is thus warranted and provides information on bias in observation data when this bias is otherwise difficult to assess.

3.2 Introduction

According to the National Research Council (1994), the presence of dense non-aqueous phase liquids (DNAPLs) in the subsurface is a pressing problem limiting groundwater cleanup. Once introduced to the subsurface, DNAPLs occupy pore spaces at residual saturations due to capillarity, serve as a long-term source for groundwater contamination due to their low solubility values, and must often be removed or isolated before any permanent groundwater remediation is possible. Successful detection and simulation of the subsurface distribution and movement of DNAPLs is an initial step in evaluating possible removal and/or isolation techniques.

Feasible methods for removing DNAPLs from the subsurface using surfactants, co-solvents, and complexing agents have been demonstrated. For a brief overview of these remedial methods, see McCray and Brusseau (1998). The greatest obstacle to such remedial action is the proper delivery of remediation fluids to the DNAPL source because of the incomplete identification of the distribution of DNAPL and associated properties of the porous media (McCray and Brusseau, 1998). If the distribution of DNAPL and porous media properties are known, they can be incorporated into multiphase flow simulations and used to evaluate alternative remedial schemes. However, it is hazardous and expensive to measure the small-scale variations in parameters controlling DNAPL transport using conventional methods such as direct coring. Remote sensing methods such as ground penetrating radar (GPR) have proven successful in determining DNAPL distributions (Greenhouse and others, 1993; Sander, 1994; Sneddon and others, 2002). Remote sensing of DNAPL distribution reduces the need for expensive and intrusive data collection from monitoring wells and coring, produces spatially continuous data, and provides observations for inverse modeling to estimate parameter values needed for multiphase flow simulations.

3.3 Objective and Approach

The objective of this research is to evaluate the suitability of DNAPL saturations interpreted from GPR data for use as observations to invert multiphase flow simulations. These inversions estimate the intrinsic permeability values that provide the best fit between field observations and simulated values of DNAPL saturation. Inversion not only yields estimates of optimal parameter values, but also provides crucial fit statistics to use in identifying the most appropriate conceptual models (Poeter and Hill, 1997). If optimal parameter values are unreasonable, the fit to field data is poor, the residuals are biased in space and/or time, or are not normally distributed, the conceptual model is adjusted to improve the results (Poeter and Hill, 1996; Poeter and Hill, 1997; Hill, 1998). Practical nonlinear least-squares inverse software such as PEST (Doherty, 1994) and UCODE (Poeter and Hill, 1998) facilitate conceptual model analysis.

First, synthetic test examples, with and without error in the saturation observations demonstrate the potential for using DNAPL saturations to estimate permeability in a multiphase flow simulation. Next, GPR data are used to define an initial conceptual model of a field DNAPL injection and nonlinear regression estimates optimal permeability values. Inversion statistics are used to evaluate the initial model, develop alternative conceptual models, and identify the most representative models. The alternative models consist of different geometries of permeability distributions, different formulations of the capillary pressure-saturation relationship, and alternative weighting schemes. Finally, spatial bias in the best model is evaluated to identify limitations in the GPR interpretation.

Generally, observations used to invert flow models are straightforward, albeit uncertain, measurements. This study is unique in that the observations are themselves determined from fitting a model of dielectric permittivity to a GPR wave and translating the permittivity to DNAPL saturation via another model. The interpretation of the GPR

data by Sneddon and others (2002) provides DNAPL saturations for use as observations to invert the multiphase flow simulations.

3.4 Borden Cell DNAPL Injection Experiment and GPR Survey

In 1991, the University of Waterloo intentionally injected the DNAPL perchloroethylene (PCE), into a completely isolated (laterally, by joint-sealed steel sheet pile walls; vertically by an underlying aquitard), hydrostatic, fully-saturated, 9 by 9 by 3.3 m portion of the sand aquifer at Canadian Forces Base Borden, Ontario, Canada. Although PCE was injected under constant head at a depth of 60 cm in the field, it resulted in a relatively constant rate of 11 liters/hr for a total of 770 liters over 70 hours (Redman, 1992; Greenhouse and others, 1993). The only flow in the system is caused by PCE displacing water to a constant head sump at the top corner of the cell. The Borden aquifer consists of thinly bedded, fine to medium-grained, moderately well to well-sorted beach-foreshore sands (Bolha, 1986). These sands form sedimentary beds that are horizontal, to sub-horizontal, lenticular structures with horizontal correlation lengths for permeability of 2.8 m and vertical correlation lengths of 0.12 m (Sudicky, 1986). Turcke and Kueper (1996) find the upper 1.5-2 meters of sand to be relatively unstructured in a sand pit approximately 550 m southwest of the experimental cell and measured a permeability of $7x10^{-12}$ m^2 in deeper zones with a horizontal correlation length of 4.8 m and a vertical correlation length on the order of 0.2 m.

Ground penetrating radar tracked the injection (Greenhouse and others, 1993; Sander, 1994; Sander and Olhoeft, 1994) and provided data for estimating PCE saturation (Figures 3.1 and 3.2). Eight other geophysical surveys qualitatively confirm the GPR detection of PCE (Brewster and others, 1995; Greenhouse and others, 1993). A pre-injection image of the 500 MHz GPR data (Figure 3.2a) shows limited spatial variation in GPR response produced by slight variations in porosity, because the dielectric

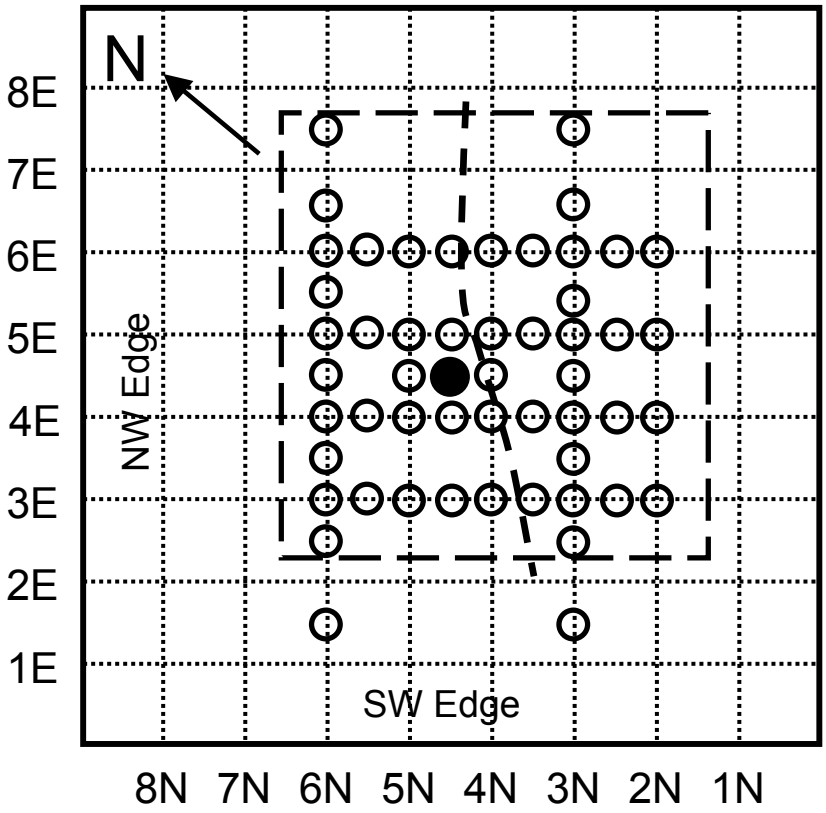

Figure 3.1: Overhead view of Borden injection cell with location of sheet pile walls (solid rectangle), GPR lines (dotted grid lines), 1D GPR interpretations (open circles), injection point (solid circle), flow simulation domain (long-dashed rectangle) and division between units of differing permeability (short-dashed curved line).

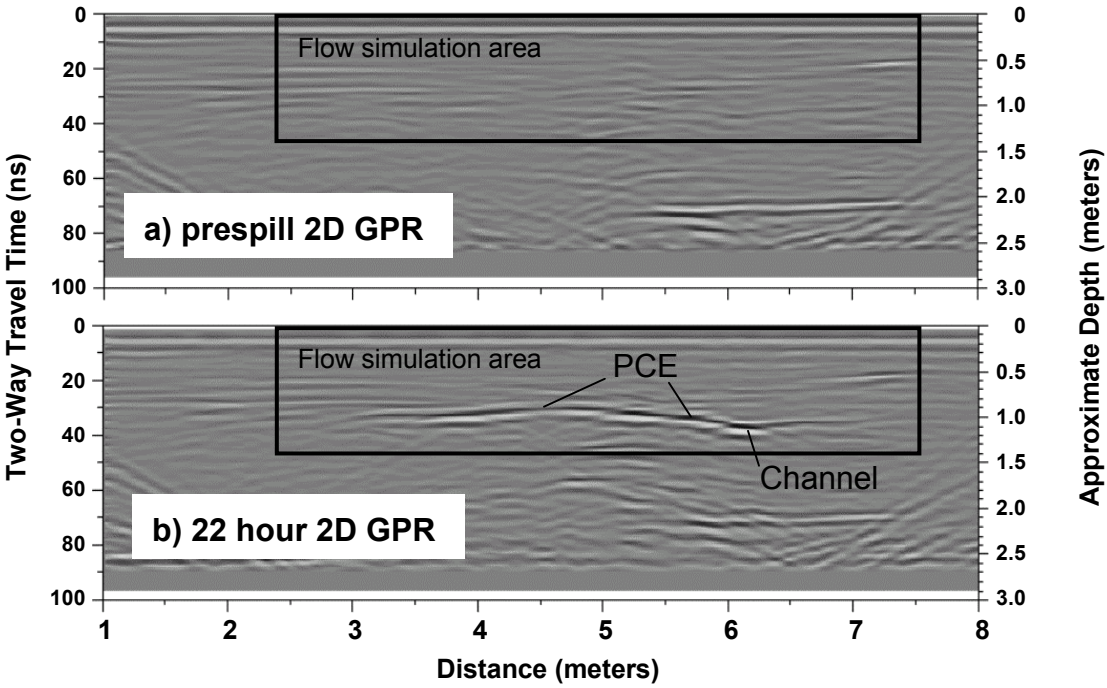

c) prespill 1D interpretation

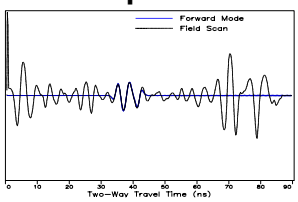

Depth (m)	Permittivity	Porosity	Unit	Relative Permeability
0.97	25.0	0.40	1	High
1.03	20.0	0.33	2	High
1.09	25.0	0.40	3	Low
1.17	20.5	0.33	4	High
	25.0	0.40	5	Low

d) 22 hour 1D interpretation

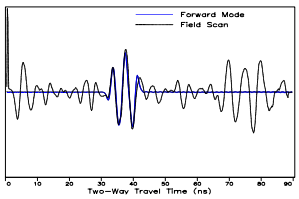

Depth (m)	Permittivity	Saturation	Unit	Relative Permeability
0.92	25.0	0.00	1	High
1.00	13.5	0.35	2	High
1.06	25.0	0.03	3	Low
1.17	10.5	0.36	4	High
	25.0	0.00	5	Low

Figure 3.2: 500 MHz GPR data and interpretations for Borden PCE injection: a) prespill image at line 4N (see Figure 3.1 for line locations); b) 22 hour image at line 4N; c) prespill 1D GPR interpretation of line 4N at 5 m (field scan is dashed and forward model is solid); and d) 22 hour 1D GPR interpretation of line 4N at 5 m (data provided by Sneddon and others, 2002).

permittivity varies with the ratio of sand and water. The diagonal bands at the lower corners of each GPR image are reflections from the steel sheet-pile walls. The PCE pooled at approximately 1 m below the surface and spread laterally (Figure 3.2b) within a coarse to medium-grained sand that overlies finer-grained sand. PCE induced variations in GPR response yield greater contrast of banding in the 2D images as PCE replaces water. Falling head permeability tests (Redman and Kueper, 1992) and visual inspection of cores (Sneddon and others, 2002) confirm a consistent permeability contrast at a depth of approximately 1 m. The PCE flowed along this contact and entered a trough in the contact surface with an axis that approximately parallels the 3N GPR line (Figure 3.1), which is referred to as a channel (Figure 3.2b). Significant PCE flow below the ~1 m contact did not occur until after 22 hours. The geophysical data indicate that the PCE at depths below 1 m pooled in thin (5-30 cm), more or less randomly distributed zones (Greenhouse and others, 1993), indicating layers with lower horizontal correlation lengths for permeability.

Quantitative interpretation of GPR data up to 22 hours defines: 1) the initial conceptual model by providing elevation of the contact between a low permeability zone and an overlying slightly coarser-grained sand, where PCE pools and spreads laterally and 2) PCE saturations as a function of space and time, which serve as observations to invert the multiphase flow simulations. Sneddon and others (2002) describe the interpretation procedures, where one-dimensional (1D) GPR models are calibrated to the field data at the locations shown in Figure 3.1. Calibration of a pre-injection GPR trace establishes varying porosity with depth (Figure 3.2c), which is assumed to reflect changes in permeability. Differences found in the GPR trace from a later time at the same location (Figures 3.2d) are used to calculate the PCE saturation as well as refine the location of permeability zones (Sneddon and others, 2002).

The calibration of the 1D GPR models is non-unique because a simulated match to the data involves several unknown model parameters: a constant gain function that affects the overall reflection amplitudes, the number of layers, the layer permittivities, and the

layer depths. This problem is partially overcome by fixing the constant gain function for all locations in the domain at all times. In addition, the number of layers and their depths are identified by the location of reflections due to the presence of DNAPL and can vary between locations, but remain approximately the same through time. The adjustment of the remaining parameter, the permittivity, creates a unique calibration when the other parameter values are fixed (Figures 3.2c and 3.2d). Due to this non-uniqueness, the porosity and DNAPL saturations interpreted via the calibrated permittivity values may not be exactly correct with depth, but they are constrained enough to produce reasonable and consistent interpretations of DNAPL saturations in time and space within a bulk thickness.

The enhanced bright and dark bands indicating PCE inflow in the 2D GPR image (Figure 3.2b) correspond to a sequence of peaks and troughs in the 1D image (Figure 3.2d). The multiple amplitude increases in the GPR wave were initially interpreted as two, separate zones of increased PCE saturation, but were interpreted as one PCE zone for calibration of the multiphase flow simulations. PCE spreads where a higher permeability zone overlies a lower permeability zone; consequently, the upper zone (less than 1.17 meters in Figure 3.2c and 3.2d and approximately less than 1 meter in Figure 3.2a and 3.2b) is thought to be a higher permeability sand. PCE saturation, estimated from the GPR survey conducted 22 hours after injection began is superposed on a contour map of the depth to the permeability contrast and reveals higher saturation near the source and in the channel feature (Figure 3.3).

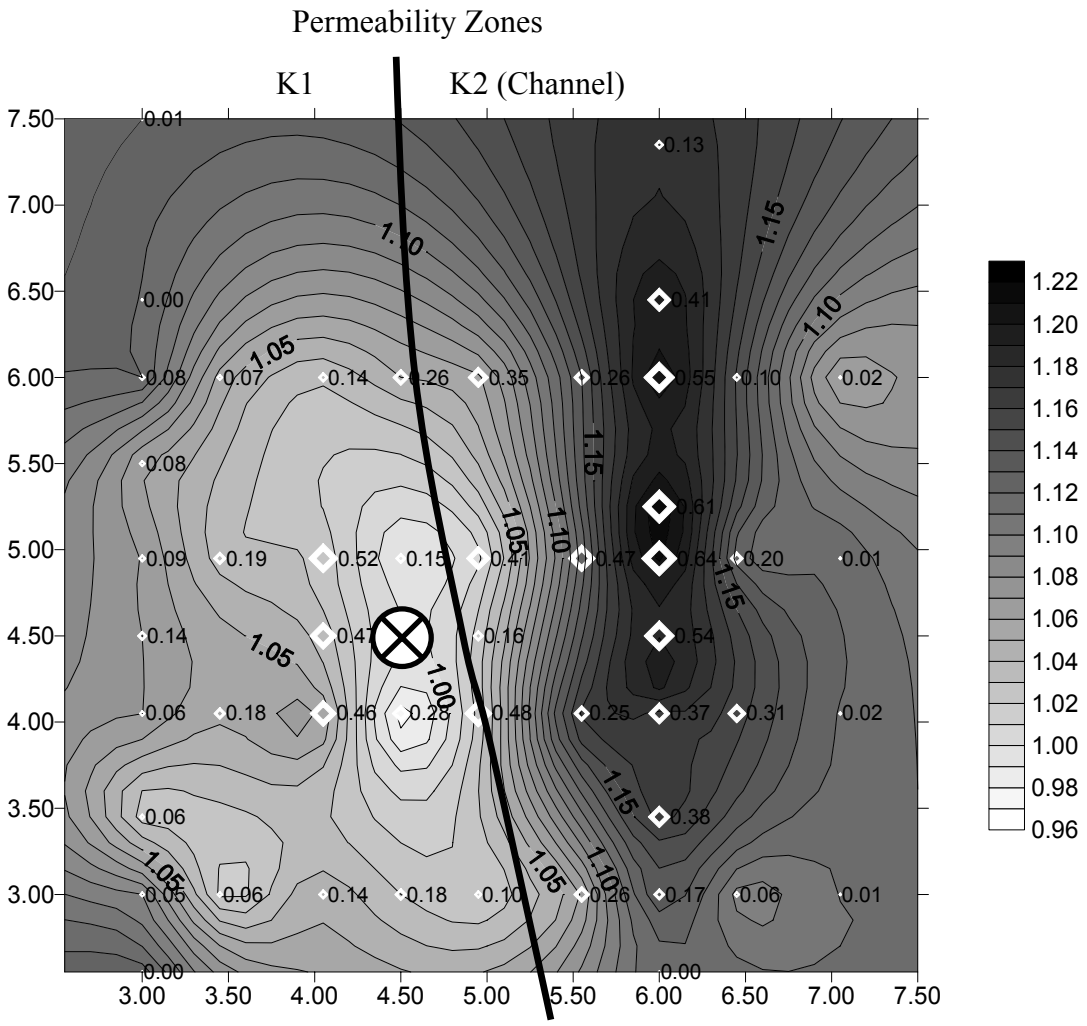

Figure 3.3: Contours of depth to the contact where DNAPL spreads (darker areas are deeper) and diamonds are proportional to DNAPL saturation 22 hours after injection began (data provided by Sneddon and others, 2002).

3.5 Inverse Multiphase Flow Simulations

3.5.1 Multiphase flow simulation

3D2PHASE, a two-phase flow code (Gerhard and others, 1998; Kueper and Frind, 1991a, 1991b), provided by Queen's University, is used for the multiphase flow simulations. Inputs include fluid properties, boundary conditions, and the subsurface geology in terms of the distribution of intrinsic permeability and characteristic curves (porosity cannot be varied spatially in 3D2PHASE). 3D2PHASE calculates fluid pressures and saturations in space and time. For this experiment, the fluid properties, boundary conditions, and characteristic curves are known (Table 3.1), while the subsurface geology is approximated from the GPR data.

To limit computation time, the model encompasses a horizontal domain of 5 by 5 m and a vertical domain of 1.25 m (Figures 3.1 and 3.2), which includes the full extent of PCE migration between 0 and 22 hours. A uniform cell size, 0.15 by 0.15 m in the lateral direction and 0.05 m in the vertical, is used. To represent the sealed sheet pile walls, fine-grained underlying unit, and the unchanging water level at the top of the domain, no-flow conditions are specified at the side, bottom, and top boundaries except for one, top corner cell that is defined as a constant atmospheric pressure to represent water outflow to the sump during PCE injection. A constant PCE flux of 3.06×10^{-6} m^3/s (11 liters/hour) is specified at 60 cm below the ground surface.

3.5.2 Calibration

Calibrating the simulated PCE injection involves: 1) creating a conceptual model of permeability zones and capillary pressure-saturation relationships; 2) simulating the PCE injection, using nonlinear regression to adjust the intrinsic permeability values until the

Table 3.1: Fluid properties, boundary conditions, and characteristic curves from the Borden DNAPL injection experiment for multiphase flow modeling

Property	**Value**	**Source**
density of water	1000 kg/m^3	
density PCE	1625 kg/m^3	
viscosity of water	0.001 Pa-s	
viscosity of PCE (visc)	0.0009 Pa-s	
interfacial tension between water and PCE (inttens)	0.045 N/m	*Kueper and Frind* [1991b]
Brooks-Corey displacement pressure (pd)	0.00558	" "
Brooks-Corey pore size distribution index (lambda)	2.48	" "
residual wetting phase saturation (residsat)	0.078	" "
exponent α	0.65	" "
average porosity (por)	0.37	*Sander* [1994]
van Genuchten α	0.00062	Visual inspection of capillary pressure-saturation curves *Kueper and Frind* [1991b]
van Genuchten n	3.5	" "

simulated PCE saturations best match the saturations determined from the GPR survey; 3) evaluating the estimated parameter values, overall fit, and residual; and 4) iterating the process with a new conceptual model that is modified in a manner intended to reduce both the sum-of-squared-weighted residuals (SOSWR) and the residual bias. The "best" conceptual model has reasonable parameter values, the best-fit, and least-biased residuals as determined by: 1) visual inspection of model results to confirm the parameter values and simulated values are reasonable and to identify temporal and/or spatial bias of residuals; 2) review of measures of model fit including the SOSWR, which should be minimized, standard error (square root of SOSWR divided by degrees of freedom {# observations + # parameters}), correlation coefficient between weighted observed and weighted simulated values (R O/S), and the goodness of fit between the residuals and a normal distribution (RN2); where these latter three items should approach one; and 3) evaluation of graphical displays, including weighted residuals versus weighted simulated values which should form a uniform horizontal band centered about zero, and observed versus simulated values which should fall on a 45^{o} line intersecting the origin.

Residuals provide a guide for trial-and-error definition of permeability zones, while permeability values are estimated by nonlinear regression (only permeability values are optimized in this case because other input parameters have been measured and simulated results are more sensitive to changes in permeability values than any other parameter, Figure 3.4). Use of nonlinear regression to estimate parameter values allows focus on improving the conceptual model (Poeter and Hill, 1997) and provides statistics for model comparison. Hill (1998) outlines methods and guidelines for effective model calibration. UCODE (Poeter and Hill, 1998) performs the inverse modeling, posed as a parameter estimation problem, using nonlinear regression. With respect to the parameter values, UCODE minimizes the SOSWR between observed and simulated saturations using a modified Gauss-Newton method. The algorithm is the same as used in MODFLOWP (Hill, 1992) and MODFLOW2000 (Hill and others, 2000), but UCODE can be applied to

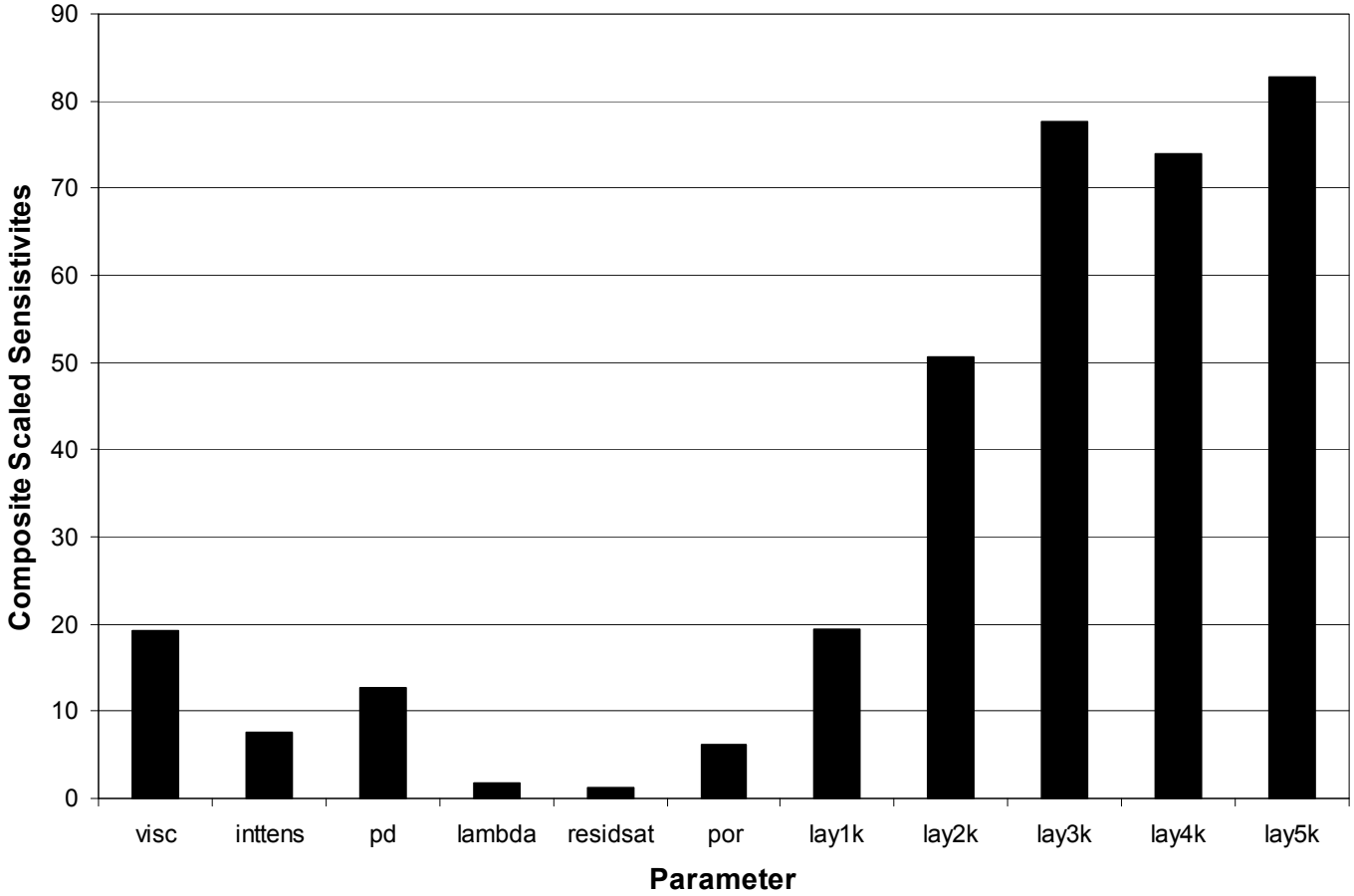

Figure 3.4: Composite scaled sensitivities for parameters used in the 3% error synthetic test case (abbreviations are listed in Tables 3.1 and 3.2).

any model with text based input and output while the others are limited to MODFLOW simulations.

Calibration data consist of PCE saturation values at 5, 14, and 22 hours derived from the GPR interpretation, which are determined by relating permittivity changes to PCE saturations (Sneddon and others, 2002). Generally, the accuracy and precision of the calibration data are known and the focus is on finding the best conceptual model to fit the data by analyzing residual statistics from the regression. For this research, the accuracy and precision of the calibration data are not known. As a result, the residual statistics are used to evaluate the interpretation of the GPR data in addition to evaluating alternative conceptual models.

3.6 Synthetic Test Cases to Evaluate Inversion Potential

Synthetic test cases are used to determine whether use of DNAPL saturation observations alone are sufficient to estimate optimal intrinsic permeability values for a system like the Borden injection experiment. The synthetic system, with the same geometry, source, and parameters as the Borden cell, represents five units as presented in Table 3.2. DNAPL will flow laterally along units where higher permeability overlies lower permeability, in this case units 2 and 4 (Table 3.2). A forward simulation is completed to produce DNAPL saturation values representing values at locations where 1D GPR models are available for the field site, and these are used as observations to optimize permeability values in the synthetic model. The inversion is started with incorrect permeability values to determine if the regression will converge to the true permeability values of the synthetic system that were used to generate the synthetic observations.

Forward simulations indicate little, to no, DNAPL saturation occurs in unit 1 at the locations where GPR data are available. As a result, the permeability value of unit 1 is

Table 3.2: Units and properties of the synthetic test case

Unit	Above Depth (m)	Intrinsic permeability (m^2)
1 (lay1k)	0.92	9×10^{-12}
2 (lay2k)	1.00	9×10^{-12}
3 (lay3k)	1.06	7×10^{-12}
4 (lay4k)	1.17	1×10^{-11}
5 (lay5k)	1.50	1.1×10^{-14}

less sensitive to the observation data. In addition, it is correlated to the other permeability values so units 1 and 2 are assigned the same permeability value. With a conceptual model where the permeability of units 1 and 2 is estimated as one value and the DNAPL saturation data are error free, the inversion of the synthetic case converges to the true permeability values.

Normally distributed error with a mean of zero and a standard deviation of 3% saturation is used to create five distributions of synthetic saturation observations using a random number generator. Resulting negative saturation values are assigned zero-saturation. This creates some bias, but is representative of the GPR data interpretation procedure, because physically impossible negative DNAPL saturations are assigned zero saturation. The fourth observation set is the only set that does not yield optimal permeability values consistent with the true values for both units 2 and 4 (Figure 3.5). The same five sets of error distributions are also simulated with a standard deviation of 5%, and 7% of the saturation values. With a 5% standard deviation, the confidence intervals are larger and again, only the fourth distribution yields optimal values with 95% confidence intervals that do not include the true permeability values. With a 7% standard deviation, two distributions produce reasonable results and three distributions do not produce a convergent regression with reasonable solution parameters, indicating that this is the approximate upper limit of error for which reasonable optimal permeability values can be obtained.

To evaluate the deviation for the fourth observation set, separate inversions are conducted with error in observations removed from each unit. For the standard deviation of 3% and 5%, removal of error from the four points surrounding the injection area in unit 2 produce optimal parameters similar to those from the other distributions. Inspection of the trend of PCE saturation indicates that the addition of error to these four observations created a situation where the PCE saturation decreases between one of the calibration times. Simulations of continuous injection reveal that PCE saturation continually increases everywhere within the flow domain except for a slight, and

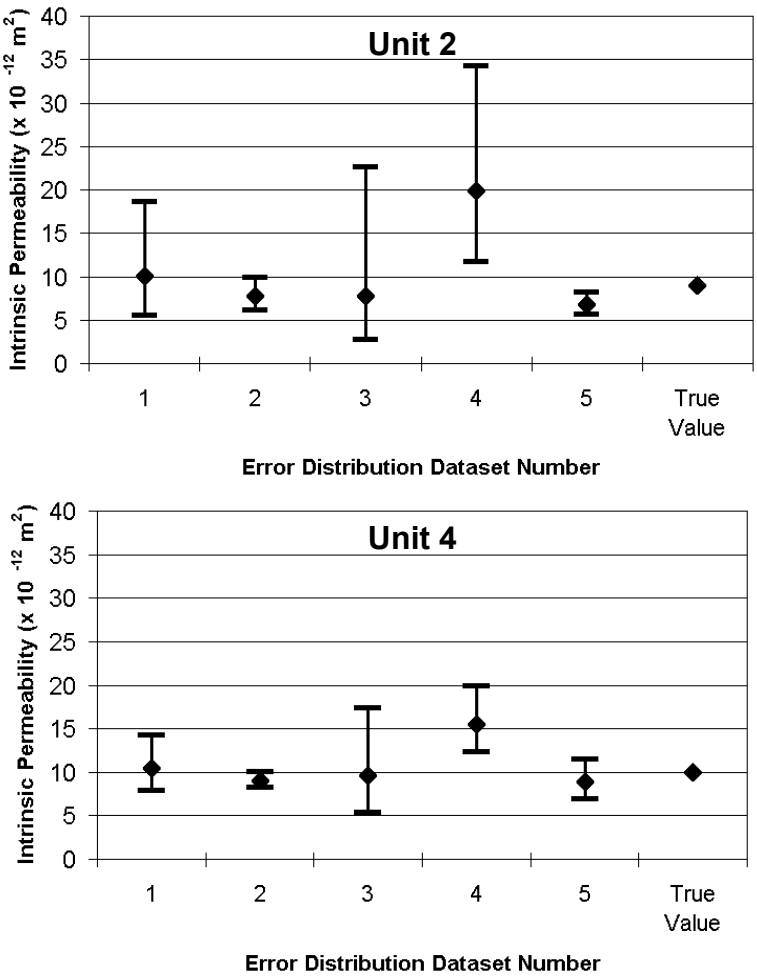

Figure 3.5: Optimal intrinsic permeability values with 95% confidence intervals for synthetic test cases with five different error distributions.

temporary, decrease when the PCE breaks through an underlying lower permeability layer. The synthetic GPR data are available at only a few time intervals and are not located under the injection zone where PCE breaks through the underlying low permeability layer; consequently, synthetic PCE saturation observations should never decrease with time. The fourth observation set presents a scenario where the DNAPL saturation decreases with time in unit 2 (a physical impossibility at this location and time), which yields inaccurate estimates of permeability. This saturation reversal does not occur in any of the other observation sets

The synthetic test cases illustrate that DNAPL saturations alone are sufficient to estimate permeability values for this situation of known flux and boundary conditions, given that the magnitude of observation error is small relative to the observed saturations and the errors do not reverse temporal trends in the observations. For the DNAPL saturations derived from GPR interpretations of the Borden DNAPL injection, the magnitude of the error is difficult to quantify (Sneddon and others, 2002). In addition, the 1D GPR interpretations produce some significant decreases in PCE saturation over time at several locations near the injection zone.

3.7 Inversion to Evaluate Conceptual Models of Borden DNAPL Injection

3.7.1 Initial conceptual model

Although the GPR interpretation from Sneddon and others (2002) represents DNAPL in two units, the initial conceptual model considers these two units as one bulk DNAPL zone. Given the non-uniqueness of DNAPL saturation with depth in the GPR interpretation, this approach is taken because inverse multiphase flow simulations with two units produced similar results to simulations with one unit.

The initial conceptual model represents a higher permeability sand unit overlying a low permeability unit of variable depth, including a ridge below the source. The higher permeability sand unit is split into two zones (Figure 3.1) following the ridge (Figure 3.3) to allow for the possibility of a different permeability within the channel zone. The capillary pressure-saturation curve is represented by the Brooks-Corey formulation (Brooks and Corey, 1966) and the simulation is optimized using observations of GPR-estimated PCE saturation. The topography of the contact creates a hydraulic divide in the simulated PCE flow, yielding simulated saturations inconsistent with saturations determined from the GPR data. The overall fit of the "initial" simulation can be measured by the residual analysis presented in Figure 3.6 and global fit parameters presented in Figure 3.7. In an effort to develop a conceptual model that would produce saturations consistent with field observations and eliminate residual bias, alternative conceptual models are considered.

3.7.2 Alternate conceptual models

The alternative models illustrate the process of conceptual model evolution, proceeding towards better statistical fits and less biased residuals (Figures 3.6 and 3.7). A lower sum-of-squared weighted residuals (SOSWR, note division by 1000) and a standard error that is close to one indicate improvement in the statistical fit. A slope and intercept of the weighted residuals versus weighted simulated values that approaches zero and graphs that take on the visual appearance of an even band of residuals distributed about zero at all levels of saturation indicate an improvement in the bias of the residuals.

The inconsistency between the simulated hydraulic divide and the lack of a divide in the field observations, coupled with the possibility that the permeability contact depth is underestimated near the source (as described in the next section), lead to the second conceptual model (flat model). This conceptual model decreases the elevation of the

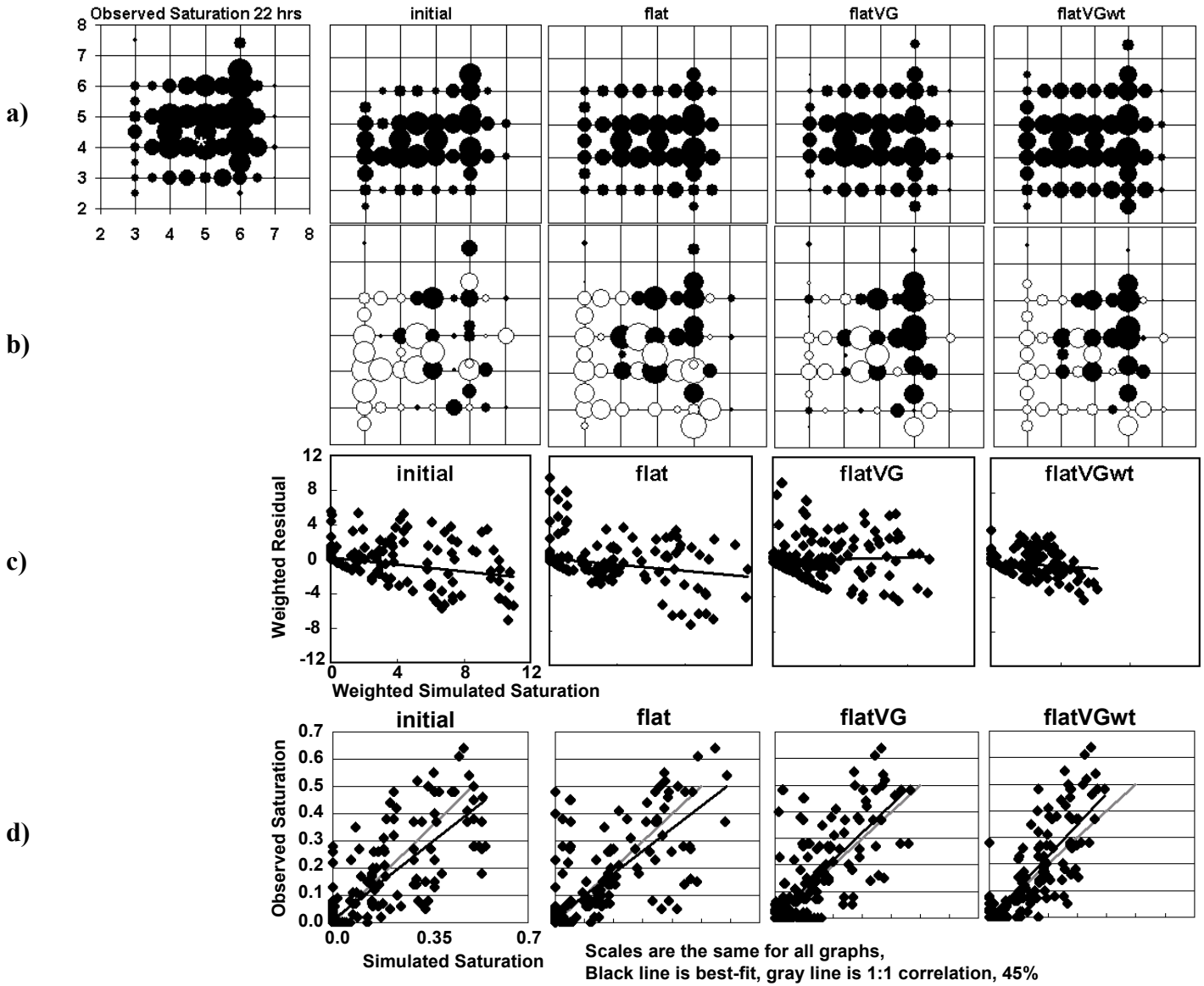

Figure 3.6: Residual analysis: a) spatial distribution of simulated values at 22 hrs; b) residuals at 22 hrs; c) weighted residuals vs. weighted simulated values; and d) simulated versus observed values.

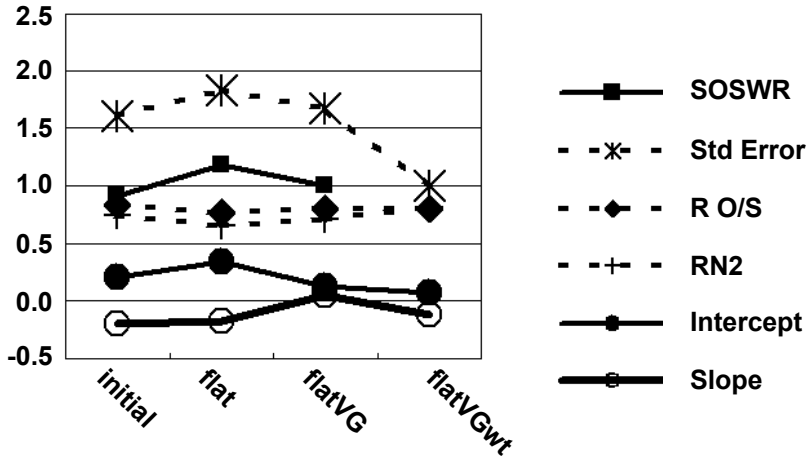

Figure 3.7: Statistical measures to evaluate conceptual models (those represented by dashed lines should approach one while those with solid lines approach zero).

permeability contact surface that pools the PCE below the injection (Figure 3.8). Although the hydraulic divide has been eliminated, the same spatial bias still occurs (Figures 3.6) and the overall fit is not improved (Figure 3.7). Visual inspection of the simulated PCE values indicates the PCE is flowing too far, too fast, in the two-phase flow simulations, especially outside of the channel zone. The fact that the optimal permeability values are higher that the core-derived permeability values (Figure 3.9) supports this conclusion.

The GPR interpretation of PCE saturation represents an average value over a 15-cm thickness and the calibration therefore uses an average simulated saturation from three cells (5 cm each). In the "initial" and "flat" conceptual models with the Brooks-Corey (BC) equation (Brooks and Corey, 1966) for the capillary pressure-saturation relationship in 3D2PHASE, the PCE saturations are much higher in the bottom cell, especially at the front of the PCE migration. The use of the van Genuchten (VG) (van Genuchten, 1980) capillary pressure-saturation relationship can dramatically affect the results of multiphase flow simulations, with the BC curve producing thinner, more extensive PCE pools than those simulated with the VG curve (Rathfelder and Abriola, 1998). The primary difference between these formulations is the use of a specified initial displacement pressure for the BC relationship. The 3D2PHASE code was modified for this study to use the van Genuchten formulation, and the third conceptual model (flatVG) incorporates the van Genuchten formulation of the capillary pressure-saturation relationship instead of the Brooks-Corey formulation. This improves the overall fit and residual distribution over the "flat" model but does not produce fit statistics as desirable as the initial model (sum-of-squares and standard error, Figure 3.7). The lack of improvement in overall fit statistics is due to the large residuals in the channel zone where the GPR interpretation indicates much higher PCE saturations.

Bias towards larger residuals at high PCE saturation led to the evaluation of a different weighting scheme. Although adjusting weights cannot correct for consistent bias in measurement error, the fourth model (flatVGwt) uses a weighting-scheme defining

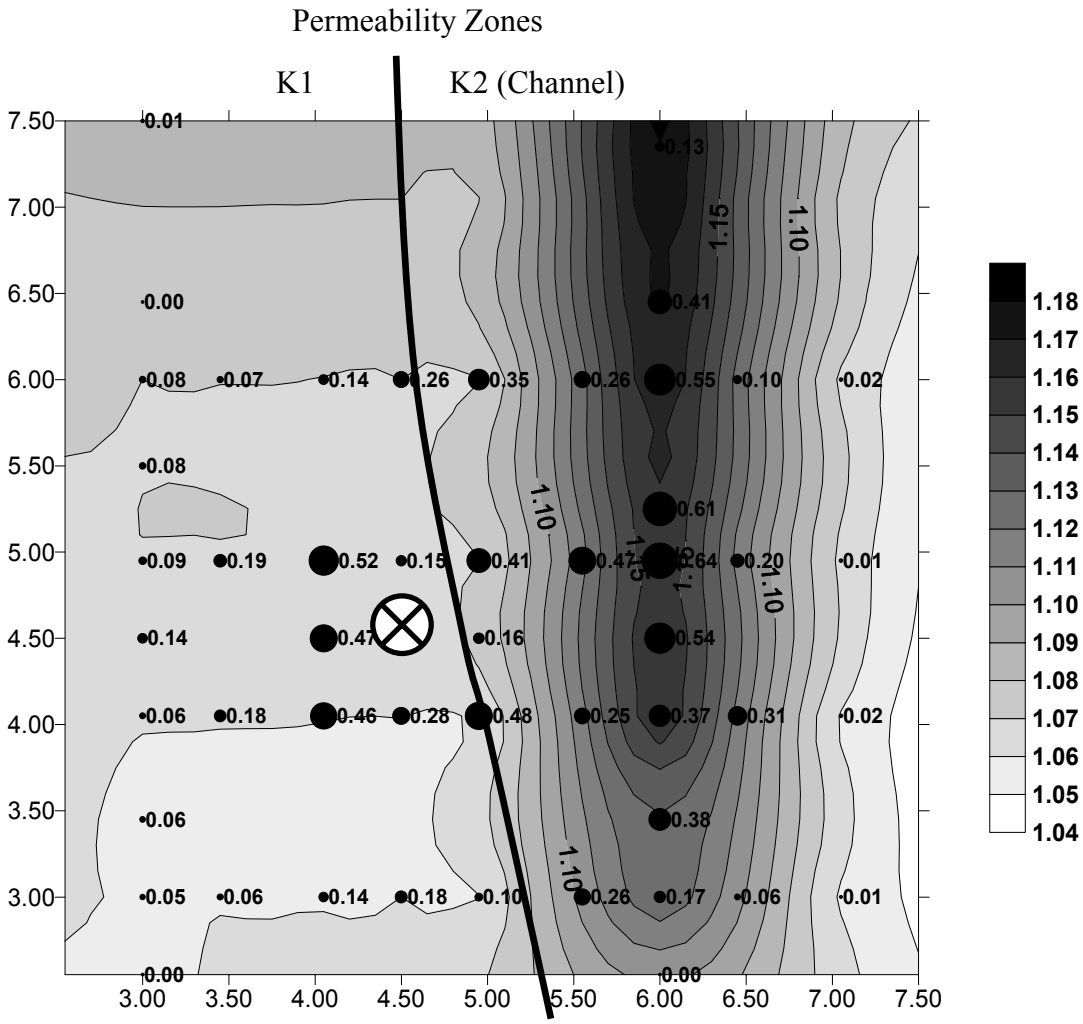

Figure 3.8: Contours of depth to "flattened" low permeability contact where DNAPL spreads (darker areas are deeper) and circles are proportional to DNAPL saturation 22 hours after injection began.

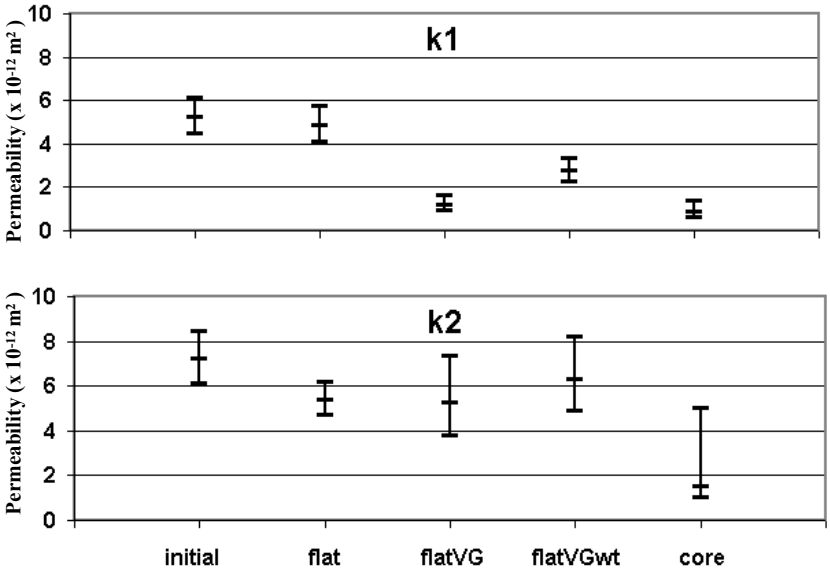

Figure 3.9: Summary of optimal intrinsic permeabilities for conceptual models with 95% confidence intervals.

greater uncertainty for higher saturation observations. Initially, observations had equal weighting assuming a 95% confidence that the saturation was within 10% of the true value. The alternate scheme assumes 95% confidence the saturation was within 10% for observed saturations of 0.0-0.2, 15% for saturations from 0.2-0.4, and 20% for saturations above 0.40. The improved fit and standard error of one (Figure 3.7, note the change in weighting prevents comparison of the SOSWR so it is not plotted) suggest that there is a problem with the accuracy of the high saturations. Because weighting cannot correct bias, the biased residuals remain (Figure 3.6). In spite of the improved fit, the estimated and measured permeability values did not match as well (Figure 3.9). As a result, approaches to identifying possible errors in the GPR saturation estimates are considered.

3.8 Errors Associated with Ground Penetrating Radar Interpretation

Sneddon and others (2002) discuss possible errors in the GPR interpretations that are difficult to quantify, but result from violations of assumptions used in the procedure. The 1D GPR interpretation is based on the assumption that the GPR trace is one-dimensional in infinite, horizontal layering. Much of the DNAPL flow from 0 to 22 hours occurs in zones of uniform properties in the horizontal direction, but the concave channel focuses GPR rays toward the 1D vertical line of interpretation, resulting in shorter travel time and greater amplitude of the GPR wave, which leads to overestimation of DNAPL thickness and saturation (Figure 3.10). Another assumption is that the GPR response is received from one vertical line below the point of interpretation; however, the GPR antenna senses the electromagnetic response from a zone of influence around that line (Lucius and Powers, 1997). Consequently, in areas where DNAPL is present at higher saturations adjacent to the line, such as near the injection (Figure 3.10) the shortened travel time causes underestimation of depth to the surface of the low permeability layer. This is the justification for the lowered elevation of the permeability contrast under the injection

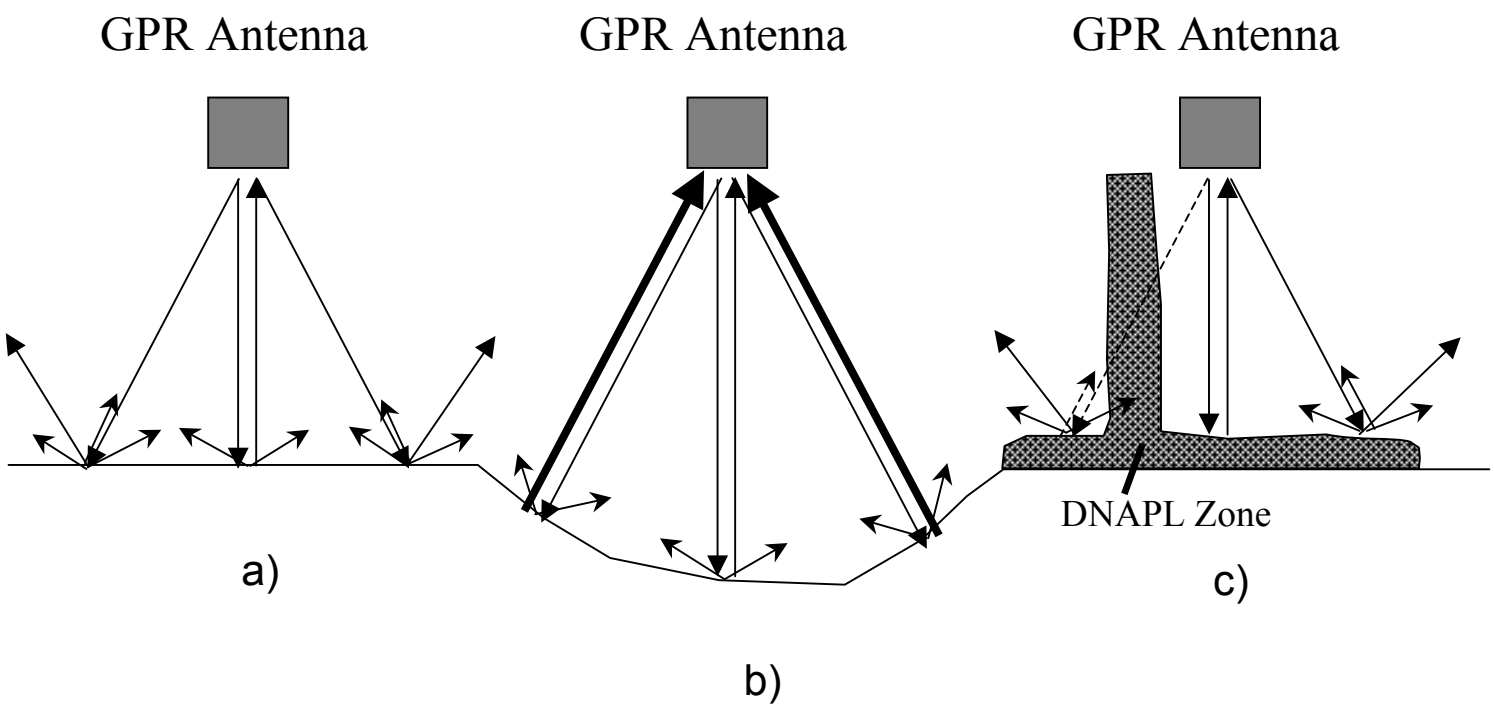

Figure 3.10: Sources of error in 1D GPR interpretation of DNAPL saturation due to two-dimensional affects: a) reflections from a flat interface; b) focusing of GPR rays within a channel; and c) response from a DNAPL zone, GPR wave travel times are decreased within the DNAPL zone (dashed lines).

zone, which creates the "flat" conceptual model. Use of prespill GPR data could avoid this problem, but at the Borden site, the location of the low permeability layer at ~1 m is not distinct enough to be identified until it is highlighted with PCE (Figure 3.2). Additional error in the GPR interpretation may result from use of an incorrect starting wavelet (the actual wavelet was not measured during the experiment). According to Sneddon and others (2002), use of an incorrect starting wavelet can alter the interpreted depth to DNAPL and may be the cause of the multiple occurrences of high amplitude that led to the initial interpretation of two separate DNAPL zones with depth.

Three approaches were taken to evaluate the character, magnitude and influence of these errors, including: flow simulation experiments to evaluate the influence of such errors on the multiphase flow inversion; GPR modeling experiments to estimate the potential magnitude of the errors; and laboratory experiments to determine whether the theoretical errors are observed in practice.

Two flow simulation experiments assess the overestimation of DNAPL saturations in the channel. First, the "flatVG" model is inverted omitting the observations in the channel, producing the same optimal permeability values as the inversion with observations in the channel. A second experiment involves inversion using saturation values from a forward simulation of the "flatVG" model as observations. Before undertaking the inversion, the saturation values in the channel were inflated by a factor of 1.7 (the approximate factor between GPR saturations and those of the "flatVG" model in the channel). Again, the optimal permeability values are essentially the same as obtained using the field observations with similar positive residuals at high DNAPL saturations within the channel. These simulations reveal that bias in DNAPL saturations are reflected in the residuals of the calibrated model, but do not significantly affect the optimal permeability values.

GPR simulations reveal that 1D GPR model calibration overestimates saturation in channel zones. A synthetic model (Figure 3.11) is created using a two-dimensional GPR simulator (Powers, 1997). This synthetic model has uniform background properties

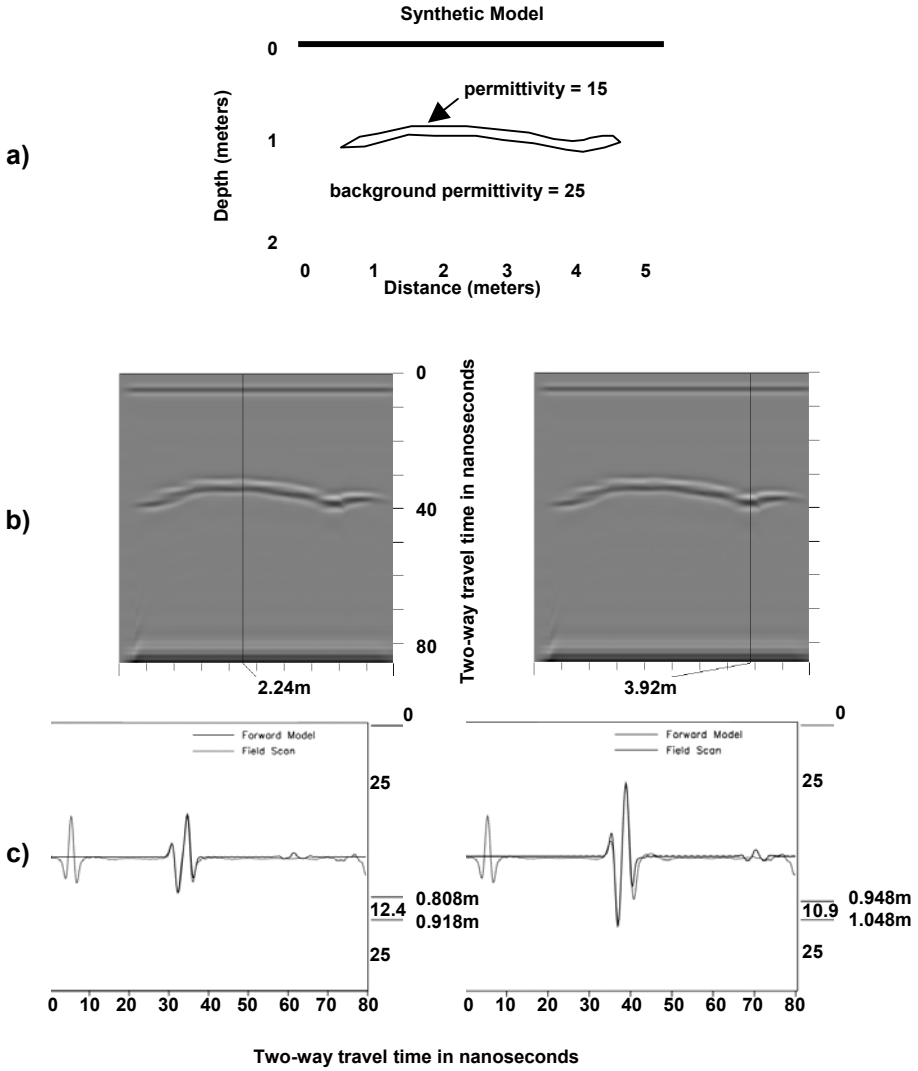

Figure 3.11: Estimation of permittivity generated by a 2D GPR model using 1D GPR models: a) 2D model geometry; b) 2D GPR image; and c) 1D models at different locations.

representing water-filled sand with 40% porosity (permittivity ~ 25) and a zone representing a constant 39% saturation of DNAPL (permittivity ~ 15). Lower permittivity values indicate higher DNAPL saturation and higher permittivity values indicate lower DNAPL saturation. These values can be quantified using the BHS curves as presented in Sneddon and others (2002). The DNAPL zone has variable thickness and elevation as shown in the outlined area of Figure 3.11a. The resulting two-dimensional image of response (Figure 3.11b) delineates the DNAPL in a manner similar to that observed in the field. A 1D GPR model is fit to one-dimensional traces extracted from the 2D model at two locations shown in Figure 3.11b (2.24 m and 3.92 m, with the same constant gain function). At 2.24 m, the DNAPL zone is a relatively flat, uniform-thickness horizontal slab, while at 3.92 m DNAPL fills a channel. The resulting 1D model fits (Figure 3.11c) reveal the influence of the DNAPL zone geometry on the estimated DNAPL permittivity. The channel geometry creates an amplified reflection at the 3.92-m interpretation, leading to an underestimation of the permittivity and an associated overestimation of the DNAPL saturation.

The error in the GPR interpretation within the channel zone demonstrates the overall difficulty with the non-unique nature of the GPR modeling procedure. As discussed previously, in the 1D GPR models of the Borden data, the constant gain function (affects reflection amplitude), permittivity, and depth are all unknown parameters. As a result, the constant gain function is fixed for all GPR models and the GPR interpretation attempts to focus on reflection arrival times (Sneddon and others, 2002). However, this creates a problem for the modeler because the permittivity and depths are still unknown. The assumption of a permittivity of 25 for the water-saturated sand creates a unique depth for the top of the DNAPL zone, but still leaves the DNAPL thickness and permittivity in question. As a result, the GPR modeler has no choice but to rely on the reflection amplitude created by a contrast in permittivity for model calibration. This problem creates the error in the GPR interpretation within the channel where DNAPL reflections are amplified and interpreted as higher DNAPL saturations.

The ultimate reliance on reflection amplitude can also create an overall bias in the interpreted permittivity values for all 1D GPR model locations. This overall bias is demonstrated in Figure 3.11c for a 1D GPR trace from the 2.24-m point (Figure 3.11a). The arrival time for the DNAPL zone is correctly modeled as long as the water-saturated sand is represented with a permittivity of 25. The problem is picking the correct DNAPL thickness and permittivity. In the given example, a permittivity of 12.4 and a thickness of 0.11 m produce a good calibration of reflection arrival times and reflection amplitudes. The true thickness of 0.09 m and a permittivity of 15 produce the correct arrival times in the 1D model, but not the correct amplitudes. This occurs because the GPR modeler does not know the correct constant gain function to use in the 1D GPR model. The use of the constant gain function from the original 2D model produces the correct permittivity of 15 (by matching the amplitude) and a thickness of 0.09 m. For the Borden GPR data, error in picking the improper constant gain function would produce a consistent error with high or low DNAPL saturations throughout the interpreted domain. The possible amount of this consistent error is not examined, but consistent error in the Border GPR interpretation is not seen in the best alternative conceptual models (flatVG and flatVGwt). The difficulty in determining the constant gain function occurs because the absolute output power of the GPR antenna is not known (Powers, 2003); however, knowledge about reasonable permittivity variations can constrain the constant gain function that is selected.

Laboratory experiments confirm the overestimation of saturation from GPR data due to the focusing of GPR rays (Johnson and Poeter, 2003). Pre- and post-spill GPR surveys of a small sand tank with DNAPL pooling along a clay base indicate that 1D modeling of the GPR overestimates saturation of DNAPL near the location where two clay slopes meet in the corner of the tank. This multidimensional nature of the GPR reflections near the corner of the tank is not accounted for in the 1D GPR modeling. In addition, the non-uniqueness in the GPR interpretation is overcome by knowing the depth to reflection interfaces (clay interface and a steel sheet) and modeling only reflection arrival times.

3.9 Summary and Conclusions

The goal of inverse modeling is to test alternative conceptual models and identify optimal parameter values for the most representative model(s). If measurement error is random, then biased residuals can be used to guide construction of better conceptual models. Bias in observation measurements may indicate conceptual model error when none exists.

Synthetic test cases show that saturation data alone are sufficient to estimate optimal intrinsic permeability values when other model parameters are known, as is the case in this study. However, the character and magnitude of error in the observation data are critical to accurately estimating permeability values. If observation errors indicate physically improbable trends in the dependent variable (e.g., DNAPL saturation decreases with time during constant injection) at critical locations, or the errors are large, then permeability values will not be accurately estimated.

Synthetic simulations of the Borden injection illustrate that artificially biased observation data produce biased residuals similar to those observed in this evolution of conceptual models, yet still produce accurate optimal permeability values. Accurate optimal permeability values are also produced in a case where no channel observations are provided. These findings indicate that the resulting optimal permeability values are not substantially influenced by bias in the observation data within the channel.

Exploration of the source of bias (conceptual model versus measurement) using flow simulation experiments, GPR modeling experiments, and laboratory experiments, reveal that DNAPL saturations are overestimated in the channel due to GPR ray focusing which results in biased residuals from model calibration. In addition, the GPR modeling experiments indicate that consistent bias in DNAPL saturations could occur throughout the interpreted domain, but are not readily apparent in the Borden GPR data. Reasonable optimized permeability values (based on laboratory measurements of core samples) are estimated for all conceptual models, but the effort to improve fit and reduce residual bias

yielded optimal permeability values closer to the field measurements. Consequently, an effort to improve model fit and reduce residual bias is useful in decreasing conceptual model error even though it cannot compensate for bias in observations. The remaining bias can then be used as a tool to identify possible errors in the observations, especially when the bias in observation data is difficult to assess. In this way, the use of inverse multiphase flow simulations provides a unique opportunity for improving the GPR interpretation.

3.10 References

Bolha, J., 1986, A sedimentological investigation of a prograding foreshore sequence: C.F.B. Borden, M.Sc. Thesis, University of Waterloo, Waterloo, Ontario, Canada.

Brewster, M. L., Annan, A. P., Greenhouse, J. P., Kueper, B. H., Olhoeft, G. R., Redman, J. D. and Sander, K. A., 1995, Observed migration of a controlled DNAPL release by geophysical methods: *Ground Water*, **33**, pp. 977-987.

Brooks, R. H., and Corey, A. T., 1966, Properties of porous media affecting fluid flow. *J. Irrig. Drain. Div*., ASCE, **92**, pp. 61-88.

Doherty, J., 1994, PEST: Corinda, Australia, Watermark Computing, 122 p.

Gerhard, J. I., B. H. Kueper, and G. R. Hecox, 1998, The influence of waterflood design on the recovery of mobile DNAPLs. *Ground Water*, **36**(2), pp. 283-292.

Greenhouse, J., Brewster, M., Schneider, G., Redman, D., Annan, P., Olhoeft, G.,Lucius, J., Sander, K. and Mazzella, A., 1993, Geophysics and solvents: The Borden experiment*, Leading Edge*, **12**(4), pp. 261-267.

Hill, M. C., 1992, A computer program (MODFLOWP) for estimating parameters of a transient, three-dimensional, ground-water flow model using nonlinear regression, U. S. Geological Survey Open File Report 91-484, 102 p.

Hill, M. C., 1998, Methods and guidelines for effective model calibration, U. S. Geological Survey Water-Resources Investigations Report 98-4005, 90 p.

Hill, M.C., Banta, E.R., Harbaugh, A.W., and Anderman, E.R., 2000, MODFLOW-2000, the U.S. Geological Survey modular ground-water model -- User guide to the Observation, Sensitivity, and Parameter-Estimation Processes and three post-processing programs: U.S. Geological Survey Open-File Report 00-184, 210 p.

Johnson, R. H. and Poeter, E. P., 2003, Interpreting DNAPL saturations in a laboratory-scale injection with GPR data and direct core measurements, U. S. Geological Survey Open File Report, in review.

Kueper, B. H. and Frind, E. O., 1991a, Two-phase flow in heterogeneous porous media: 1. model development, *Water Resources Research*, **27**(6), pp. 1049-1057.

Kueper, B. H. and Frind, E. O., 1991b, Two-phase flow in heterogeneous porous media: 2. model application, *Water Resources Research*, **27**(6), pp. 1057-1070.

Lucius, J. E. and Powers, M.H., 1997, Multi-frequency GPR surveys, *in* SAGEEP '97 Proceedings, Symposium on the Application of Geophysics to Environmental and Engineering Problems, Environmental and Engineering Geophysics Society, **1**, pp. 355-364.

McCray, J.E. and Brusseau, M.L, 1998, Cyclodextrin-enhanced in-situ flushing of multiple-component immiscible organic-liquid contamination at the field scale: Mass removal effectiveness, *Environ. Sci. Tech.*, **32**(9), pp. 1285-1293.

National Research Council (NRC), 1994, *Alternatives for Ground Water Cleanup*, National Academy Press, Washington, D. C.

Poeter, E.P. and M.C. Hill, 1996, Unrealistic parameter estimates in inverse modeling: A problem or a benefit?, Proceedings of ModelCare'96, Golden CO, IAHS/AISH Publication, pp. 277-286.

Poeter, E. P. and Hill, M. C., 1997, Inverse models: A necessary next step in groundwater modeling, *Ground Water*, **33**(6), pp. 889-904.

Poeter, E. P. and Hill, M. C., 1998, Documentation of UCODE, A computer code for universal inverse modeling, U.S. Geological Survey: Water-Resources Investigations Report 98-4080, 116 p.

Powers, M.H., 1997, Modeling frequency-dependent GPR, *Leading Edge*, **16**(11), pp. 1657-1662.

Powers, M.H., 2003, Personal communication.

Powers, M. H., Duke, S. K., Huffman, A. C., and Olhoeft, G. R., 1992, GPRMODEL: One dimensional full waveform forward modeling of ground penetrating radar data, U.S. Geological Survey Open File Report 92-532, 22 p. + floppy disk.

Rathfelder, K., and Abriola, L. M., 1998, The influence of capillarity in numerical modeling of organic liquid redistribution in two-phase systems, *Adv. Water Resour.,* **21**(2), pp. 159-170.

Redman, J. D., 1992, Geophysics and the solvents-in-groundwater program, *in* Proc. Of Symposium on the Application of Geophysics to Engineering and Environmental Problems, April 26-29, 1992, Oakbrook, Illinois, **2**, Society of Engineering and Mineral, Golden, CO, pp. 375-382.

Redman, J. D., and Kueper, B. H., 1992, Core permeability data, University of Waterloo and Queen's University, Internal Document.

Sander, K.A., 1994, Characterization of DNAPL Movement in Saturated Porous media Using Ground Penetrating Radar, Colorado School of Mines, Master's Thesis, ER-4336.

Sander, K. A., and Olhoeft, G. R., 1994, 500-MHz ground penetrating radar data collected during an intentional spill of tetrachloroethylene at Canadian Forces Base Borden in 1991, USGS. Digital Data Series DDS-25, CD ROM.

Sneddon, K. W., Powers, M. H., Johnson, R. H., and Poeter, E. P., 2002, Modeling GPR data to interpret porosity and DNAPL saturations for calibration of a 3-D multiphase flow simulation U.S. Geological Survey Open-File Report: 02-451, 29 p.

Sudicky, E. A., 1986, A natural gradient experiment on solute transport in a sandy aquifer: Spatial variability of hydraulic conductivity and its role in the dispersion process, *Water Resources Research*, **22**(13), pp. 2069-2082.

Turcke, M.A. and Kueper, B.H., 1996, Geostatistical analysis of the Borden aquifer hydraulic conductivity field, *Journal of Hydrology*, **178**, pp. 223-240.

van Genuchten, M.T., 1980, A closed-form equation for predicting the hydraulic conductivity of unsaturated soils, *Soil Sci. Soc. Am. J.*, **44**, pp. 892-898.

Chapter 4

INTERPRETING DNAPL SATURATIONS IN A LABORATORY-SCALE INJECTION WITH GPR DATA AND DIRECT CORE MEASUREMENTS

4.1 Abstract

Ground penetrating radar (GPR) is used to track a DNAPL injection in a laboratory sand tank. Before data reduction, GPR data provide a qualitative measure of DNAPL saturation and movement. One-dimensional (1D) GPR modeling provides a quantitative interpretation of DNAPL volume within a given thickness during and after the injection. This is confirmed qualitatively by visual inspection of cores and two-dimensional GPR modeling. DNAPL saturation in sub-layers of that thickness could not be quantified because calibration of the 1D GPR model is non-unique when both permittivity and depth of multiple layers are unknown. Accurate quantitative interpretation of DNAPL volumes using 1D GPR modeling requires: 1) identification of a suitable target that produces a strong reflection and is not subject to any multidimensional interference; 2) knowledge of the exact depth of that target; and 3) use of two-way radar-wave travel times through the medium to the target to determine the permittivity of the intervening material, which eliminates reliance upon reflection amplitude. With geologic conditions that are suitable for GPR surveys (i.e., shallow depths and low electrical conductivities), the procedures in this laboratory study can be adapted to a field site to identify DNAPL source zones after a release has occurred.

4.2 Introduction

The identification of dense non-aqueous phase liquids (DNAPLs) in the subsurface is the first step toward remediation of an area affected by organic contaminants. Since DNAPLs are the source zone for dissolved constituents, the removal or isolation of the pure phase DNAPL is a priority for successful remediation. Identification of DNAPL source zones has traditionally relied upon the use of soil cores and monitoring wells. Analyses of soil cores can provide quantitative values for DNAPL saturation with depth. Monitoring wells can provide direct evidence of DNAPL due to the accumulation of free product, but do not provide the distribution of DNAPL saturations with depth. Both require a large expense, and drilling risks the remobilization of residual DNAPL zones. Dissolved concentrations of organic contaminants in monitoring wells outside of the source zone provide indirect evidence of possible DNAPL source zone locations.

Geophysical methods are an attractive alternative for the detection of DNAPL source zones because they are non-intrusive and time effective. Qualitative information is readily acquired, but acquisition of quantitative DNAPL saturations requires detailed analysis of the geophysical data and favorable geologic conditions. A variety of geophysical methods were used at the Canadian Forces Base Borden in a 9 m by 9 m controlled field cell where perchloroethylene (PCE) was intentionally spilled and monitored (Brewster and others, 1995; Greenhouse and others, 1993). The ground penetrating radar data (GPR) from this PCE spill was analyzed to determine the distribution of DNAPL saturations (Sneddon and others, 2002) and used to calibrate a multiphase flow simulation (Johnson and Poeter, 2003a). The calibration statistics from Johnson and Poeter (2003a) led to the conclusion that the interpretation of the GPR data may be biased, especially in a channel where focusing of the GPR rays could lead to an overestimation of DNAPL saturation. However, it was not possible to determine whether the biased residuals resulted from error in the GPR interpretation or inaccuracies in the multiphase flow model. This research was designed to study the accuracy of DNAPL

saturations interpreted from GPR data. GPR data were collected in a small sand tank during a spill of a non-toxic DNAPL. The GPR data were analyzed before, during, and after the spill to confirm the known geologic arrangement and quantify DNAPL saturations. Cores were taken postspill, cut in sections and weighed to independently determine DNAPL saturations.

4.3 Tank Design and Data Collection

A sand tank was created by lining a plastic container with clay to create the desired geometry (Figures 4.1 and 4.2). Angled clay walls were used to evaluate the affect of a channel in two-dimensions and a bowl in three-dimensions on the GPR response. A steel rod was placed in the tank and a steel sheet was placed below the tank to provide known targets for the GPR interpretation. The tank was filled with tap water that was de-aired by boiling and #45 Ottawa silica sand from U. S. Silica Company was sifted manually into the tank. Deposition of the sand through the water created layers of slightly varying sand sizes because the sand grains separated as they fell through the water column (Figure 4.3). Coarse sand lenses on the order of 0.5 to 1.0 cm thick were flat to slightly sloped (darker color in Figure 4.3) with thin intervening layers of fine sand on the order of 0.1 to 0.3 cm thick (lighter color).

The tank geometry included 2.54 cm of water-saturated sand below the bottom of the clay to allow for coring and a 1.27 cm thick Plexiglas sheet that covered the tank (Figures 4.1 and 4.2). The Plexiglas sheet was used to create a dry, smooth surface for the GPR antenna. Two outlet ports (2.54 cm in diameter) were installed at the top of the sand, one in the northeast corner of the tank and one in the southwest corner of the tank to allow water to flow out of the tank as the DNAPL was injected. As discussed later, GPR data indicated that the upper 3.81 cm of sand was not fully saturated. The precise thickness of this unsaturated sand was not independently verified.

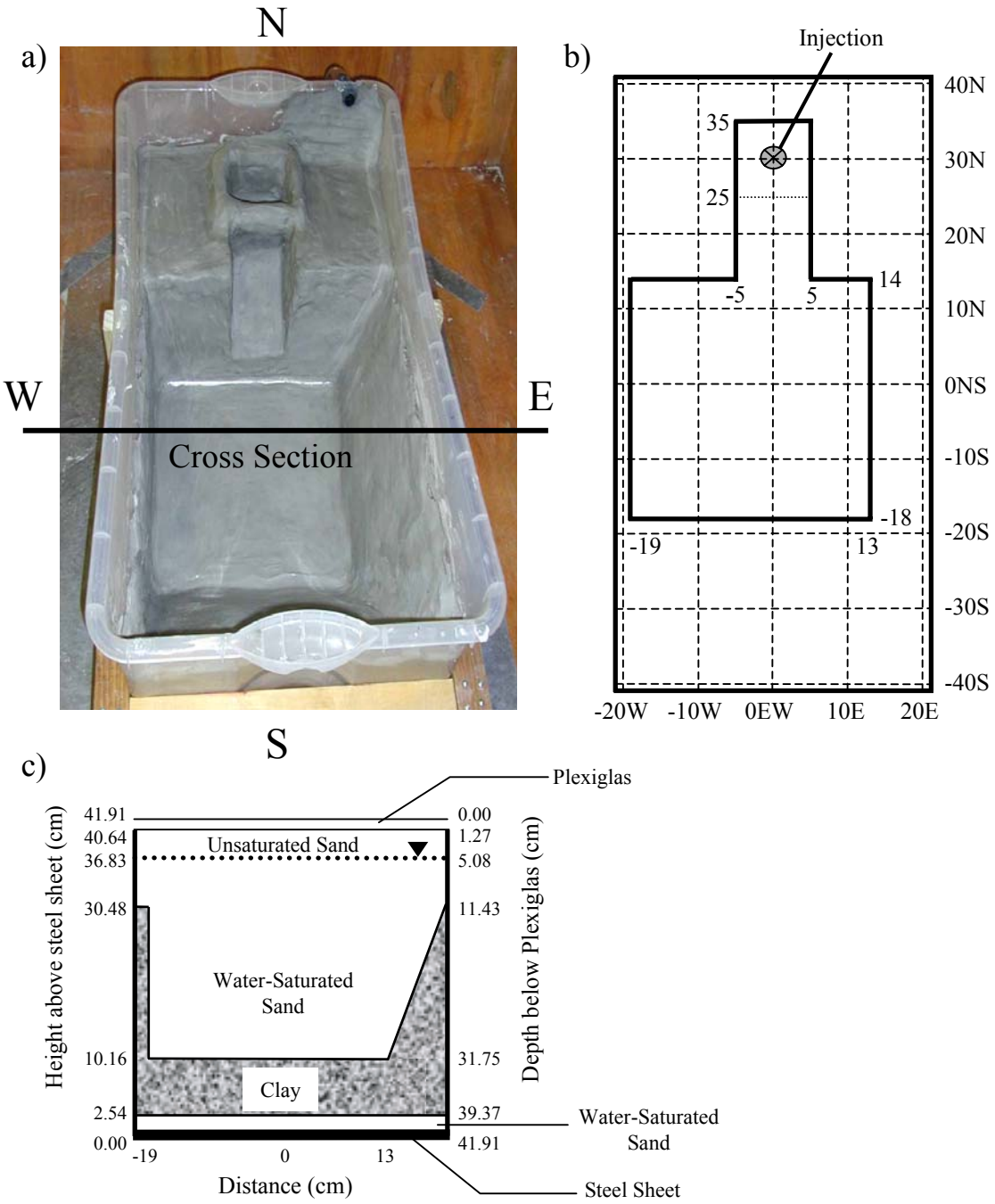

Figure 4.1: Dimensions of sand tank drawn to scale:
a) overhead photo of unfilled tank;
b) overhead dimensions where total tank area is 42 cm x 82 cm; and
c) cross section looking north.

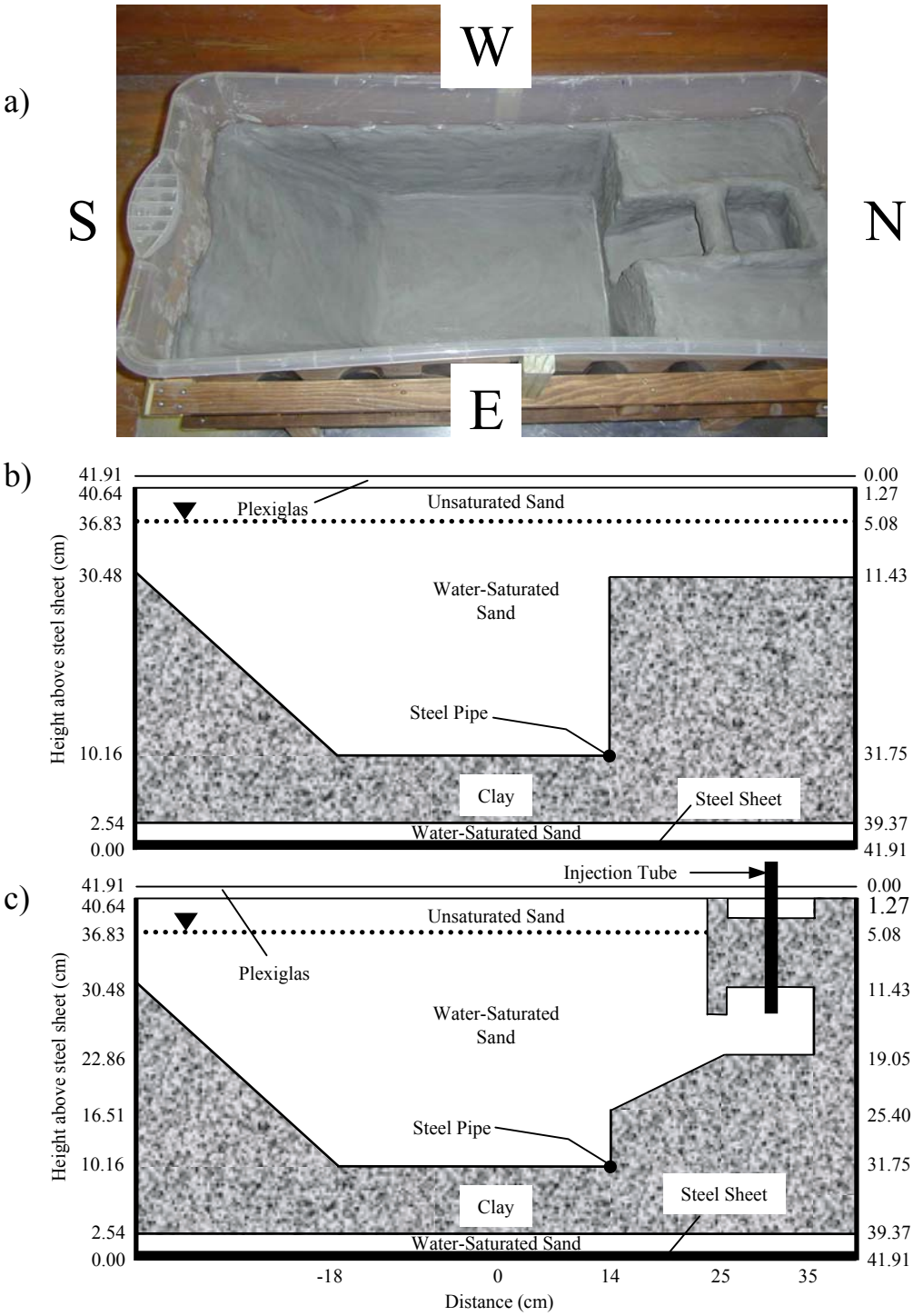

Figure 4.2: Side view of sand tank with dimensions drawn to scale: a) photo of unfilled tank; b) non-center cross section; and c) center cross section.

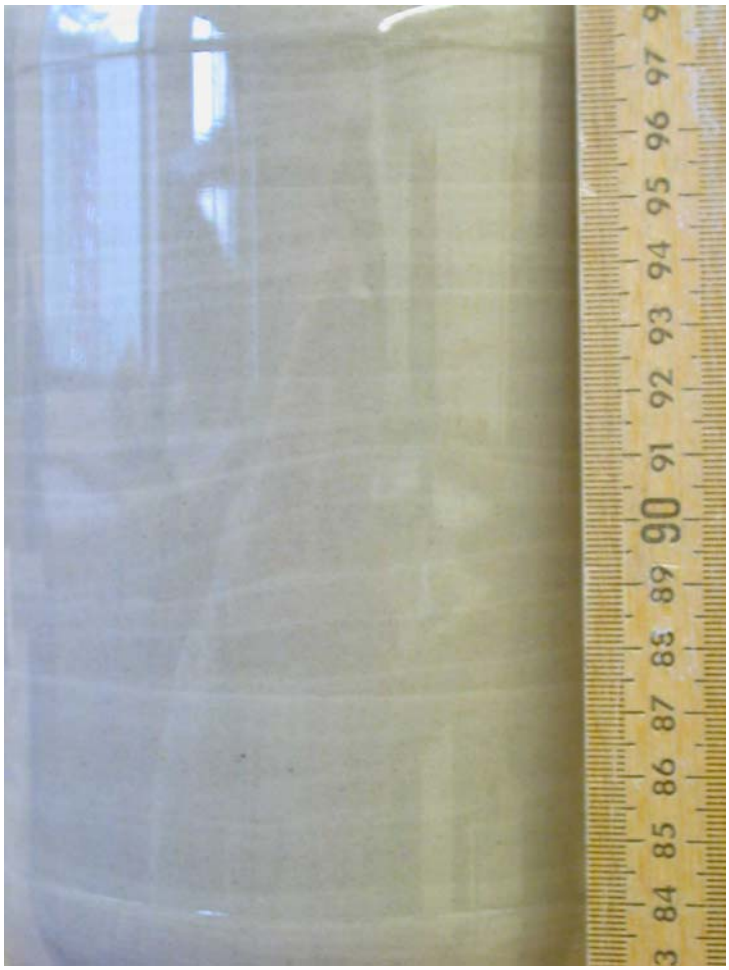

Figure 4.3: View of sand layering.

The DNAPL was 98% hydrofluoroether (HFE-7100) produced by the 3M Company and 2% methyl caprylate, added to allow for the addition of oil red O (0.5 g in every 1000 mL total) because standard organic dyes do not dissolve in HFE. At 20º C, the density of HFE is 1.5 g/mL and methyl caprylate is 0.877 g/mL, resulting in a density of 1.49 g/mL at 20º C for the mixture, which was confirmed by direct measurement. The mixture was injected into the tank through a plastic tube, at a constant head of 19.05 cm above the sand (Figure 4.4). The constant head was maintained by an inlet of dyed HFE, which was constantly circulated via a peristaltic pump, and a free flowing outlet port (Figures 4.4a and 4.5). The whole injection system was sealed to reduce volatile losses and the volume injected was tracked using a graduated cylinder (Figure 4.5a). The injection zone was surrounded by clay to eliminate leakage of HFE to the surface during injection (Figure 4.4b). However, upon postspill disassembly, HFE was seen to have leaked through the clay seal to the north end of the tank. This leak did not occur at the surface, but appeared to follow a fracture in the clay, which allowed the HFE to leak into the small space between the clay and the plastic walls of the tank.

GPR data were collected using a GSSI-SIR10A unit with a 1.5 GHz antenna. Geometric control was maintained using a track system and the pull rate of the antenna was maintained at a relatively constant rate using a motorized pulley system (Figure 4.5). Prespill and postspill GPR data were collected at 1-cm increments and during the spill, GPR data was continuously collected at various locations that provided the most information on the DNAPL movement.

Postspill, clear acrylic core tubes were pushed into the tank and withdrawn for visual analysis and quantitative measurement of DNAPL saturation (Figure 4.6). The sand/clay interface at the bottom of the tank created a seal via the clay and a break in suction via the lower sand, which allowed for easy removal of the cores. The cores were cut into precise increments, weighed, dried, and re-weighed. The known volume of the core and the final mass of the sand, with a known specific gravity, allowed for the calculation of

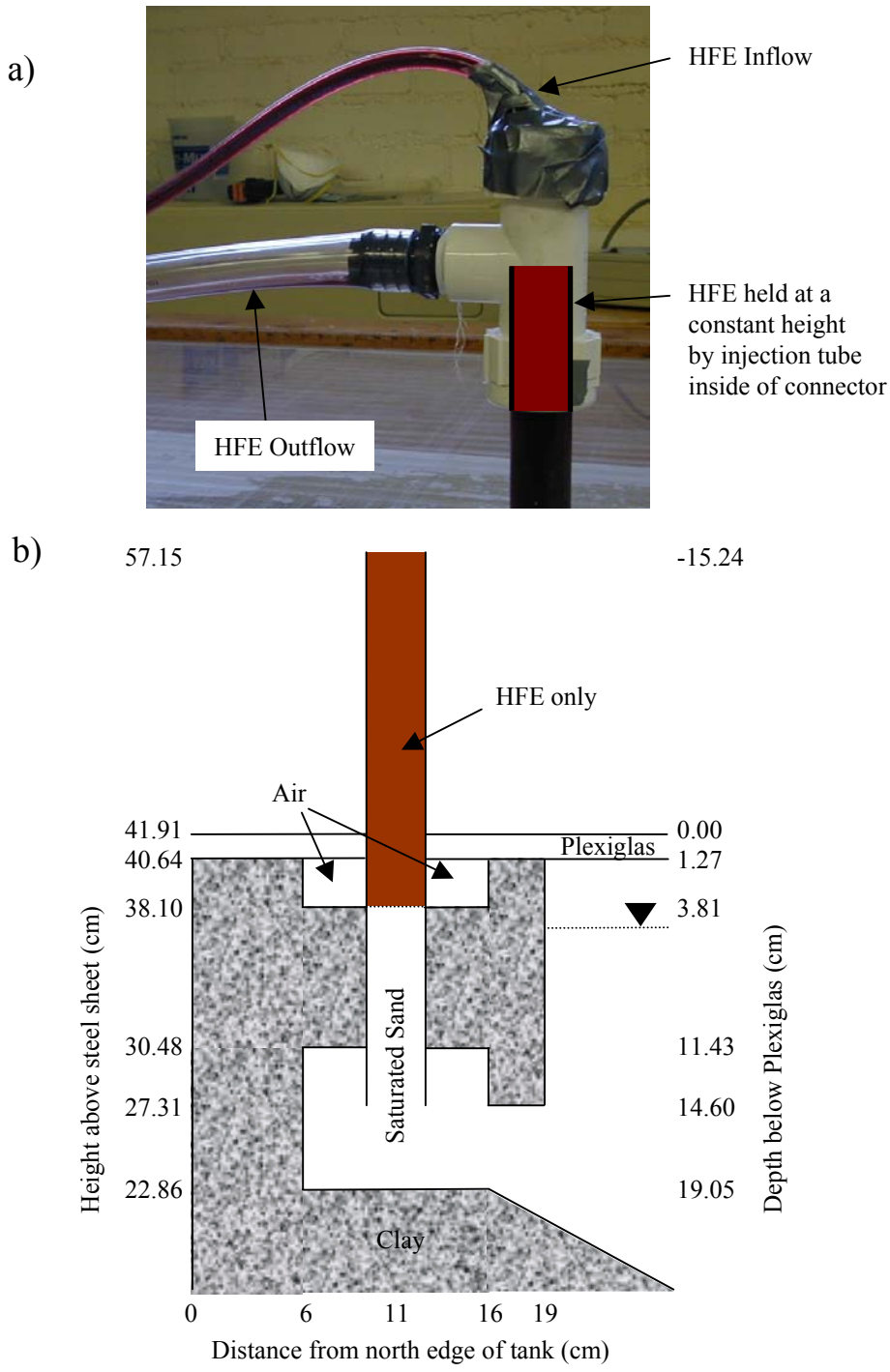

Figure 4.4: Details of the injection system: a) photo of injection system above the Plexiglas; and b) dimensions of injection system drawn to scale.

a)

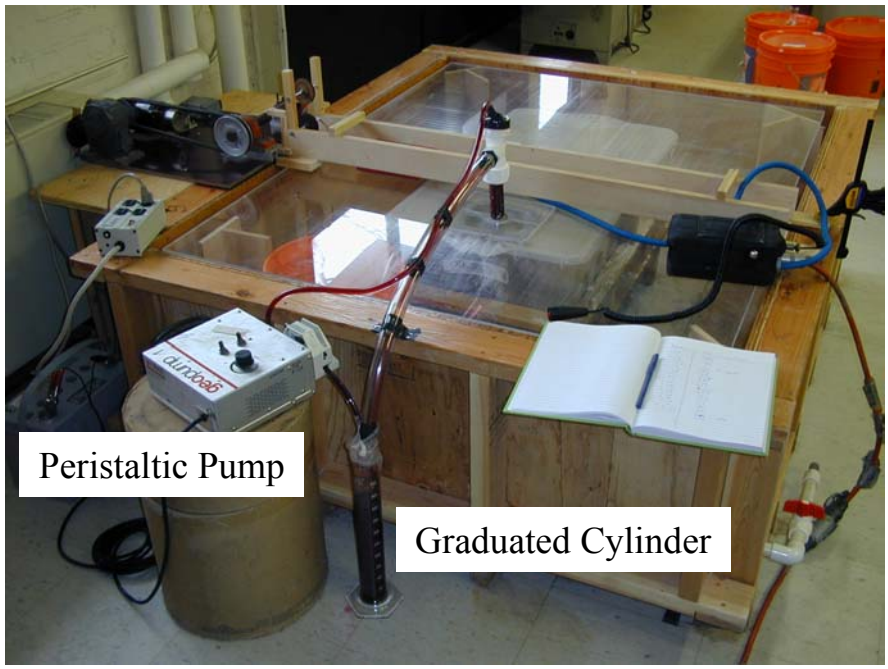

b)

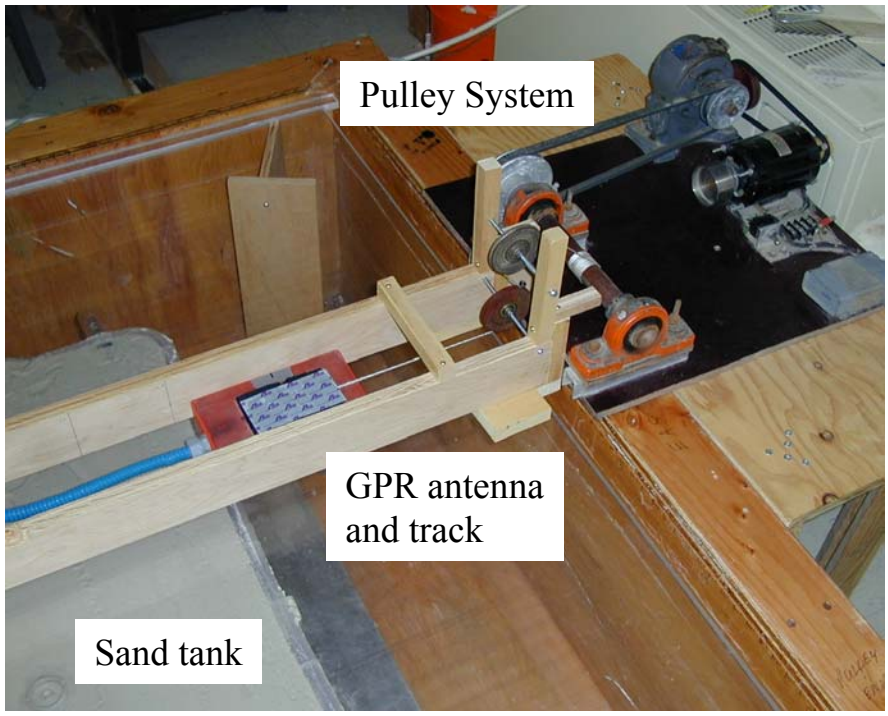

Figure 4.5: Photograph of: a) sand tank, injection system, and GPR antenna track and pulley; and b) close up photograph of GPR antenna, track, and pulley system.

a)

b)

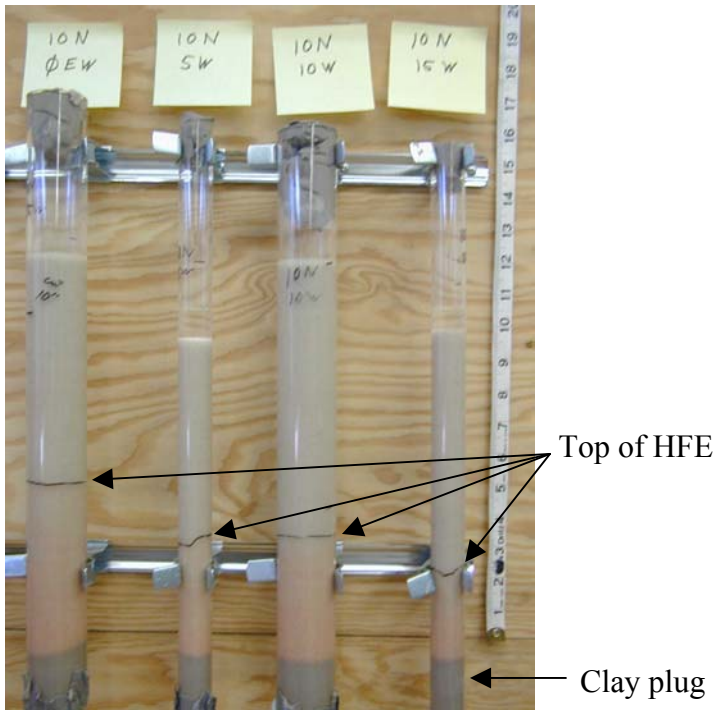

Figure 4.6: Core tubes: a) within sand tank; and b) withdrawn and mounted.

porosity. Excess mass in the pre-dried core, above the mass attributed to the sand and water based on the porosity, could be attributed to the heavier-than-water HFE.

An earlier laboratory-scale DNAPL injections was completed in a larger tank, which was made of wood with a fiberglass lining and is seen surrounding the small sand tank in Figure 4.5. GPR data were collected in a similar manner as the smaller tank, but coring was delayed and the dyed HFE had biodegraded, so DNAPL saturation could not be determined.

4.4 GPR Data

All GPR data were collected in a north-south (Figures 4.7 and 4.8) or an east-west (Figures 4.9 through 4.15) direction across the tank and can be located using the coordinate system in Figure 4.1b. A wiggle-trace plot of the center trace is superimposed on the gray-scale GPR profile of the data. A "snapshot" of the tank at approximately 200 minutes after the start of injection at the profiles 10N to 20S, with a 6-cm interval between each profile shown is presented in Figure 4.9. The same profiles are shown individually in Figures 4.10 through 4.15 with prespill, postspill, and intermediate time data when significant changes in the GPR image occur.

Several key features are consistent in all of the 2D GPR images. Differences in these key features through time are created by HFE flowing into the initially water-saturated sand. Time zero in all the GPR images represents the top of the Plexiglas. A steel sheet is located at 31.75 cm below the top of the Plexiglas and occurs at a time of approximately 14 ns in the prespill GPR images. The steel sheet cannot be seen as distinctly in the north end of the tank because the greater electrical conductivity of the thicker clay attenuates the GPR signal. This same influence is seen at the south, east, and west sides of the tank as the clay thickens, but is not as great in extent. The addition of HFE creates a "pull-up" effect for the reflection of the steel sheet, as seen most

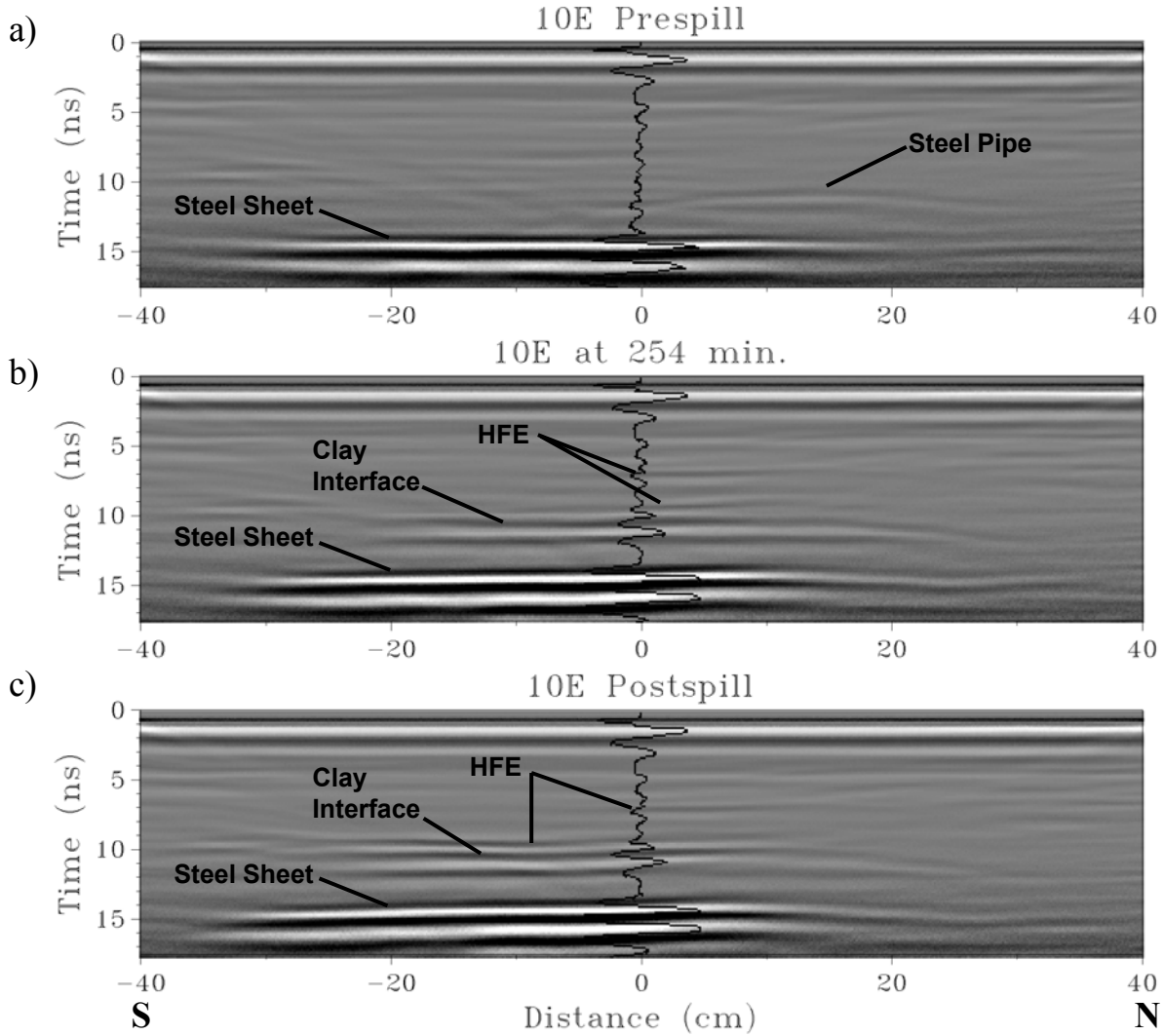

Figure 4.7: GPR data at various times along 10E, looking west. Negative distances are the south end of the tank and positive distances are the north end of the tank. A wiggle-trace display of the center trace is superimposed on the gray-scale profile display.

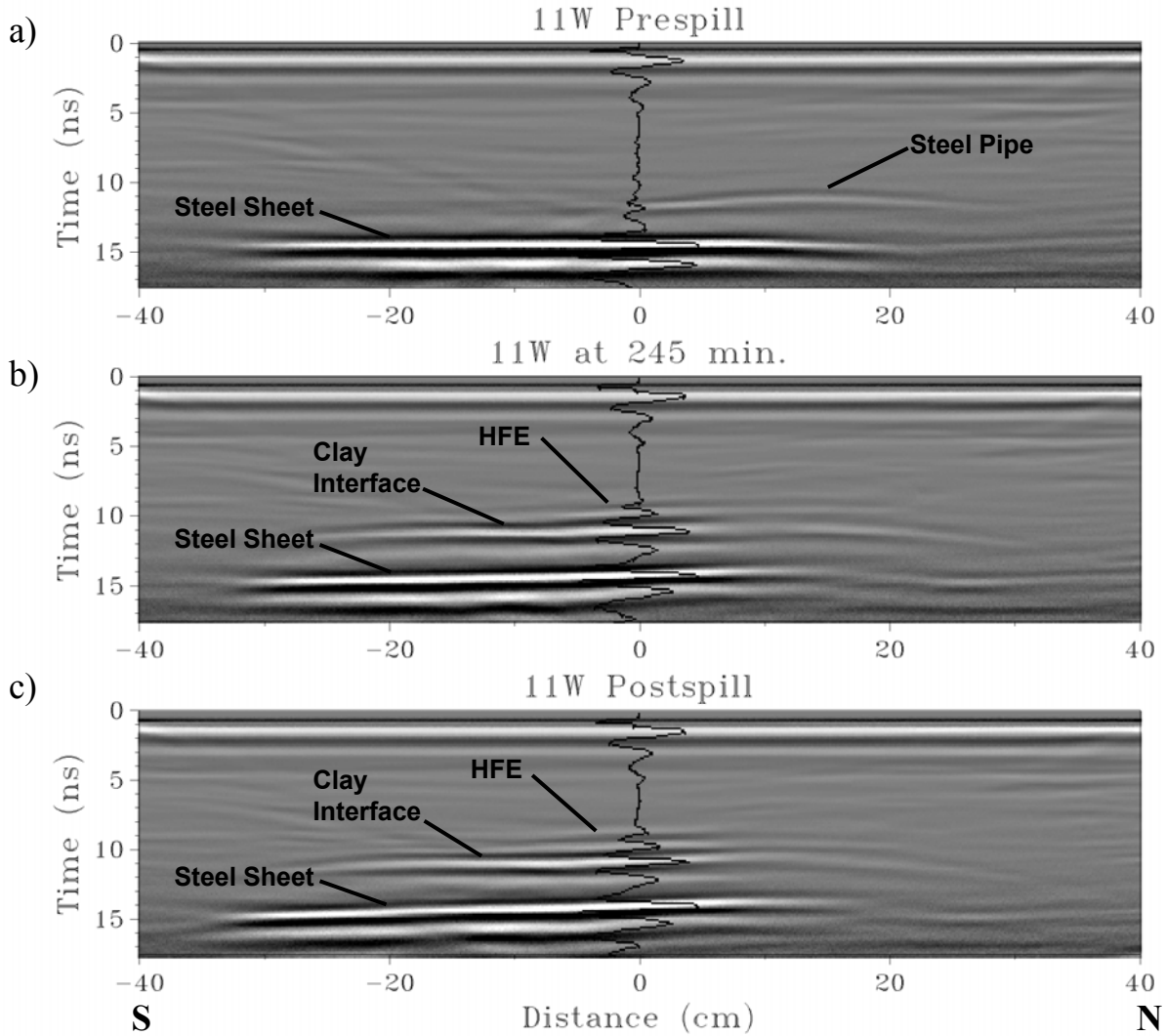

Figure 4.8: GPR data at various times along 11W, looking west.

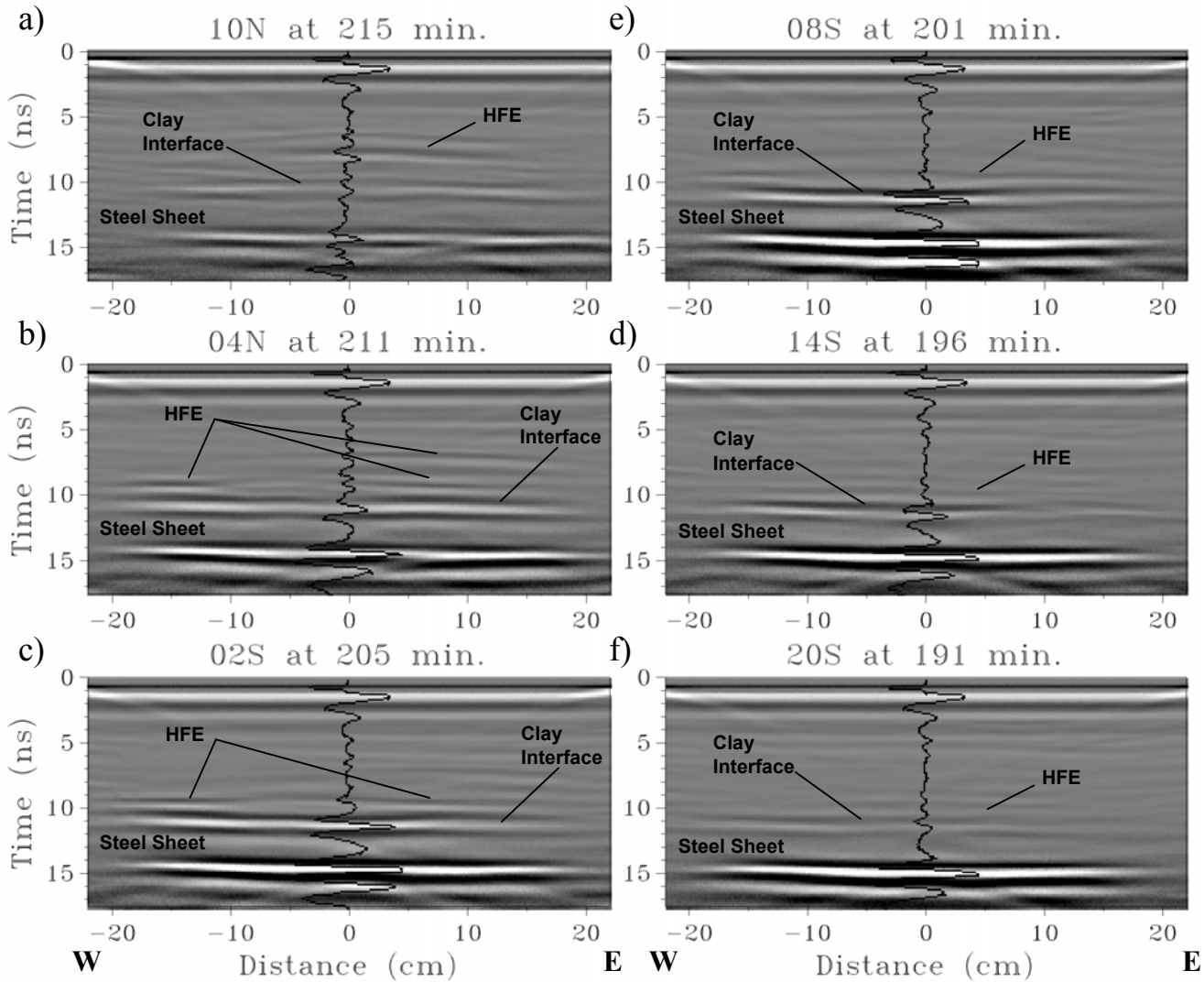

Figure 4.9: GPR data at various E-W cross sections at approximately 200 minutes, looking north. Negative distances are the west end of the tank and positive distances are the east end of the tank.

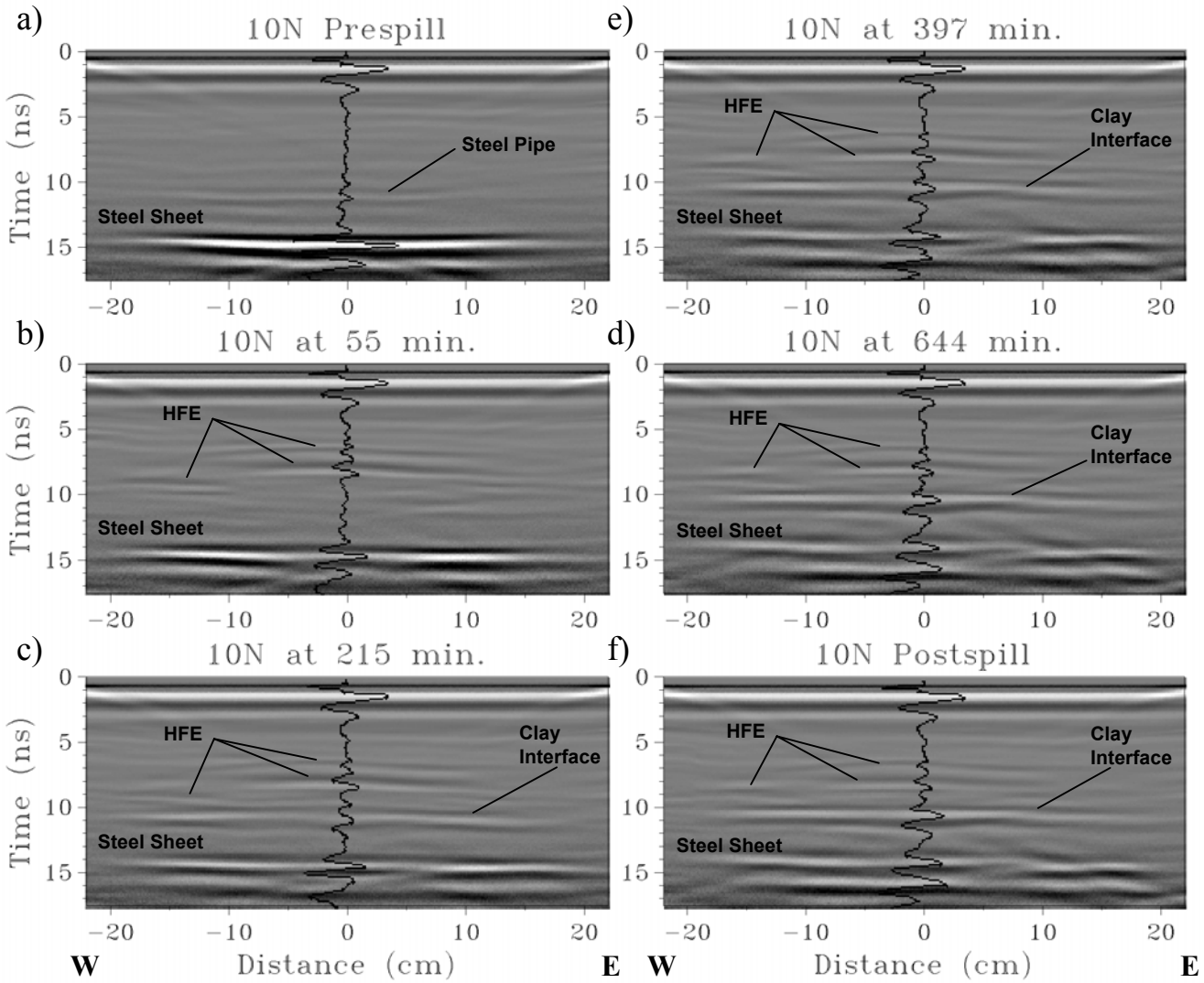

Figure 4.10: GPR data at various times along 10N, looking north.

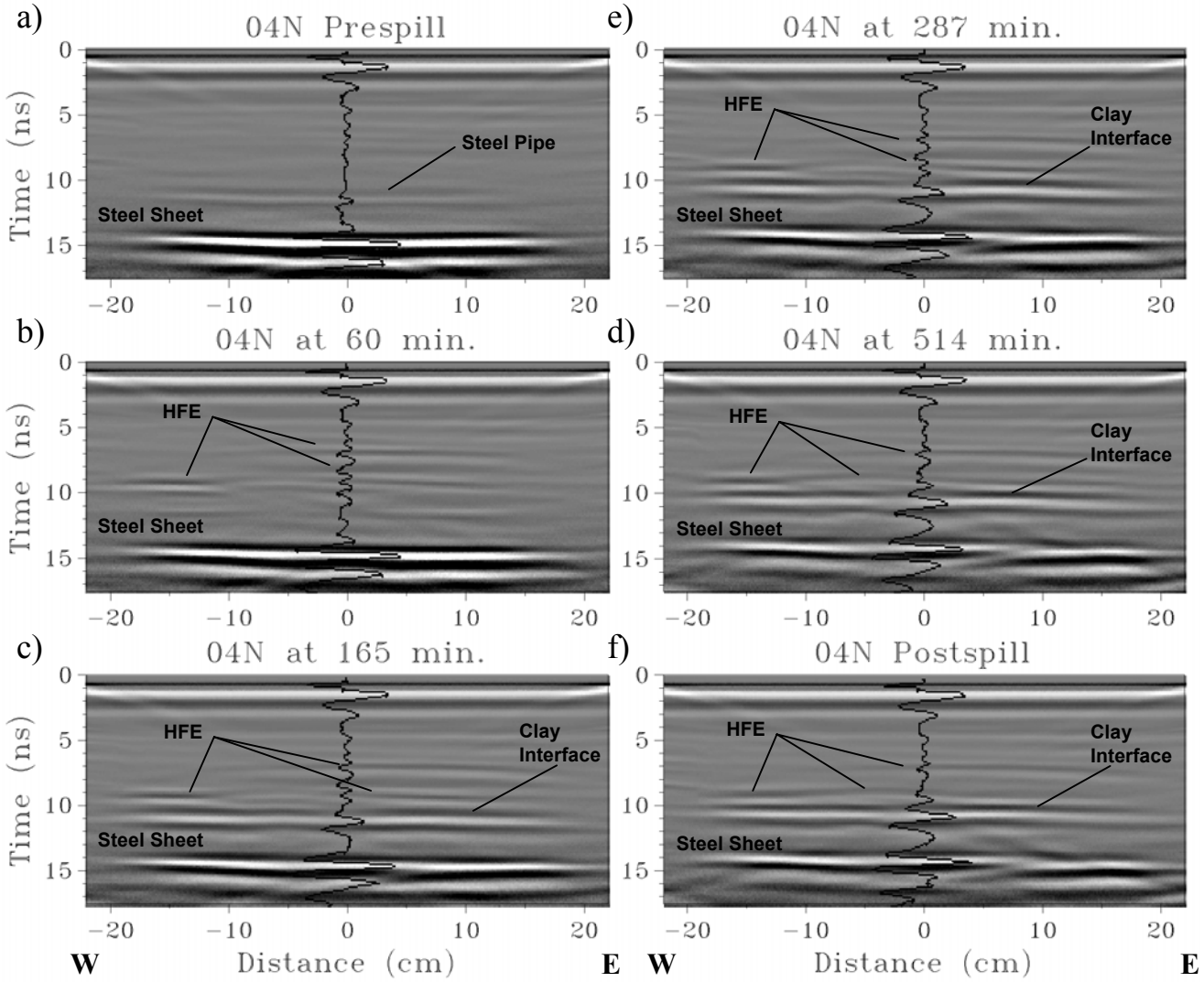

Figure 4.11: GPR data at various times along 04N, looking north.

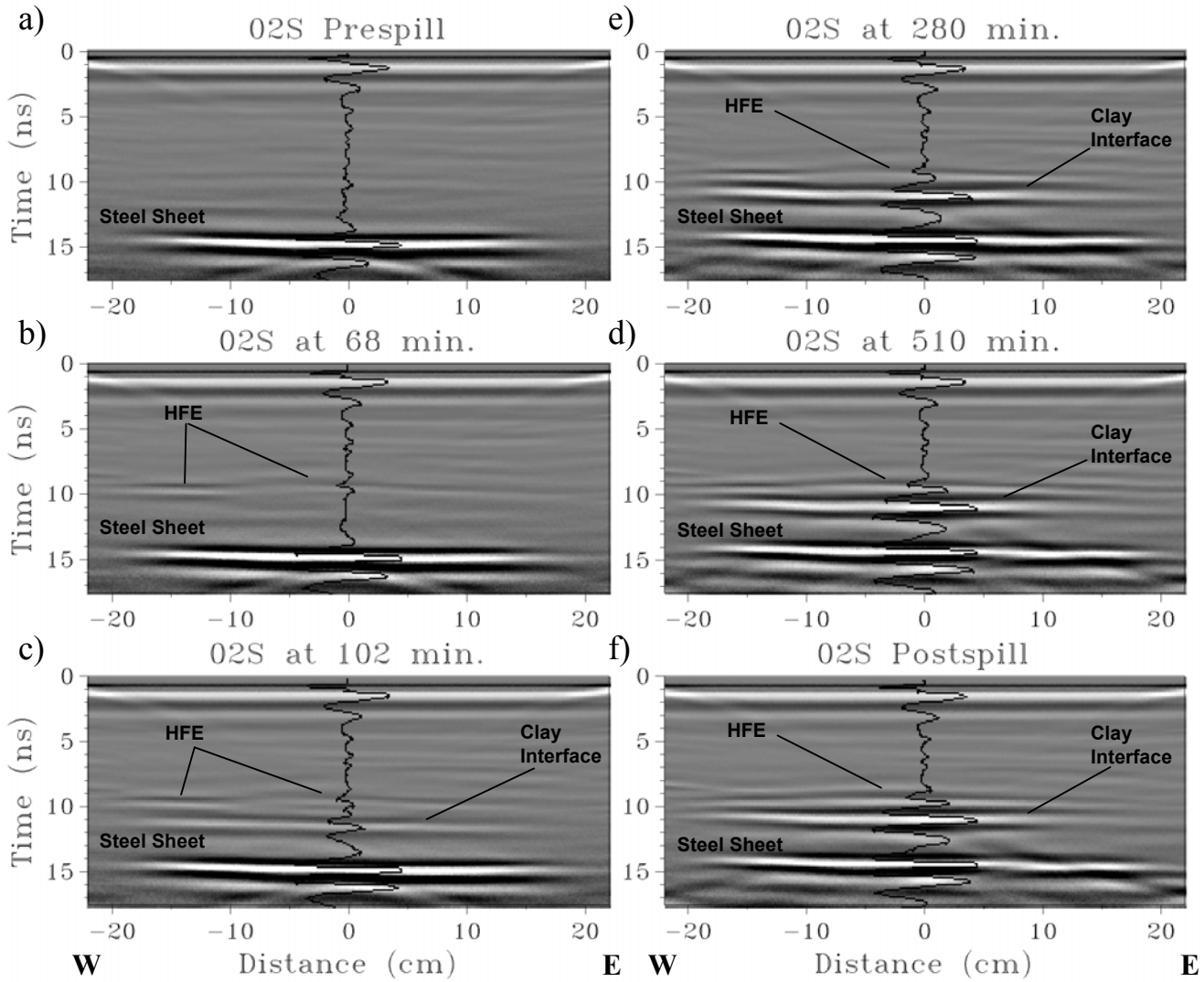

Figure 4.12: GPR data at various times along 02S, looking north.

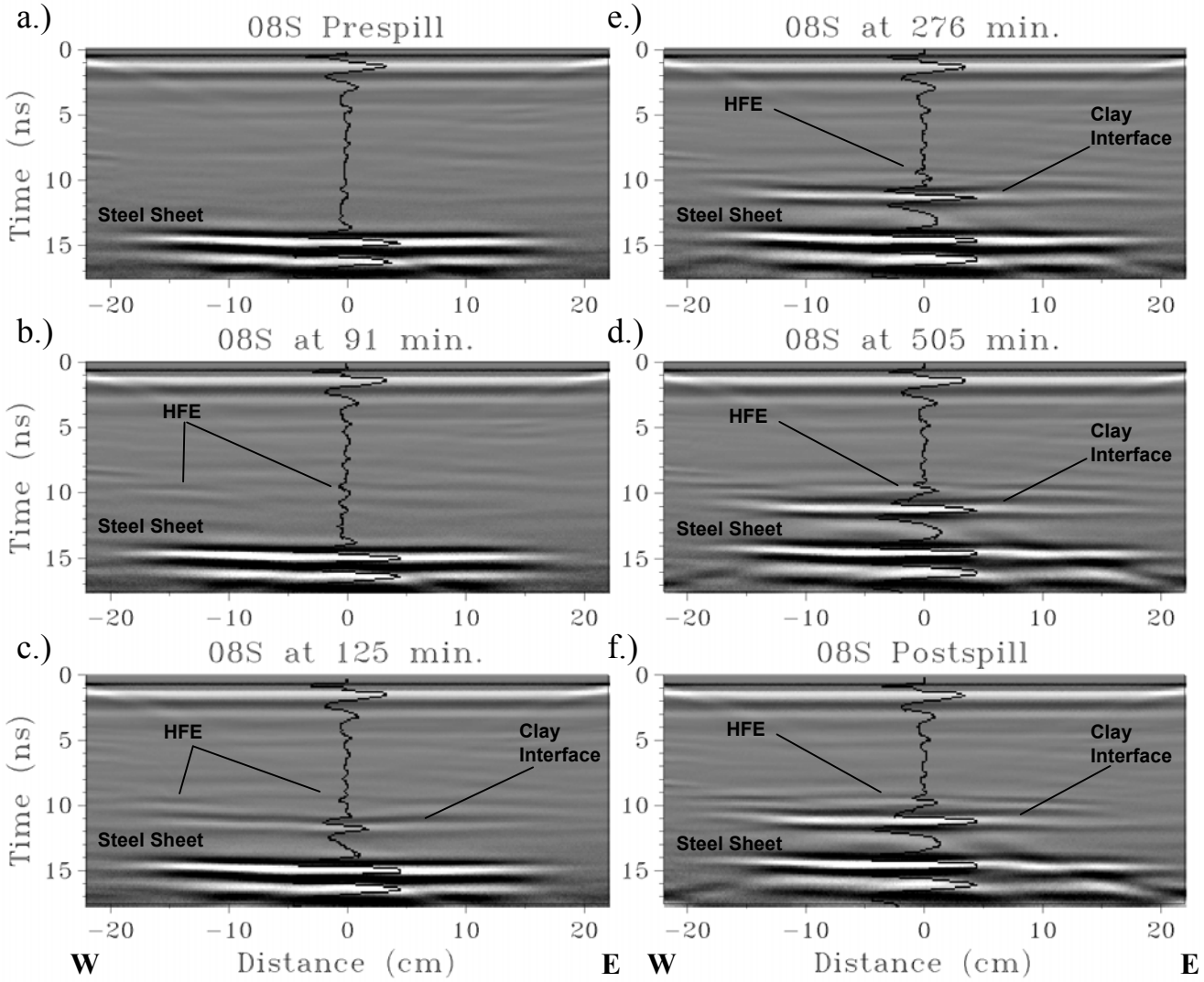

Figure 4.13: GPR data at various times along 08S, looking north.

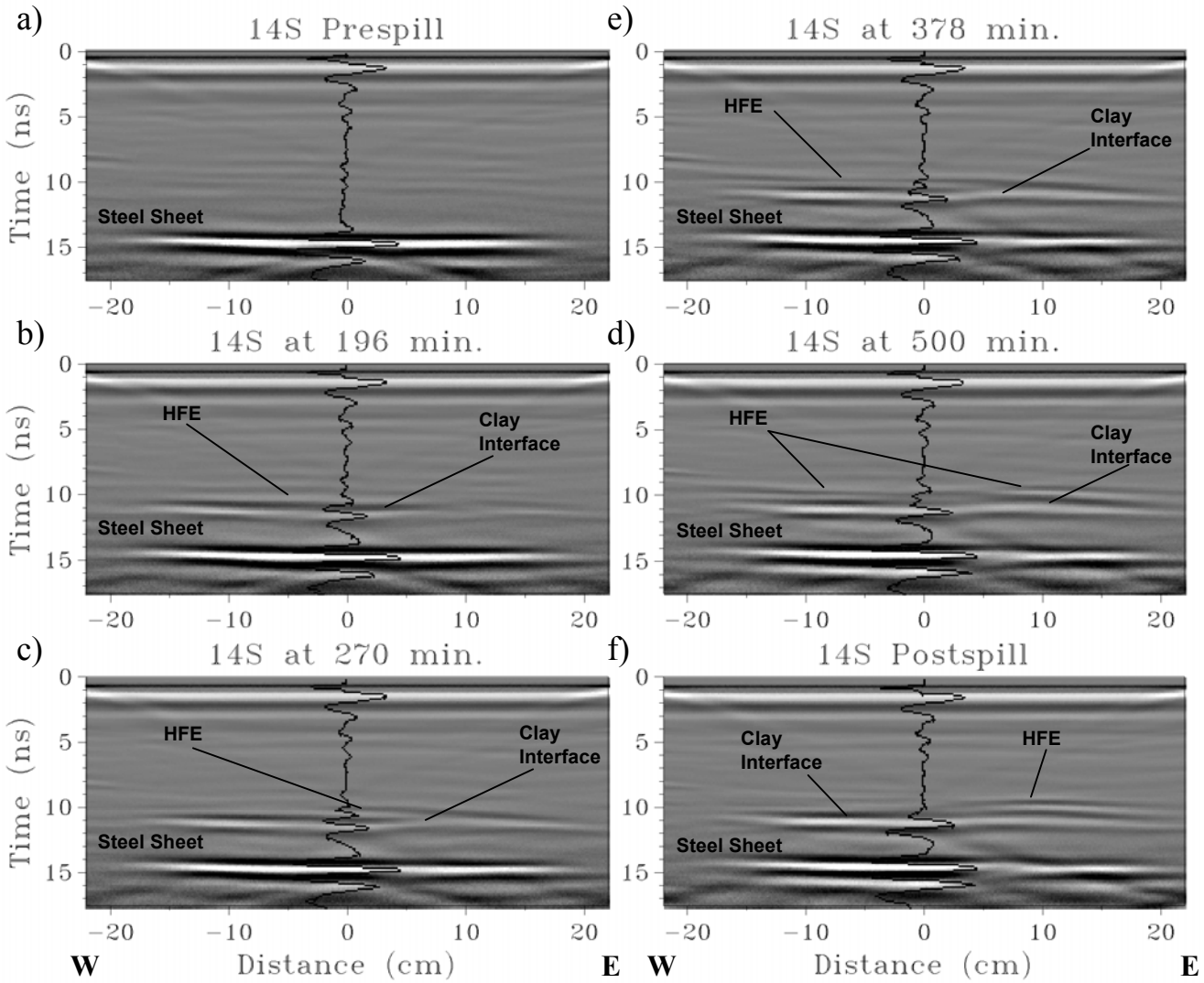

Figure 4.14: GPR data at various times along 14S, looking north.

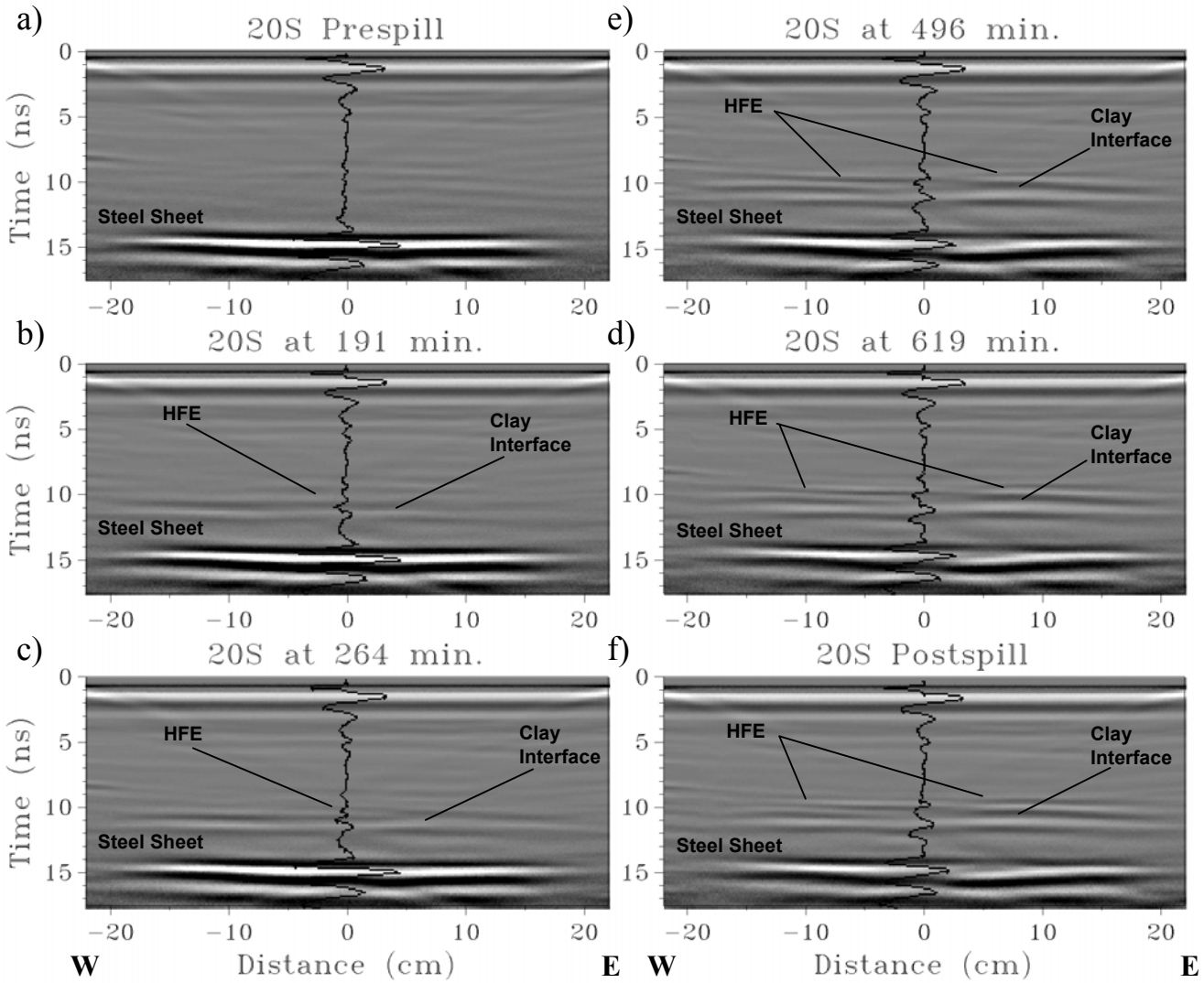

Figure 4.15: GPR data at various times along 20S, looking north.

dramatically in Figures 4.7c and 4.8c, where the reflection slopes to the south. The reflection occurs sooner on the north end due to the greater volume of HFE close to the injection zone. The GPR waves travel faster through the water/HFE/sand mixture than the water-saturated sand and the travel time decreases with increasing HFE volume; thus, the use of time for the y-axis and not depth. The arrival time of reflected GPR energy, seen as a change in gray coloration, is controlled by the two-way travel time required for the energy to leave the antenna, be reflected by the subsurface material, and travel back at the antenna.

Additional key features in the GPR images include reflections from the sand/clay interface with HFE in the sand, HFE inflow, and a steel pipe. Reflections of the GPR energy occur where there is a change in electrical conductivity and/or dielectric permittivity. Reflections from the steel sheet and steel pipe occur due to their greater electrical conductivity. The clay is slightly more electrically conductive and has a slightly different permittivity than the water-saturated sand, but as seen in the prespill images, this contrast is not great enough to produce a strong reflection. Because HFE is non-conductive and has a much lower permittivity than water, when HFE flows into the sand at the sand/clay interface, the resulting contrast highlights this interface (Figures 4.7 through 4.15). Reflections that occur within the sand that are before the reflection of the sand/clay interface indicate inflow of the HFE. At 10N and 04N (Figures 4.10 and 4.11), these reflections are seen at a spill time before the sand/clay interface is highlighted, indicating that the HFE is following the sand layering before it reaches the sand/clay interface. These reflections persist throughout the spill, indicating that the HFE thickness remains greater near the injection, which is confirmed in the postspill cores. Farther away from the source, the HFE thickness is less, and the reflection from the top of the HFE is much closer in time to the sand/clay interface (Figures 4.12 through 4.15). Because the HFE saturation becomes greater with depth due to its density and gravity-capillary equilibrium, the sand/clay interface has a much greater permittivity contrast

than the gradual or non-distinct top of the HFE. As a result, the top interface reflection is not as distinct in the GPR data.

A steel rod was placed at the sand/clay interface at 14N and can be see as a parabolic reflection in the prespill images for 10E and 11W (Figures 4.7 and 4.8). At later spill times, the reflection from the steel rod cannot be distinguished from the HFE highlighted sand/clay interface. The reflection from the steel pipe is also seen in the 10N and 04N prespill images at approximately 11 ns (Figures 4.10a and 4.11a) because of the three-dimensional nature of the reflection. GPR waves transmitted from the antenna emanate in the shape of a cone; thus, the antenna detects reflected energy that is not directly below the antenna (Lucius and Powers, 1997), creating a parabolic nature in the reflection from the steel pipe in the 2D images. The shortest reflection time, the top of the parabola, occurs where the antenna is directly over the pipe, while energy reflected from the pipe in the second and/or third dimension arrives later due to the greater travel distance of the GPR wave. This three-dimensional (3D) nature of GPR data is important for proper interpretation of 2D GPR images.

4.5 Core Data

Mass analyses of HFE saturation were completed on all of the core tubes, but error involved in measuring the exact tube volume along with the loss of HFE during the cutting process was large enough that the resulting saturation values were only qualitative. The mass analyses agreed with the visual observations of the amount and location of red color in the core tubes.

Visual and mass analysis data showed that HFE saturation increased with increasing depth in individual cores and total HFE thickness increased closer to the injection source. Distinct changes in HFE saturation between layers could be seen on occasion as an abrupt color change. The most notable of these abrupt color changes occurred in cores 10N

0EW and 0NS 5E. In 10N 0EW there was a graduated color of dark to medium red for 0-7.62 cm above the clay followed by an abrupt contact to lighter red from 7.62-13.02 cm above the clay. This contact corresponds well with the reflection seen at 10N in Figure 4.10 at a time of approximately 7 ns. In 0NS 5E, the HFE occurred in a gradually decreasing red color from 0-5.40 cm above the clay followed by an interval of no red color from 5.40-7.62 cm above the clay. This was then followed by a thin red stringer in only one side of the core from 7.62-7.94 cm above the clay. This contact corresponds well with the reflection seen at 7 ns in 04N on the east side of the tank (Figure 4.11). This same reflection was also seen in the 2D GPR image at 01N, but was not readily apparent in any traces south of 0NS.

4.6 GPR Modeling

4.6.1 Background

Ground penetrating radar data are modeled using a software package that computes the GPR response by calculating the transmitted and reflected waves as the pulse is propagated through a geologic model of flat, horizontal layers of specified thickness and associated electromagnetic properties (complex dielectric permittivity, electrical conductivity, and complex magnetic permeability). The user adjusts the geologic model to obtain a GPR response that is most similar to the field-measured response. Solutions are not unique, but may be constrained by the user based on prior knowledge of the medium and/or subsurface geometry. The one-dimensional (1D) full-waveform GPR modeling software used in this research is a module of GRORADAR™ version 8.99 (Olhoeft, 1998), which is based upon GPRMODV2 by Powers and Olhoeft (1995). One-dimensional GPR modeling was used to quantitatively determine the change in dielectric permittivity of the initially water-saturated sand as HFE flowed into the pore spaces.

Quantitative permittivity values from the 1D GPR modeling were also used in a 2D GPR modeling program (Powers, 1997). The 2D GPR modeling was used qualitatively to confirm the absence and/or presence of multidimensional influences. Powers (1995) provides detailed descriptions of the theory and formulation of both the 1D and 2D GPR modeling codes.

4.6.2 One-dimensional GPR model parameters

GPR modeling input parameters include the parameters associated with the GPR antenna, geologic geometry and associated electromagnetic properties. The character of the energy reflected from the steel sheet was used to determine the coupling ratio of the GPR antenna with the saturated sand. The coupling ratio determines the reduction in the radar wave frequency due to near-field affects around the antenna (Lucius and Powers, 1997). The GPR antenna was rated for 1.5 GHz, but the coupling ratio of 1.95 indicates an actual frequency of 769 MHz within the sand. The shape of the reflection also indicated the radar wave was in the form of a Ricker wavelet. The initial Ricker wavelet and the Ricker wavelet with a coupling ratio of 1.95 are shown in Figure 4.16. The slight leader (flat portion) on this wavelet at early times has been found to produce the best GPR modeling results (Powers, 2003). Antenna wavelet forms and their affects on GPR modeling are discussed briefly in Sneddon and others (2002). Field traces were adjusted for the firing time of the antenna, which was generally at 2.43 ns into a total measurement window of 20 ns. This time was slightly later on a few profiles (up to 2.65 ns) when the antenna was used from 1-2 hours after the equipment was turned on, indicating a longer warm up period was required.

Materials in the tank included quartz sand, pottery clay, water, dyed HFE, air, Plexiglas and steel. Water, dyed HFE, air, and quartz sand are always present as mixtures. None of these materials are magnetic, so the electromagnetic properties of

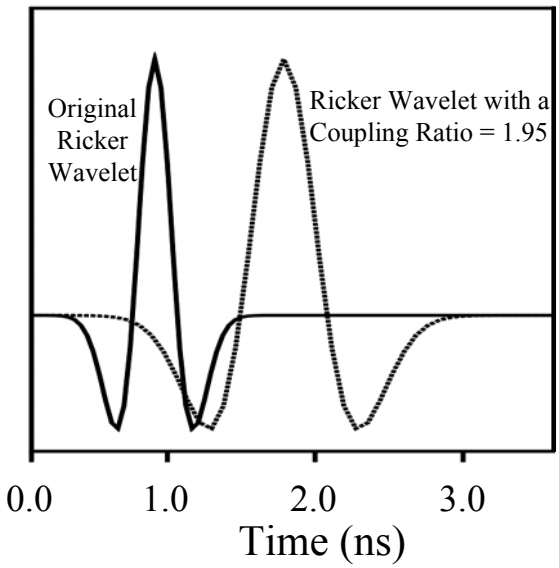

Figure 4.16: Original Ricker wavelet and Ricker wavelet with a 1.95 coupling ratio, which is used in the 1D GPR modeling

concern are complex dielectric permittivity and electrical conductivity. The prespill permittivities of Plexiglas, air/water/sand, water/sand, and clay used in all the GPR modeling were 2.5, 10.0, 23.0, and 28.0 respectively and are shown in Figures 4.17 and 4.18. The permittivity of Plexiglas was measured to be 2.74 using a parallel-plate capacitor and ASTM method D150 (ASTM,1998) at a frequency of 1 MHz. However, the measurement showed Plexiglas is somewhat frequency dependent with a decreasing value as the frequency increases. The parallel-plate capacitor could not measure permittivity at a frequency above 1 MHz , so a value of 2.5 was assumed. The permittivity of dyed HFE and distilled water were measured to be 6.85 and 80, respectively, at 1 MHz and 20º C in a liquid parallel-plate capacitor using ASTM method D150.

The porosity of the water-saturated sand was measured from cores, and ranged from 36% to 38%. The pore structure in the top of the water-saturated sand cores collapsed upon cutting as the material liquefied in response to vibration. The pore structure did not collapse in zones with high DNPAL saturation because the DNAPL was relatively immobile, and the porosity could be accurately measured. Using a permittivity of water and sand at 80 and 4.5, respectively, and the BHS curve (Sneddon and others, 2002), the calculated permittivity for a 37% porosity sand is 23. This procedure was confirmed for air/water/sand mixtures by direct measurements (Johnson and Poeter, 2003b). The porosity of the clay was measured by air drying to be 41%. Assuming a quartz sand matrix, this porosity yields a permittivity value of 25.7, but the actual permittivity of the clay particles was unknown. For the air/water/sand layer, since the permittivity of air is one, a small amount of air dramatically decreases permittivity. Using the procedure discussed in Johnson and Poeter (2003b), the permittivity of a 37% porosity sand with 50% air saturation is 9.5. In addition, total direct contact between the Plexiglas and the wet sand was not possible, allowing for a small (less than a few mm) gap of low permittivity air just below the Plexiglas. The permittivities of 10 and 28 used in the GPR modeling for the air/water/sand layer (unsaturated zone) and the clay, respectively, were

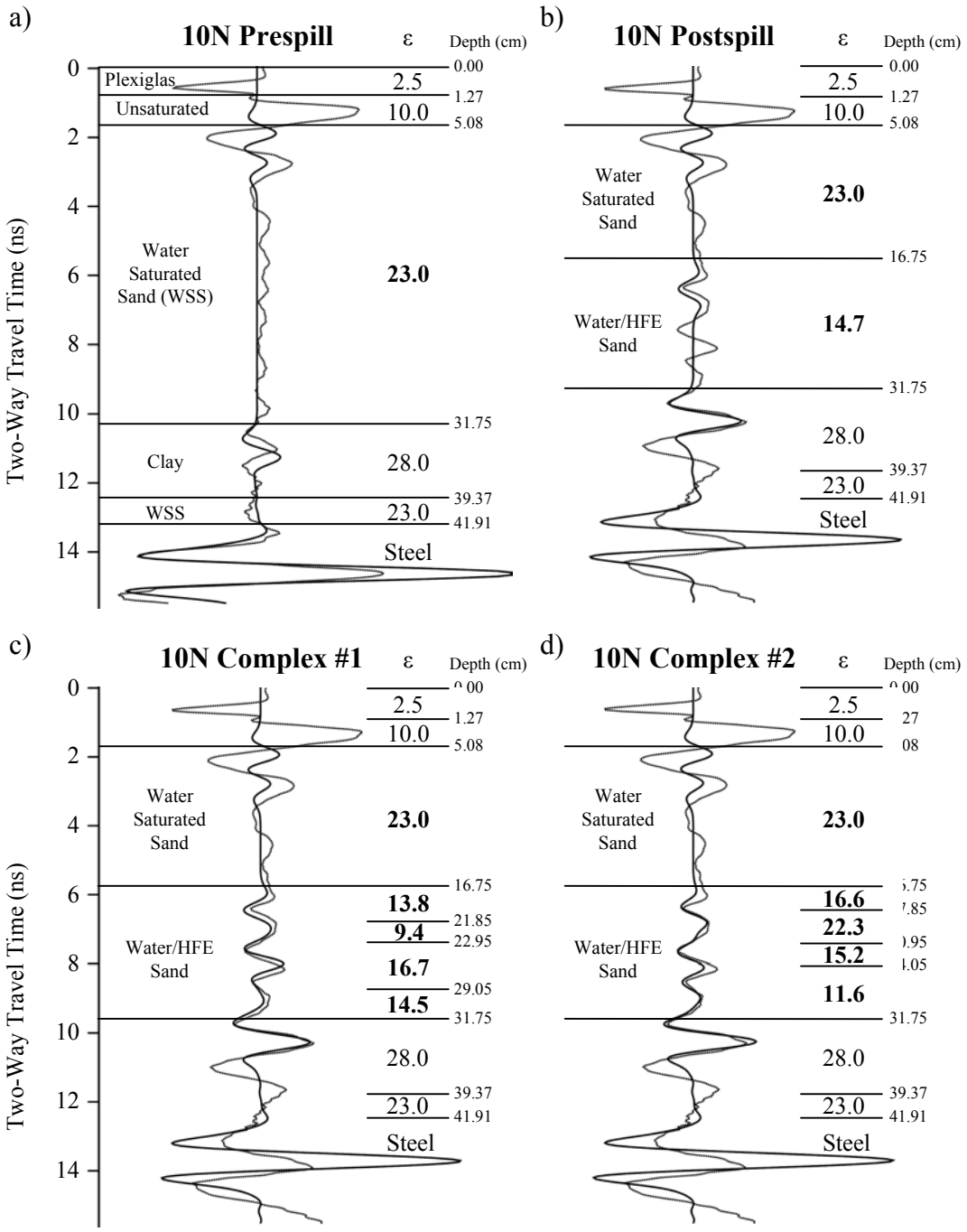

Figure 4.17: GPR traces for sand tank at 10N 0EW, dashed line is measured trace and solid line is modeled trace: a) prespill; b) postspill; c) complex match #1; and d) complex match #2.

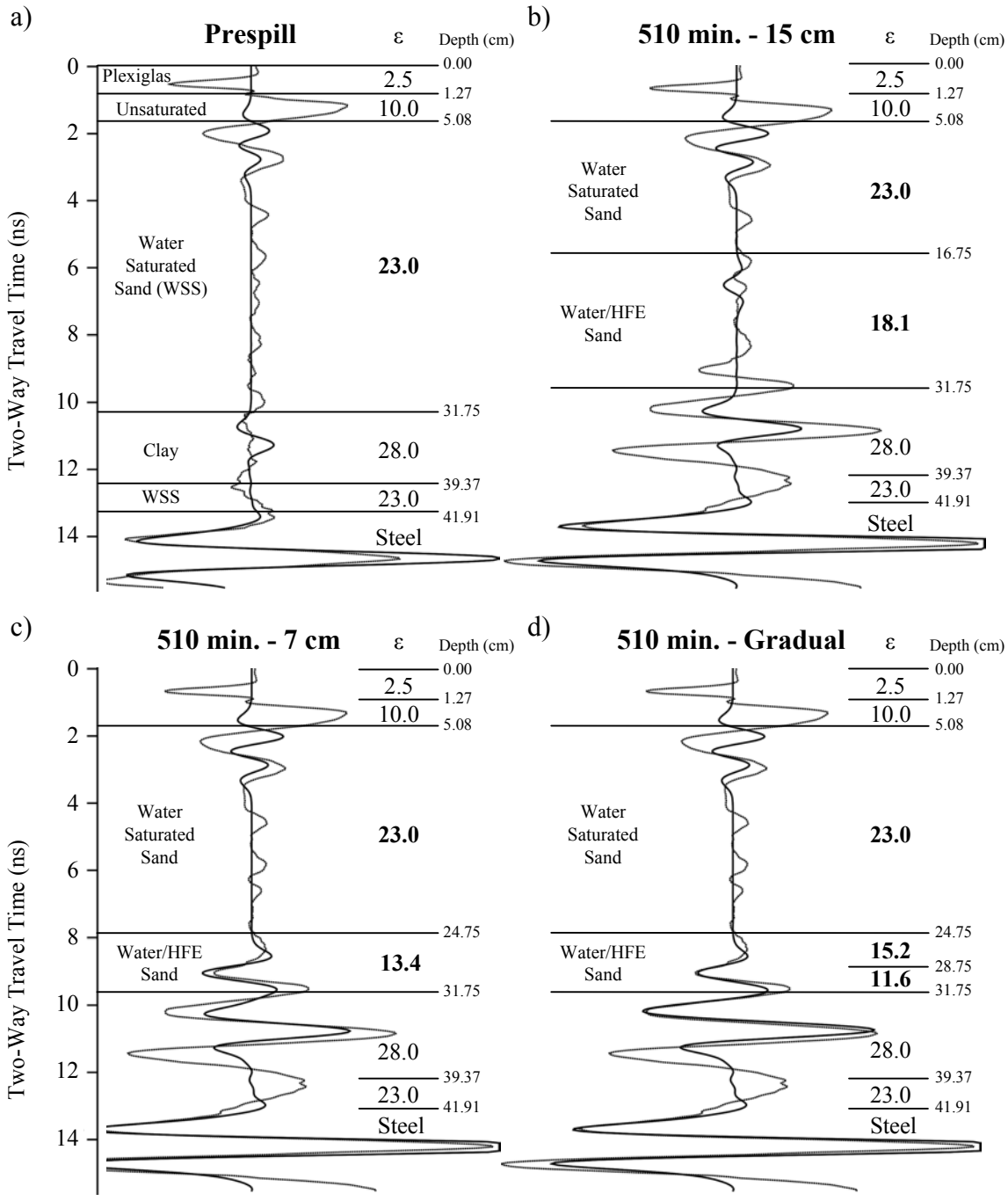

Figure 4.18: GPR traces for sand tank at 02S 0EW, dashed line is measured trace and solid line is modeled trace: a) prespill; b) 510 minutes assuming 15 cm HFE thickness; c) 510 minutes assuming 7 cm HFE thickness; and d) 510 minutes assuming increasing HFE saturation with depth.

determined via calibration. The calibration used the reasonable starting permittivity values listed above with a known thickness for the clay and a reasonable thickness for the unsaturated sand. The permittivity values were then adjusted to match the reflection of the steel sheet, which occurs at a known depth. The prespill permittivity value for the water-saturated sand was 23.0 in the center of the tank, but had to be adjusted slightly (down to 21.5) at the edges of the tank to produce a match of the 1D GPR model to the reflections from the steel sheet. This can be attributed to slight interferences in the GPR wave near the edges of the tank, rather than porosity variation.

The electrical conductivity of the water-saturated sand was measured to be 10 milliSiemens/meter (mS/m) using a hand held conductivity meter. Steel is infinitely conductive and air, dyed HFE, and Plexiglas are effectively non-conductive (0 mS/m). Using the gain function from a 1D GPR model at the center of the sand tank, a 200 mS/m electrical conductivity value for the clay provided the best match for the attenuated reflection amplitude of the steel sheet where the clay was the thickest. Since air and dyed HFE are not conductive, any sand that was not water-saturated was given a constant conductivity of 5 mS/m. Electrical conductivity values were the same in all 1D GPR models for Plexiglas, air/water/sand, water-saturated sand, water/HFE/sand, clay, and steel at 0, 5, 10, 5, 200, and 10^{10} (mS/m), respectively.

4.6.3 One-dimensional GPR modeling procedure

The initial procedure for 1D modeling of GPR data from the sand tank is similar to the procedures discussed in Sneddon and others (2002). In both cases, prespill layering within the sand is subtle because reflections of radar waves are controlled by permittivity changes due to slight variations in porosity, which is assumed to also reflect slight changes in the intrinsic permeability of the sand. Inflow of DNAPL highlights higher

permeability layers because the permittivity of DNAPL is much lower than water, creating a larger permittivity contrast between zones with and without DNAPL.

The challenge in matching a measured 1D GPR trace with a 1D GPR model is in choosing the layer thickness and permittivity. For the Borden data, Sneddon and others (2002) used a "top down" approach where the depths of layers highlighted by DNAPL were used to identify the original prespill layering. This procedure relies partially upon the amplitude of the reflection of the highlighted DNAPL because the two variables, depth and permittivity, are both unknown. The amplitude gain function for the GPR data is unknown, but Sneddon and others (2002) fixed the gain function for all of the GPR modeling for consistency. This approach was attempted for the sand tank to match the HFE highlighted layering, but the results were not unique (Figures 4.17c and 4.17d). Changes in HFE saturation, modeled as permittivity changes, were required to produce the associated reflections, but different distributions of HFE saturation produced similar results. This non-uniqueness lead to a new procedure of using a broad DNAPL zone with a bottom at the sand/clay interface and a fixed top depth at, or slightly greater than, the first highlighted horizon.

Use of one DNAPL zone relies on a matching of arrival times and fixed depths, eliminating matching to reflection amplitudes, and improving the reliability of the model results. The DNAPL saturation for the entire zone is calculated using the BHS curve (Sneddon and others, 2002) based on the permittivity relative to prespill conditions. Using the DNAPL saturation and the thickness of the zone, the volume of DNAPL in a square centimeter column can be calculated. The top of the HFE zone was held constant through time while the permittivity of the whole zone was adjusted in order to match the reflection from the sand/clay interface and the steel sheet. Since the radar wave travels faster through a HFE/water/sand mixture than a water-saturated sand, the reflections from the sand/clay interface and the steel sheet at later spill times occur at an earlier radar wave travel time, requiring a reduced permittivity for the HFE/water/sand mixture (Figures 4.17a, 4.17b, 4.18a, and 4.18b). As shown in Figure 4.18, the exact selection of

the top of the DNAPL zone is irrelevant because a thicker zone requires a higher permittivity of the DNAPL zone to create a correct match, while a thinner zone requires a lower permittivity. The different permittivities produce a consistent change in the DNAPL saturations, which produce the same total DNAPL volume, within the error of the matching procedure. The matching error refers to the range of permittivity values for the HFE/water/sand mixture, which are used to calculate the total DNAPL volume, that still produce a good GPR model fit to the steel sheet reflection. The DNAPL volume in a square centimeter column is 0.999 cm^3 for the 15 cm HFE zone in Figure 4.18b with a range of 0.955 to 1.087 cm^3 based on the matching error. For the 7 cm HFE zone in Figure 4.18c, the DNAPL volume is 1.020 cm^3 with a range of 0.994 to 1.046 cm^3. For the gradual match in Figure 4.18d, where HFE saturation increases with depth, the DNAPL volume is 1.044 cm^3 with a range of 0.994 to 1.046 cm^3. This example shows that the DNAPL volumes determined with different HFE zone representations are all within the range of the original values for a 15 cm thickness.

The HFE volumes within a square centimeter column at 200 minutes are shown in Figure 4.19 and the final postspill volumes are shown in Figure 4.20. In most of the tank, a match to the steel sheet reflection also produced a match to the sand/clay interface (Figures 4.17 and 4.18). However, in the southeast corner of the tank, the reflection from the sand/clay interface occurs at an earlier radar wave travel time when the GPR model is matched to the reflection from the steel sheet (Figure 4.21). In the southeast corner of the tank, the steel sheet reflection is distorted, possibly by reflections from the walls of the tank, so the 1D GPR model is matched to the first arrival time of the steel sheet reflection. Contoured postspill HFE volumes based on a sand/clay interface match are shown in Figure 4.22, where, based on core data, the increase in DNAPL volumes in the southeast corner is unrealistic.

The bias in the southeast corner of the tank in calculating HFE volumes from the sand/clay interface are attributed to a three-dimensional interference in the reflected radar waves. In this area, 3D radar wave reflections from the intersection of the two sloped

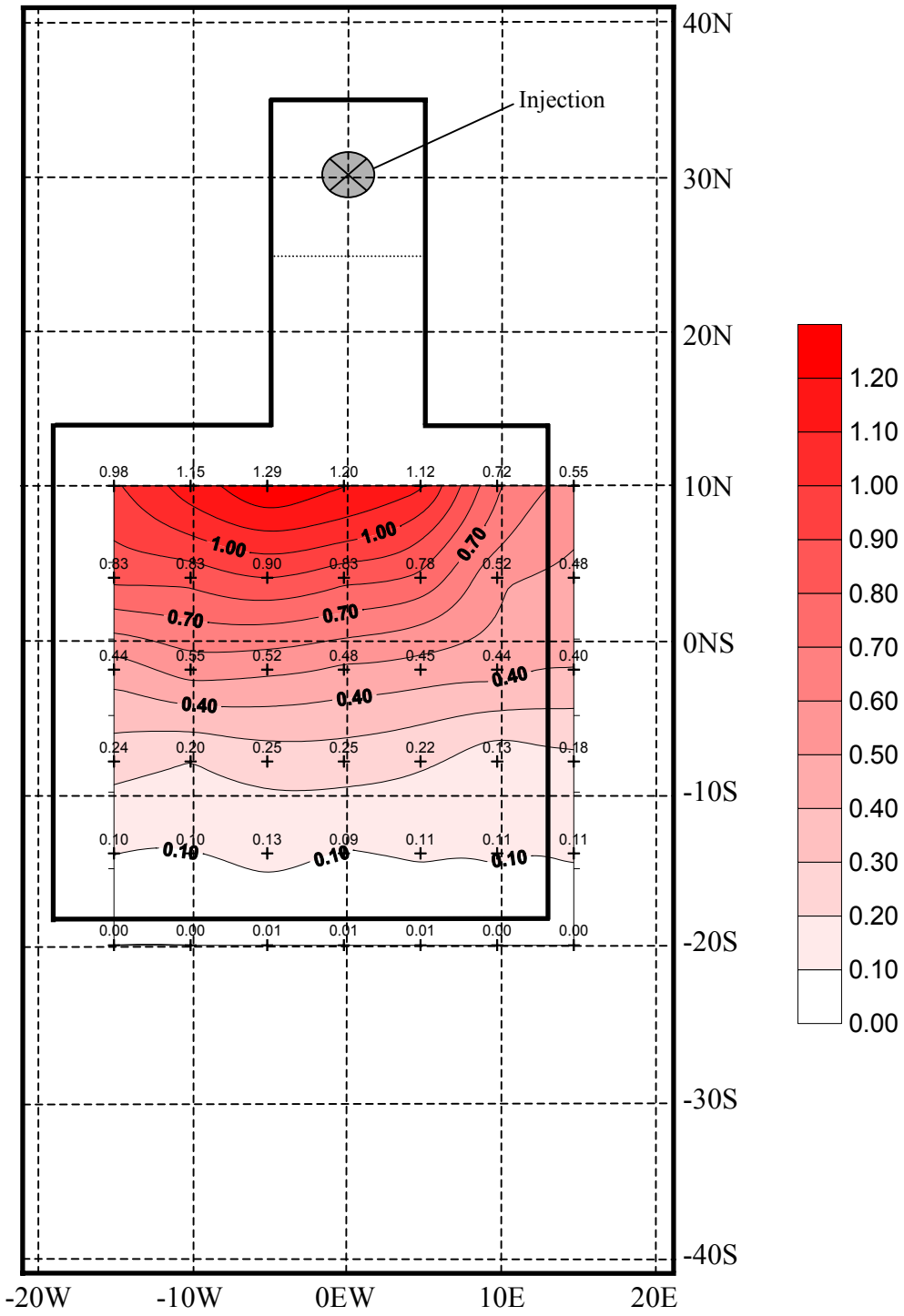

Figure 4.19: HFE volume within one square centimeter columns at 200 minutes into injection. Crosses indicate data locations. Distances are in centimeters.

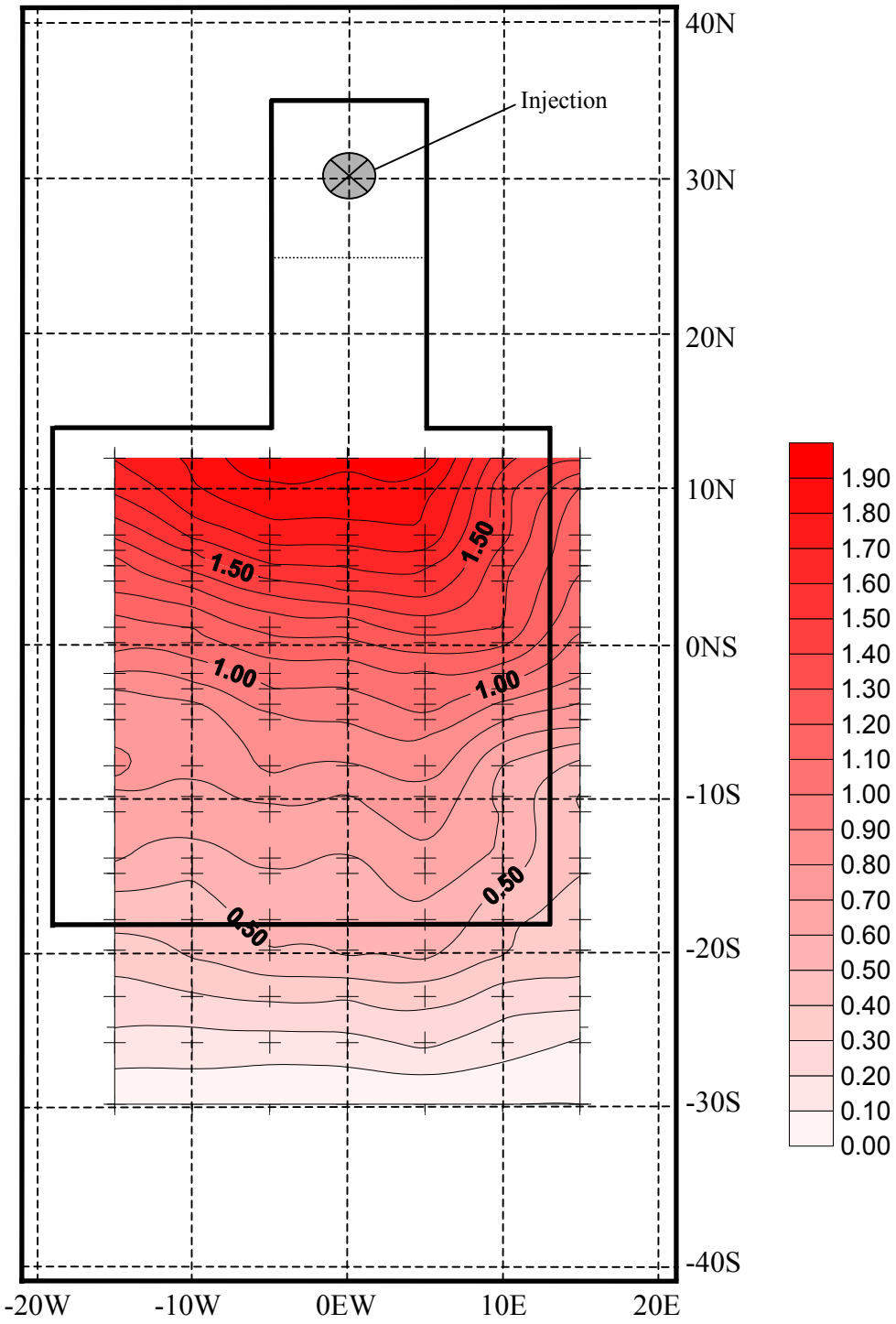

Figure 4.20: HFE volume within one square centimeter columns at postspill with a match to the steel sheet. Crosses indicate data locations. Distances are in centimeters.

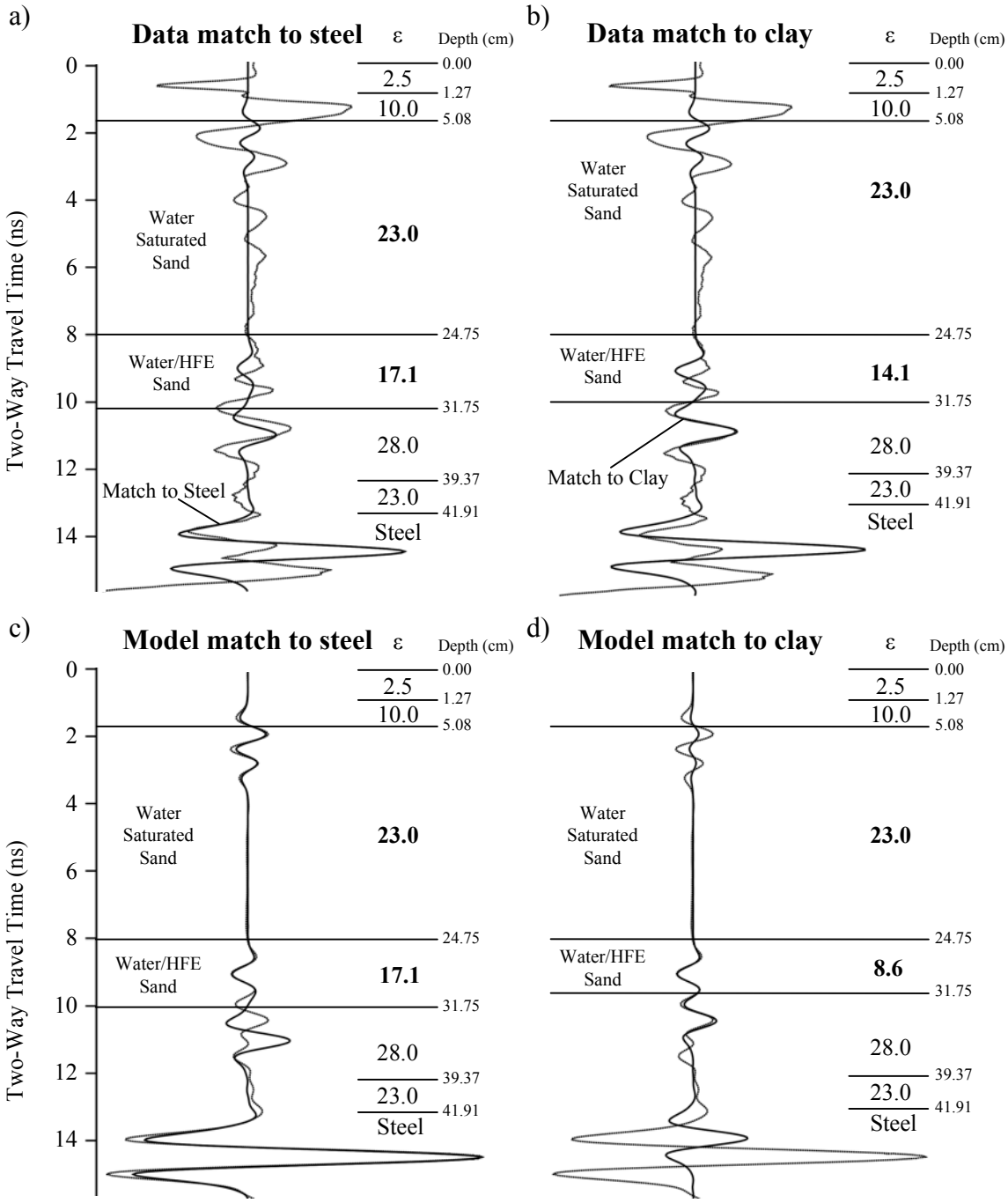

Figure 4.21: Postspill GPR traces for sand tank at 18S 5E, dashed line is measured trace in a & b and 2D model trace in c & d. Solid line is 1D model trace: a) match to steel with measured data; b) match to clay with measured data; c) match to steel with 2D model; and d) match to clay with 2D model.

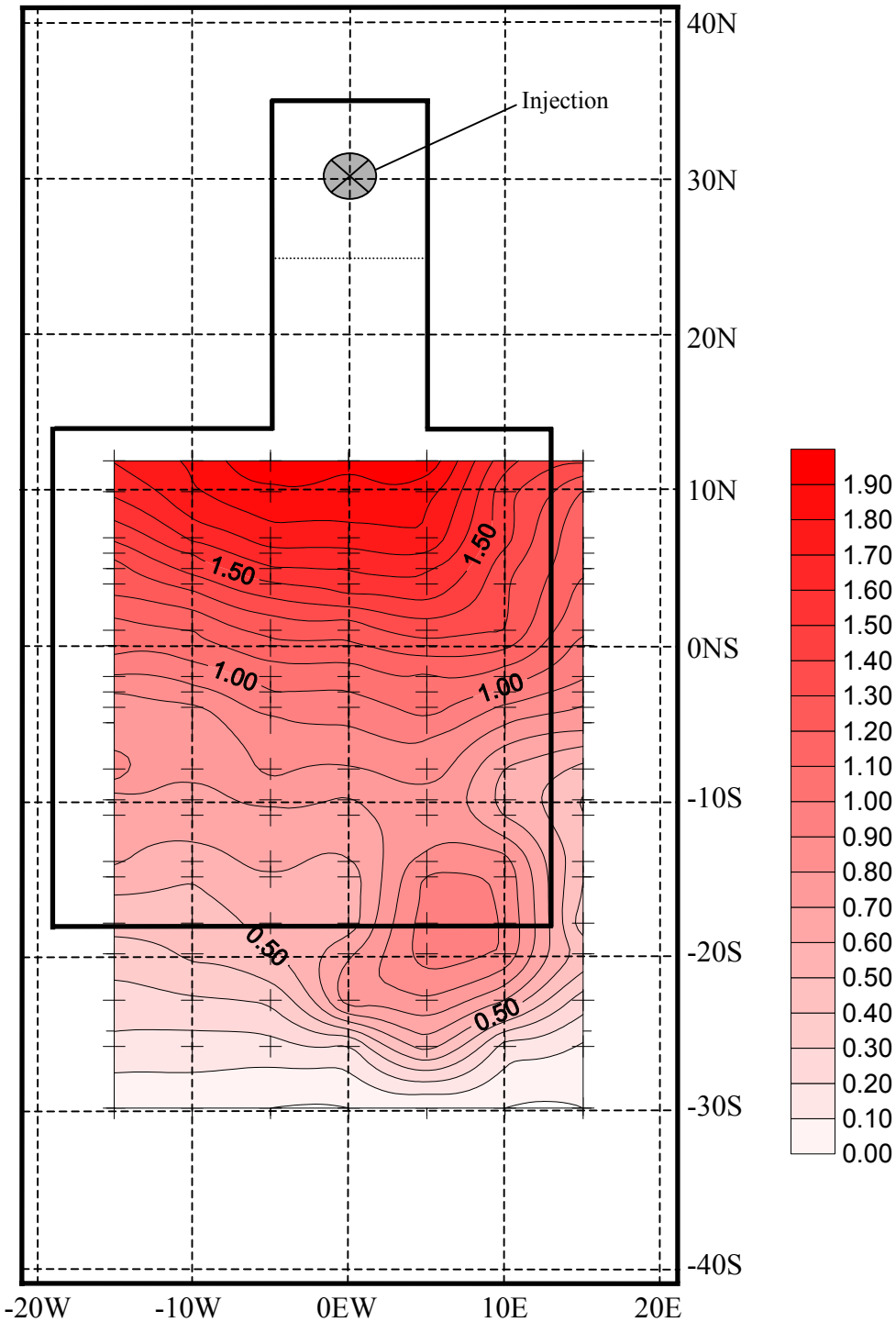

Figure 4.22: HFE volume within one square centimeter columns at postspill with a match to the sand/clay interface. Crosses indicate data locations. Distances are in centimeters.

sand/clay interfaces with HFE in the sand are amplified and then received by the antenna. This interference only occurs at locations where the time of arrival of reflections from the sloped walls interferes with the time of arrival of the sand/clay interface directly below the antenna. Using a 1D GPR model to match traces generated by a 2D GPR model with an interference reflector reproduces this incorrect match. In this case, a permittivity of 17.1 for the water/HFE/sand unit in a 2D GPR model is calibrated correctly using the steel sheet as a reference, but a permittivity of 8.6 is incorrectly determined using the sand/clay interface (Figures 4.21c and 4.21d). This bias is discussed in the 2D GPR modeling section below.

4.6.4 Two-dimensional GPR modeling of sand tank

The 2D GPR model used in this research is described in Powers (1995, 1997). While the 1D GPR model considers only reflections directly below the GPR antenna, the 2D GPR model considers specular reflections in the second dimension. Energy from the GPR antenna is transmitted in a cone shaped pattern below the antenna (Lucius and Powers, 1997); consequently, energy from reflections that are not directly below the antenna can be received.

All of the 2D GPR models use the same layering and permittivity values presented for the 1D GPR models. With the inflow of HFE, the saturated sand unit is reduced in thickness and a unit with water/HFE/sand is added. The only difference in the 2D GPR models is the representation of the actual shape of the sand/clay interface rather than representing it as a horizontal plane. At this time, the 2D GPR models cannot be as precisely compared to the actual GPR data as the 1D GPR models because the program does not allow for interactive user changes in parameters with detailed output comparisons like the 1D GPR modeling program. However, the 2D GPR model output can be compared qualitatively with measured data to evaluate whether 2D influences

must be considered. A comparison of the GPR data and the 2D GPR model at prespill, 102 minutes, and postspill for east-west trace 02S is shown in Figure 4.23 along with the geometry used in the 2D GPR model. Inflow of HFE is modeled as a 7-cm layer at 102 minutes and postspill, with a permittivity of 21 at 102 minutes and 13.4 at postspill. These permittivity values and thickness were originally determined from the 1D GPR modeling. The 2D GPR models produce a good qualitative match to the laboratory data, which shows that two-dimensional influences, such as reflections off of the angled clay walls, are not a concern within the tank. Similarly, prespill and postspill GPR data and 2D GPR models for north-south trace 10E are shown in Figures 4.24 and 4.25. In Figures 4.24 and 4.25, the steel pipe was not included in the GPR model in order to highlight the sand/clay interface. As discussed in the 1D GPR modeling section, the sand/clay interface at prespill shows a slightly greater reflection in the GPR modeling than in the laboratory data (Figures 4.23a, 4.23b, 4.24a and 4.24b). As shown by Figure 4.25, the model requires thicker HFE close to the injection to produce the pull-up in the steel sheet and the early reflection time for the top of the HFE. The 2D model simulates the attenuated signal from the steel sheet where the clay is thicker, especially in the north end of the tank (Figure 4.25). Overall, the pattern of the 2D GPR model is similar to the data, indicating that the model is representative of the sand tank. In addition, 2D influences are minimal; thus, use of 1D GPR modeling for estimation of the HFE saturation is appropriate.

The previously mentioned 3D influence of the corner of the tank was reproduced in two dimensions using an added reflector along the sloped sand/clay interface on the east side of the tank (Figure 4.26). Although this is not a 3D simulation, this reflector is positioned at a location to produce a similar response in time and space. The traces in Figure 4.26 are the 1D traces that were presented in Figures 4.21c and 4.21d to demonstrate the error associated with determining the permittivity of the water/HFE/sand unit when matching to the sand/clay interface. As shown in Figure 4.26, the permittivity used in the 2D GPR model was 17.1, which is correctly matched in the 1D GPR model in

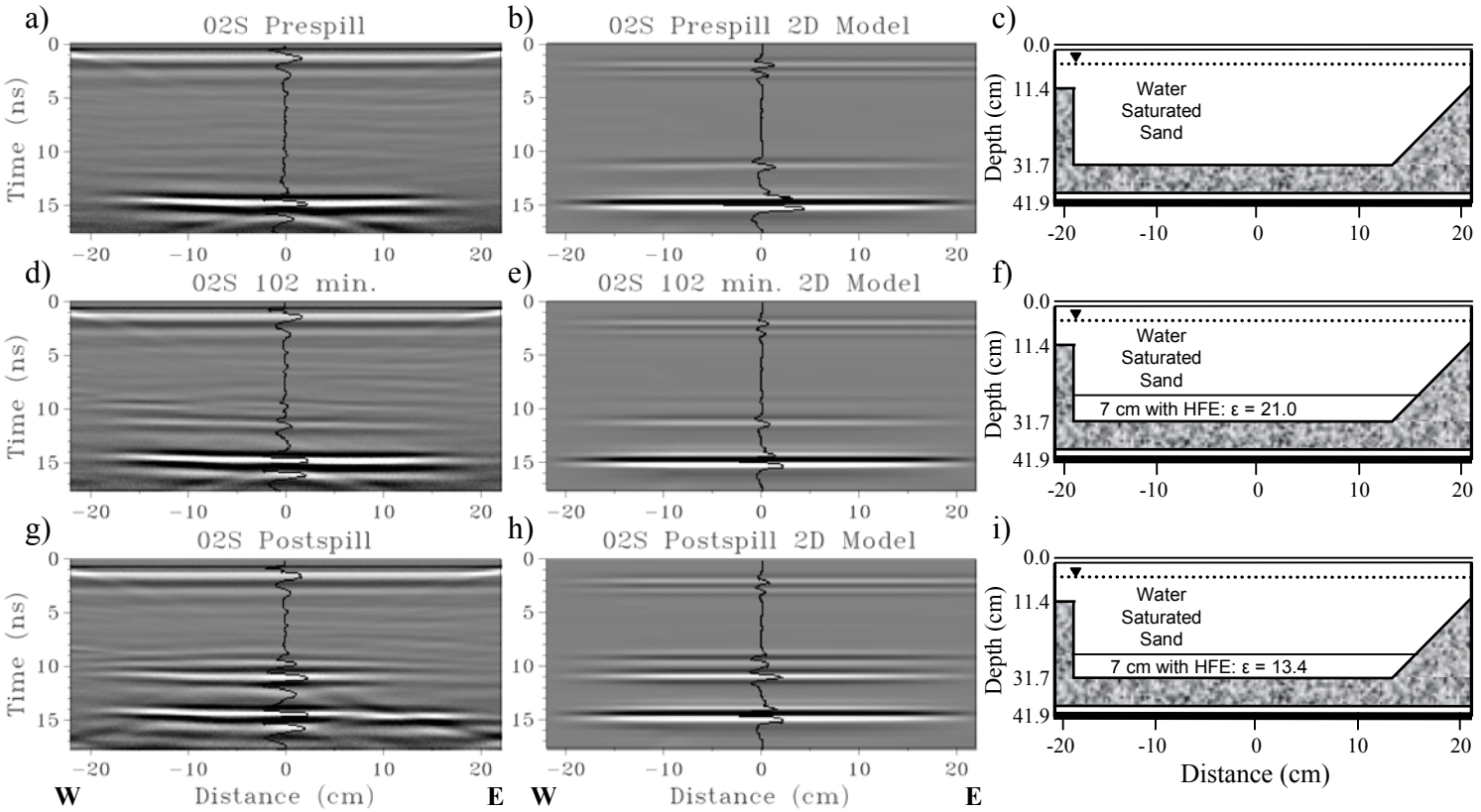

Figure 4.23: GPR images along 02S, looking north. Wiggle-trace displays are at the center of the tank: a) prespill data; b) prespill model; c) prespill geometry; d) data at 102 min.; e) model at 102 min.; f) geometry at 102 min.; g) postspill data; h) postspill model; and i) postspill geometry.

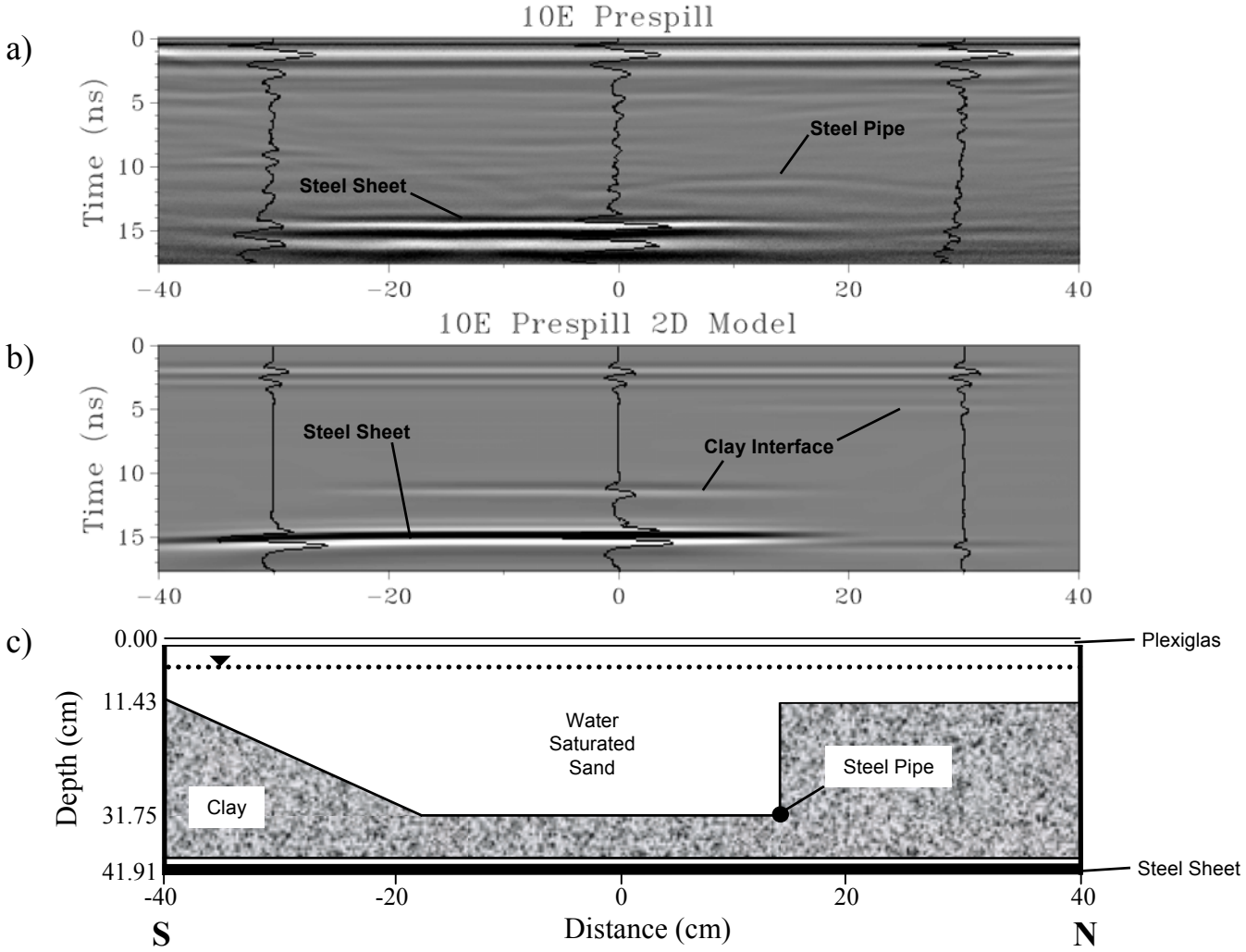

Figure 4.24: Images along 10E at prespill, looking west. Wiggle-trace displays are at –30, 0 , and 30 cm: a) GPR data; b) 2D model; and c) geometry.

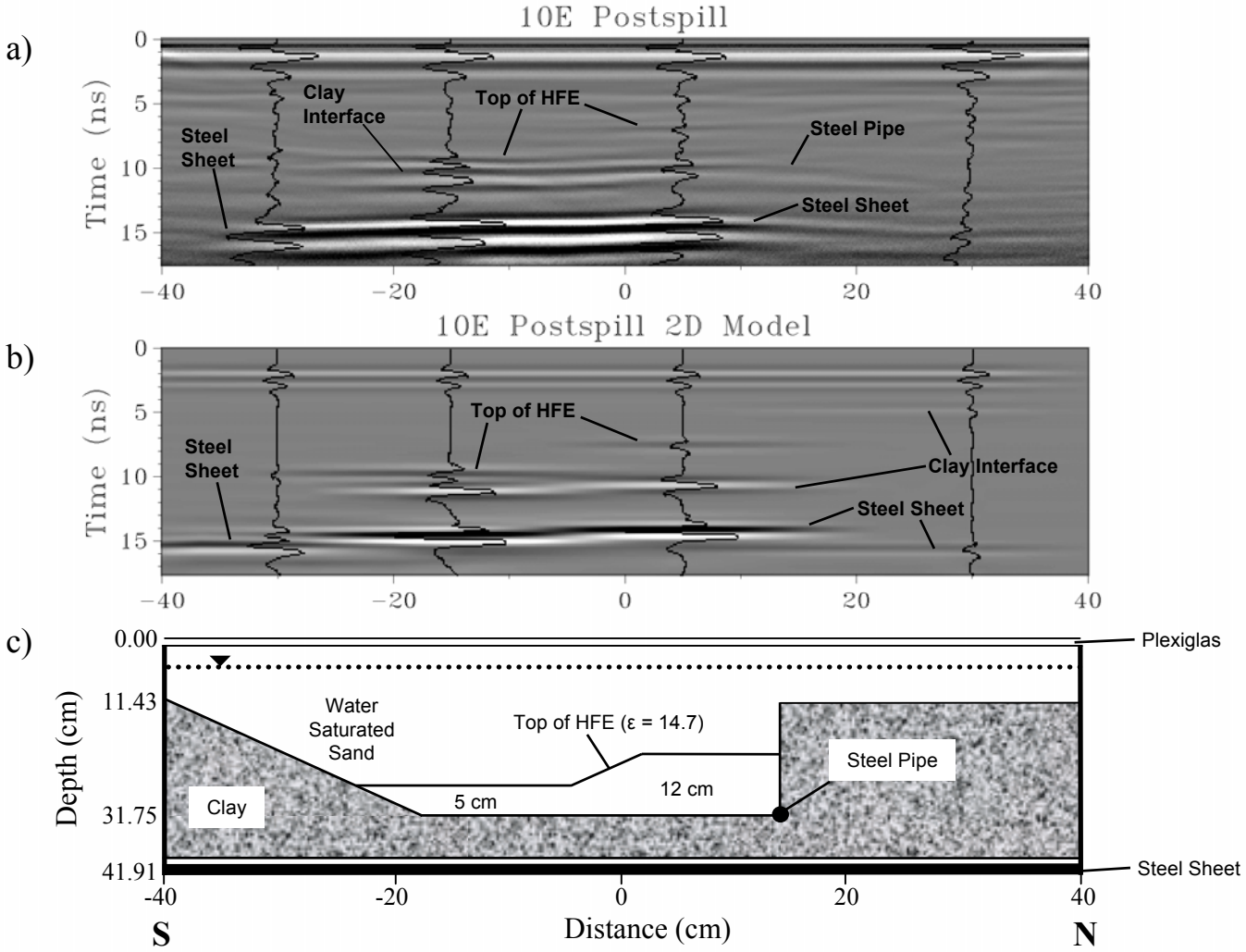

Figure 4.25: Images along 10E at postspill, looking west. Wiggle-trace displays are at –30, -15, 5, and 30 cm.: a) GPR data; b) 2D model; and c) model geometry.

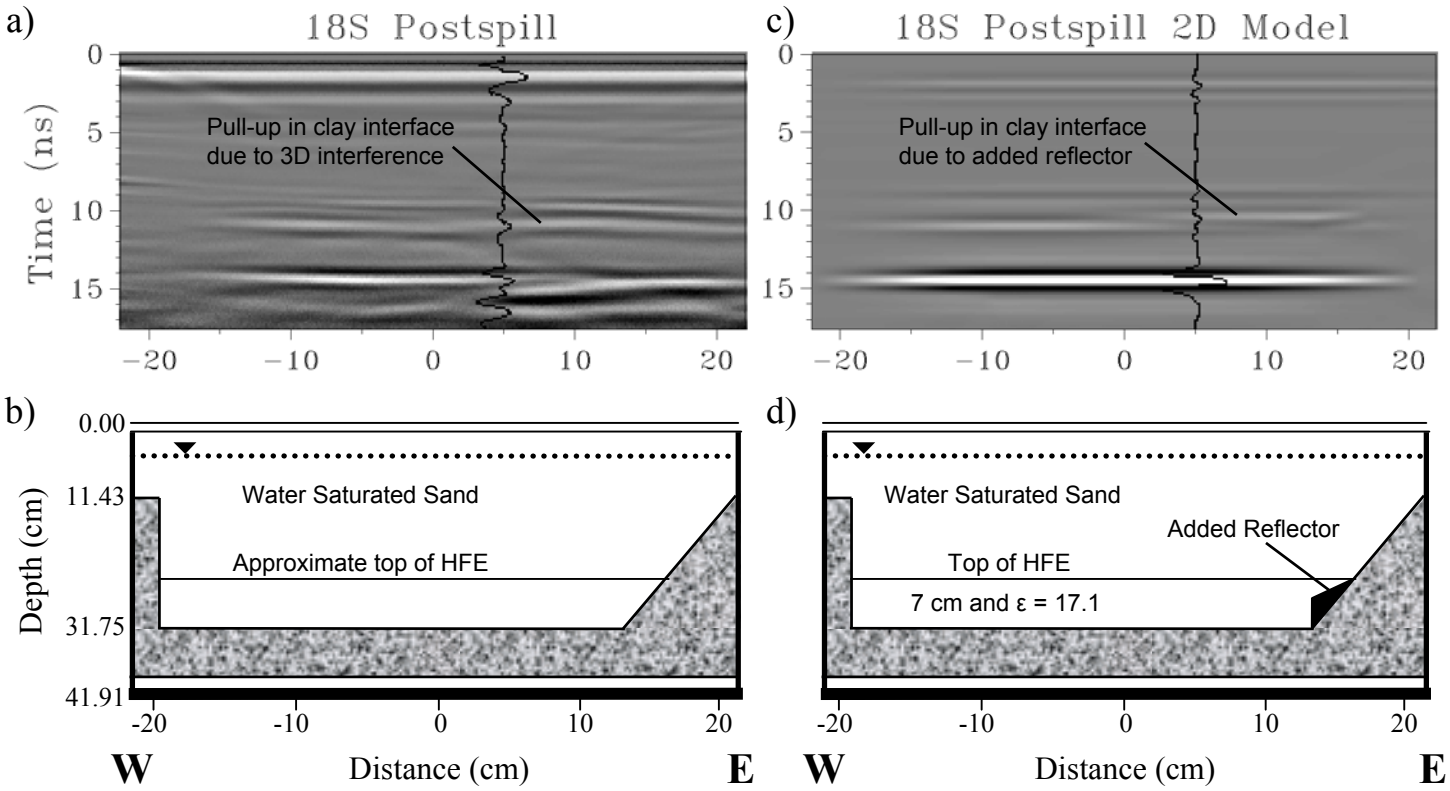

Figure 4.26: GPR images along 18S at postspill, looking north. Wiggle-trace displays are at the center of the tank: a) GPR data; b) tank geometry; c) 2D model; and d) 2D model geometry.

Figure 4.21c by matching the steel sheet reflection. In Figure 4.21d, matching the 1D GPR model to the sand/clay interface yields the incorrect permittivity of 8.6 for the water/HFE/sand unit.

4.7 Conclusions

Collection of GPR data over a DNAPL spill zone efficiently produces a detailed image of the bulk DNAPL distribution in time and space. GPR data can be used to quantitatively determine the volume of DNAPL as indicated by interpretation of GPR response to a DNAPL spill (HFE) in a small sand tank. This was achieved using the two-way travel time of radar waves reflected from a steel sheet placed below the sand tank, where increasing DNAPL volumes are indicated by decreasing travel times. The known depth to the steel sheet allows for the calibration of the permittivity of the intervening material based on the arrival time of the steel sheet reflection. Although a quantitative determination of DNAPL saturation could not be established using the core data, the qualitative, visually estimated saturation of the cores were consistent with the GPR data. One-dimensional GPR modeling of the DNAPL layers within the tank was non-unique due to an absence of depth data and a reliance upon reflection amplitudes; thus, identification of varying DNAPL saturation with depth could not be achieved.

Two- and three-dimensional influences within the tank were minimal, except in the southeast corner of the tank, where the intersection of the sloping clay walls produced an amplified reflection of the DNAPL zone, as illustrated by 2D GPR modeling. This multidimensional nature of GPR data biased the results from 1D GPR modeling because the tank walls influenced the reflection from the sand/clay interface. This bias was identified because the 1D GPR modeling that matched the steel sheet reflection showed minimal multidimensional interference, but 2D modeling confirmed a multidimensional interference, and the visual core data was consistent with the 2D modeling results. Zones

of inconsistent DNAPL saturations interpreted from 1D GPR models should be examined for possible multidimensional interferences due to geometry. This research confirms that biased DNAPL saturations calculated from 1D GPR model calibration (Sneddon and others, 2002) and used for a multiphase flow model calibration in Johnson and Poeter (2003a) are likely due to 2D interferences within a channel that are not accounted for in the 1D GPR modeling.

For a field setting where a DNAPL spill has already occurred, the identification or careful emplacement of targets (i.e., steel pipes, steel sheets, underground conduits, and geologic features) with a known depth can improve the GPR interpretation. Emplacement of targets should avoid mobilization of the DNAPL. A target placed in areas where DNAPL is not present can be used to obtain permittivity of the natural materials at the site. The DNAPL volume above a target can be calculated by calibrating a 1D GPR model to the depth of the known feature. Flat lying targets are ideal, but other target configurations could also be used if their position is known and multidimensional influences are appropriately modeled.

4.8 References

ASTM, 1998, Standard test methods for AC loss characteristics and permittivity (dielectric constant) of solid electrical insulation, 19 p.

Brewster, M. L., Annan, A. P., Greenhouse, J. P., Kueper, B. H., Olhoeft, G. R., Redman, J. D. and Sander, K. A., 1995. Observed migration of a controlled DNAPL release by geophysical methods, *Ground Water*, **33**, pp. 977-987.

Greenhouse, J., Brewster, M., Schneider, G., Redman, D., Annan, P., Olhoeft, G.,Lucius, J., Sander, K. and Mazzella, A., 1993, Geophysics and solvents: The Borden experiment, *Leading Edge*, **12**(4), pp. 261-267.

Johnson, R. H. and Poeter, E. P., 2003a, Inverse multiphase flow simulation to evaluate conceptual models, estimate intrinsic permeabilities and identify bias in field data, for a field-scale DNAPL injection in Borden sand given time-lapse GPR, in review.

Johnson, R. H. and Poeter, E. P., 2003b, Accuracy of the iterative use of the Bruggeman-Hanai-Sen mixing model to determine the proportions of a mixture of water, air and sand, in review.

Lucius, J. E. and Powers, M.H., 1997, Multi-frequency GPR surveys, *in* SAGEEP '97 Proceedings, Symposium on the Application of Geophysics to Environmental and Engineering Problems, Environmental and Engineering Geophysics Society, **1**, pp. 355-364.

Olhoeft, G. R., 1998, GRORADAR™: Acquisition, processing, modeling, and display of ground penetrating radar data: ver. 4.0, software distributed on CD-ROM at Seventh International Conference on Ground Penetrating Radar, (http://g-p-r.com).

Powers, M.H., 1995, Dispersive ground penetrating radar modeling in 2D: Ph.D. Thesis T-4820, Colorado School of Mines, Golden, CO, 198 p.

Powers, M.H., 1997, Modeling frequency-dependent GPR, *Leading Edge*, **16**(11), pp. 1657-1662.

Powers, M.H., 2003, Personal communication.

Powers, M. H. and Olhoeft, G. R., 1995, GPRMODV2: one-dimensional full waveform forward modeling of dispersive ground penetrating radar data, version 2.0: U. S. Geological Survey Open File Report 95-58, 41 p. + floppy diskette.

Sneddon, K. W., Powers, M. H., Johnson, R. H., and Poeter, E. P., 2002, Modeling GPR data to interpret porosity and DNAPL saturations for calibration of a 3-D multiphase flow simulation, U. S. Geological Survey Open File Report 02-451, 29 p.

Chapter 5

INVERSE MULTIPHASE FLOW SIMULATION TO ESTIMATE INTRINSIC PERMEABILITIES FOR A LABORATORY-SCALE DNAPL INJECTION GIVEN TIME-LAPSE GPR DATA

5.1 Abstract

A laboratory-scale DNAPL injection is monitored using ground penetrating radar (GPR). Saturation of DNAPLs, determined using the GPR data, provides calibration data for multiphase flow simulations. This paper investigates the value of GPR-derived DNAPL saturations as observations for inversion of multiphase flow simulations for the purpose of characterizing subsurface heterogeneities. The capillary pressure-saturation function and intrinsic permeability of the #45 Ottawa sand used in the experiment is measured, but the permeability varies over an order of magnitude once it is sifted into a tank. Inverse multiphase fluid flow simulations are used to estimate intrinsic permeabilities and the resulting fit statistics and analysis of residuals (observed minus simulated DNAPL saturations and observed minus simulated injection rates) are used to improve the conceptual model of permeability heterogeneities. An inverted simulation with homogeneous sand produces a permeability value that is 15% less than the measured vertical permeability. However, the fit statistics and residuals indicate an incorrect conceptual model of permeability. Additional simulations are explored using different conceptual models of permeability zones. These simulations indicate the importance of fine-scaled permeability variations and lead to an improved fit of simulated versus observed DNAPL mass distribution and injection rates. Inversion of the multiphase flow simulation is non-unique with respect to the geometry and permeability values of those zones. These fine-scaled permeability variations are imaged by the GPR data, but the

interpretation of the geometry of the zones is non-unique. Future application of GPR and inverse multiphase flow simulations to determine DNAPL flow must include a procedure to minimize this geometry non-uniqueness in order to completely identify smaller-scale permeability contrasts.

5.2 Introduction

Johnson and Poeter (2003a) present a laboratory-scale DNAPL injection, where the movement of hydrofluoroether (HFE) through water-saturated sand is successfully monitored with ground penetrating radar. These authors used GPR data to determine temporally varying HFE saturations (ratio of HFE to water in the pore space) in a specified thickness of sand throughout the tank. These HFE saturations are used to calibrate a multiphase flow simulation of the HFE injection. Calibration is automated using inverse modeling techniques, where GPR data from the injection experiment are used as observations in inverted multiphase flow simulations. The same procedure is used by Johnson and Poeter (2003b) to calibrate a multiphase flow simulation of a field-scale DNAPL injection experiment that was monitored with GPR.

Johnson and Poeter (2003b) suggest biased results in the interpretation of the DNAPL saturations from the GPR data within a channel zone and discuss the difficulties in the non-unique nature of GPR modeling. The interpretation of GPR data from the HFE injection in a sand tank (Johnson and Poeter, 2003a) confirms this bias when multidimensional influences are a factor and indicates how the bias and non-unique nature of GPR modeling can be removed using reflective interfaces with known depths. This paper investigates the value of GPR-derived DNAPL saturations as observations for inversion of multiphase flow simulations for the purpose of characterizing subsurface heterogeneities. Unlike the Borden injection, in this controlled laboratory setting, bias in the GPR interpretation is removed (Johnson and Poeter, 2003b) and the conceptual model

of larger permeability contrasts is already known. Like the Borden experiment, all of the multiphase flow parameters (i.e., fluid properties, media properties, and capillary pressure-saturation curves) are measured. Inversion results are used to evaluate the accuracy of the conceptual model of the permeability distribution and the GPR-derived DNAPL saturation data.

5.3 Measured Parameters

This experiment considers the same suite of multiphase flow parameters as the Borden injection (Johnson and Poeter, 2003a). All of the parameter values (measured and assumed) used in the multiphase flow simulations are presented in Table 5.1. The main difference in this experiment is the use of a single-sized sand with a narrow grain-size distribution (#45 Ottawa silica sand from U. S. Silica Company with a median grain size of 0.363 mm and 96.5% of the grain sizes between 0.15 mm and 0.425 mm) and a known geometry of a clay interface below the sand (Johnson and Poeter, 2003b).

Ottawa silica sand (#45) is manually sifted into a water-filled, clay-lined sand tank. Cores are taken after the injection in areas without HFE by pushing Plexiglas tubing into the sand. Falling-head permeameter tests (Klute, 1986) are performed directly on the sand within those cores (Figure 5.1). The average vertical intrinsic permeability of the sand within the tank was 3.4×10^{-11} m^2. Additional cores, with a diameter large enough to allow for horizontal sub-coring to determine the horizontal intrinsic permeability, are also taken (Figure 5.2). The average horizontal intrinsic permeability is 6.8×10^{-11} m^2. In addition, a falling-head permeameter test is completed on the entire sand tank, before HFE injection, by injecting water through the injection tube. The resulting intrinsic permeability is 3.9×10^{-11} m^2.

A capillary pressure-saturation curve of the #45 Ottawa sand with de-aired water and dyed HFE is measured using a procedure similar to that of Demond and Roberts (1991),

Table 5.1: Multiphase flow parameters for the laboratory-scale DNAPL injection experiment (all measured values are at room temperature, approximately 20-22º C).

Property	**Value**	**Source**
sand grain density	2650 kg/m^3	measured
density of water	1000 kg/m^3	
density of dyed HFE	1490 kg/m^3	measured
viscosity of water	0.001 Pa-s	
viscosity of dyed HFE	0.0007 Pa-s	measured
interfacial tension between water and dyed HFE	0.090 N/m	measured
average porosity	0.375	measured
residual wetting phase saturation	0.07	assumed value based on Kueper and Frind (1991b) and measured capillary pressure-saturation curve
exponent in Leverett function (β)	0.65	fit with data to Kueper and Frind (1991b)
van Genuchten scaling factor (α)	0.0858	measured curve fit
van Genuchten shape factor (n)	6.21	measured curve fit

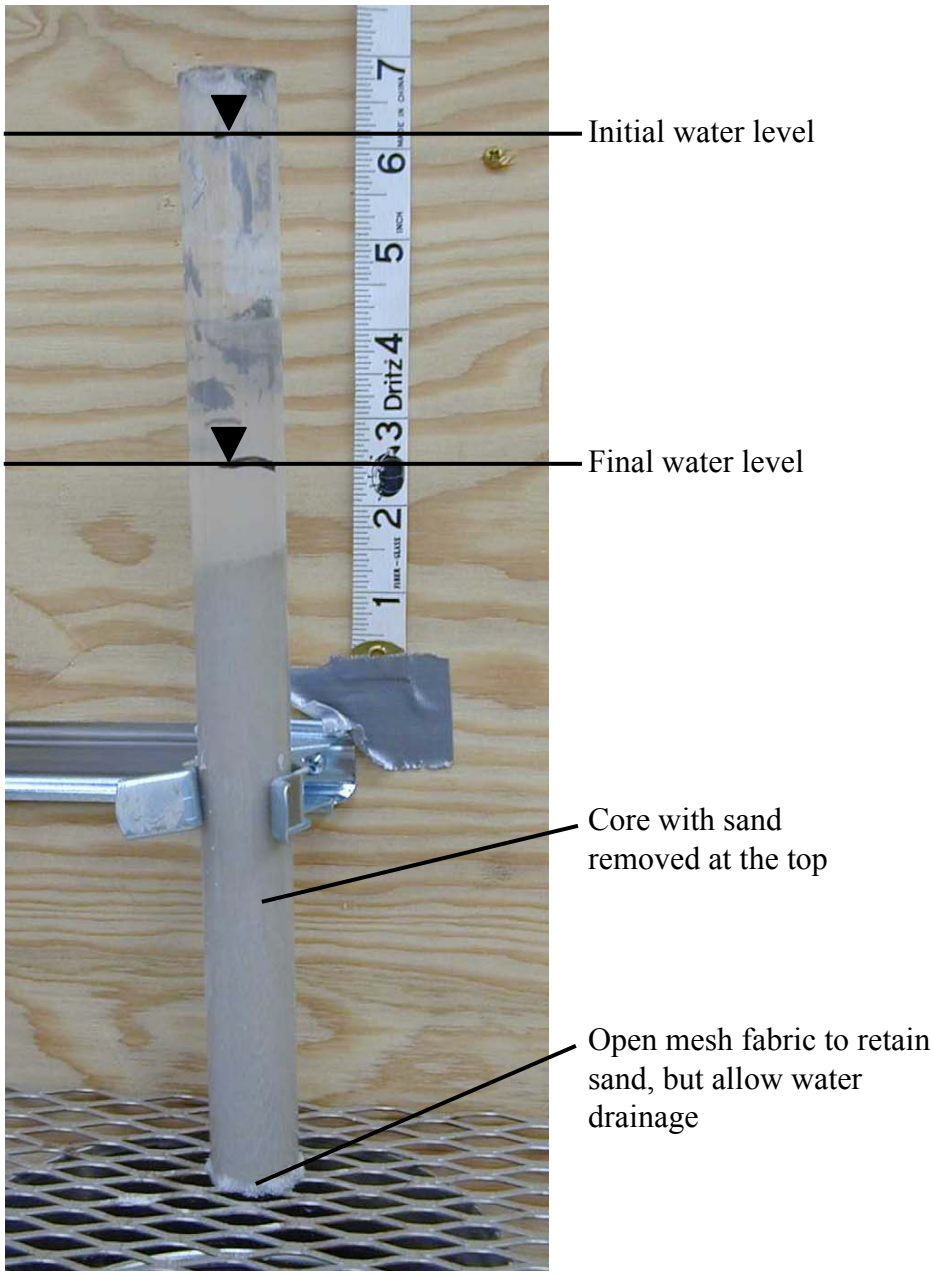

Figure 5.1: Example of falling head permeameter test.

Figure 5.2: View of horizontal coring method

where the pressure difference across the sample is created by lowering the water-filled outlet tube (Figure 5.3). Demond and Roberts (1991) use compressed air to create the pressure difference across the sample. A one-bar ceramic pressure plate is sealed into the Plexiglas tube to create a capillary pressure barrier. The bottom of the apparatus is sealed to allow for a continuous column of water below the ceramic plate. The water and HFE reservoirs are covered to minimize volatile losses. Sand is emplaced by filling the apparatus with de-aired water and sifting sand through the water to mimic the sand emplacement within the experimental tank. The sand column is 1.45 cm. The sample volume and sand mass are controlled to achieve a porosity of approximately 37.5% to match that of the sand tank. Before the HFE is added, excess water is drained to the top of the sand. For each capillary pressure-saturation measurement, the water outlet tube is lowered and the pressure is allowed to equilibrate. Capillary pressure is recorded as the difference in water pressure from the center of the sample to the water level in the outlet tube, minus the pressure from the height of HFE. The HFE saturation in the sand is determined from the increase in water volume within the outlet tube.

A non-linear least squares fitting routine (van Genuchten, 1987) applied to the experimental data yields the van Genuchten (van Genuchten, 1980) and Brooks-Corey (Brooks and Corey, 1966) parameters illustrated in Figure 5.4 for #45 Ottawa sand, as packed in this column. The van Genuchten capillary pressure-saturation relationship is:

$$P_C = \frac{1}{\alpha}(S_e^{-1/m} - 1)^{1/n} \tag{5.1}$$

The Brooks-Corey capillary pressure-saturation relationship is:

$$P_C = P_D(S_e)^{-1/\lambda} \tag{5.2}$$

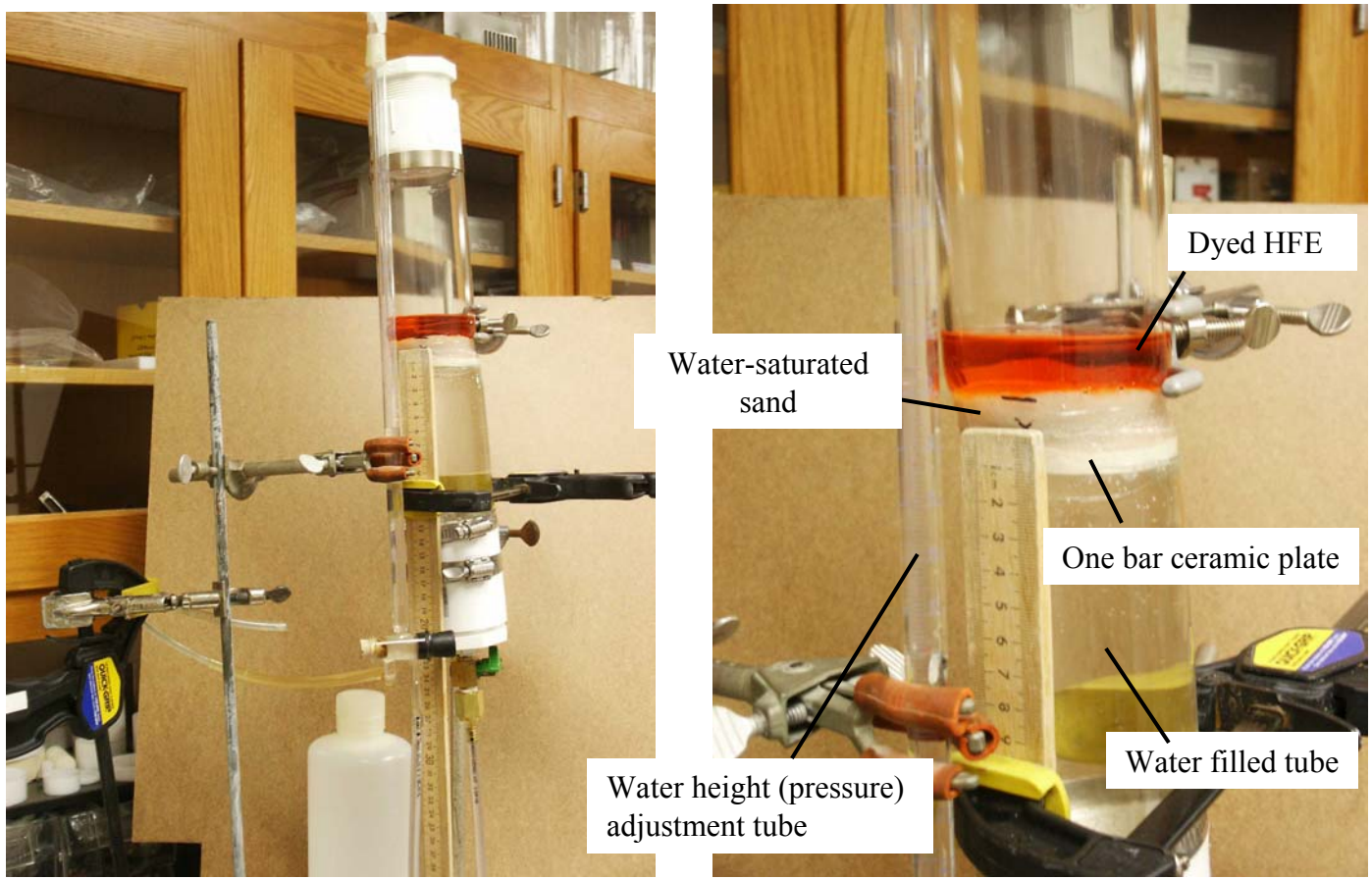

Figure 5.3: Capillary pressure-saturation measurement device: a) full-sized view of apparatus; and b) close-up view of apparatus.

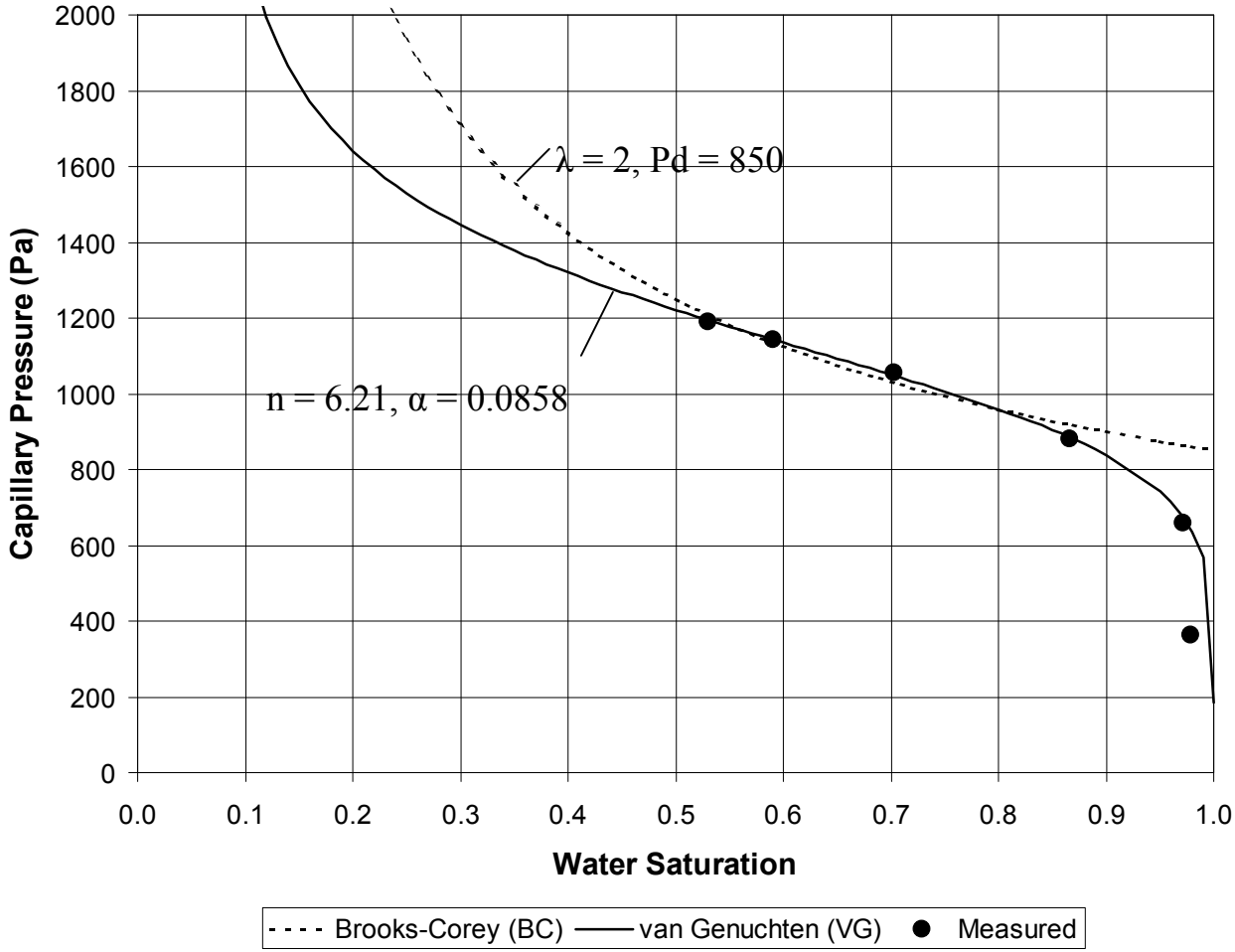

Figure 5.4: Measured capillary pressure-saturation data with curve fits to the Brooks-Corey and van Genuchten relationships.

where:
$$S_e = \frac{S - S_r}{1 - S_r} \tag{5.3}$$

and P_C = capillary pressure, α = fitting parameter related to the median pore size in the same units as the capillary pressure, S_e = effective saturation, m = 1-1/n, n = fitting parameter related to the pore distribution, P_D = initial capillary displacement pressure, λ = fitting parameter related to the pore size distribution, and S_r = residual wetting phase saturation.

The interfacial tension (σ) of dyed HFE and the de-aired water used in the tank is 90 dynes/cm or 0.090 N/m, as measured with a du Nouy interfacial tensiometer using the procedure described by du Nouy (1926) and more recently described by Paul and de Chazal (1967).

5.4 Scaling of the Capillary Pressure-Saturation Curve

The capillary pressure-saturation curve varies with the permeability of a material and is often scaled using the Leverett function (Leverett, 1941) to determine curve parameters suitable for a range of sand permeabilities:

$$P_{CD} = \frac{P_C}{\sigma}\left(\frac{k}{\Phi}\right)^{0.5} \tag{5.4}$$

where: P_{CD} = the dimensionless capillary pressure, σ = the interfacial tension between the two fluids, k = the intrinsic permeability, and Φ = the media porosity. Kueper and Frind (1991a) show this procedure to be relatively effective for Borden sand, but determine that an exponent of 0.65 created a better match than 0.5.

Visual inspection of the cores indicates gradational fining upward layers where the approximate thickness ratio of higher permeability (larger grain-size) to lower permeability (smaller grain-size) ranges from 2:1 to 10:1. Using this range of layer-thickness ratios and the measured vertical and horizontal permeabilities, values for the lower and higher permeability layers can be calculated. The results yield a low permeability of 1.5×10^{-11} m^2 and a high permeability of 9.5×10^{-11} m^2 to for the 2:1 thickness ratio and a low permeability of 0.50×10^{-11} m^2 and a high permeability of 7.5×10^{-11} m^2 to for the 10:1 thickness ratio. Sand samples measured by Kueper and Frind (1991a) from the Borden aquifer are mixed to eliminate layering before the capillary pressure-saturation curves are measured. The intrinsic permeability of those samples range from 0.44×10^{-11} m^2 to 1.2×10^{-11} m^2. The Leverett scaling method provides a means to calculate the appropriate capillary pressure-saturation parameters for additional samples where the intrinsic permeability is known, but the capillary pressure-saturation parameters are not measured.

When the capillary pressure-saturation curve is measured, dyed HFE can be seen surrounding the sand sample along the side walls of the apparatus before HFE entered the sand sample at the measured pressures. Because of this short-circuiting, the HFE is immediately available to enter the most permeable layers. Thus, the measured capillary pressure-saturation curve most likely represents the properties related to the most permeable portion of the sand sample, where 6.8×10^{-11} m^2 (the measured horizontal intrinsic permeability from core samples) is a minimum value of intrinsic permeability represented by the capillary pressure-saturation curve. Coarser sand layers may have higher intrinsic permeabilities. The concern in this case is what intrinsic permeability value is being represented by the measured capillary pressure-saturation parameters.

The measured capillary pressure-saturation curve is scaled using the Leverett function with the measured porosity and interfacial tension value using both an intrinsic permeability of 6.8×10^{-11} m^2 and 10×10^{-11} m^2 (an approximate maximum permeability based on the measured permeabilities and the observed layering thicknesses). These

curves are compared to the results from Kueper and Frind (1991a) in Figure 5.5, which indicates an intrinsic permeability of 10 x 10^{-11} m^2 is more appropriate. This is reasonable given that the Borden and Ottawa sands are similar in composition and grain size.

For multiphase flow simulations, the median pore-size fitting-parameter must be scaled appropriately for materials of different permeability using the Leverett function (only the van Genuchten relationship is considered in this case). This scaling assumes that higher permeability materials are composed of larger grains and thus, larger pores. The pore-size distribution parameter, or the variation of pore sizes from the median pore size, is assumed to remain the same. For two materials with the same porosity and the same interfacial tension, in the Leverett function (Equation 5.4) the P_{CD} will be the same for both materials, so the measured capillary pressure (Pc) depends only on the intrinsic permeability. This gives the following:

$$P_{Cref}(k_{ref})^{\beta} = P_{Cnew}(k_{new})^{\beta} \tag{5.5}$$

where: β is the exponent in the Leverett function, P_{Cref} and P_{Cnew} are the capillary pressures for the reference and the new materials, respectively, and the k_{ref} and k_{new} are the intrinsic permeabilities for the reference and new materials, respectively. Combining Equations 5.1 and 5.5 for specified effective saturation, a new van Genuchten pore size parameter (α) is determined using:

$$\alpha_{new} = \alpha_{ref}\left(\frac{k_{ref}}{k_{new}}\right)^{-\beta} \tag{5.6}$$

where α_{ref} and α_{new} are the pore size fitting parameter for the reference and new materials, respectively. The capillary pressure-saturation curve comparisons (Figure 5.5) indicate a

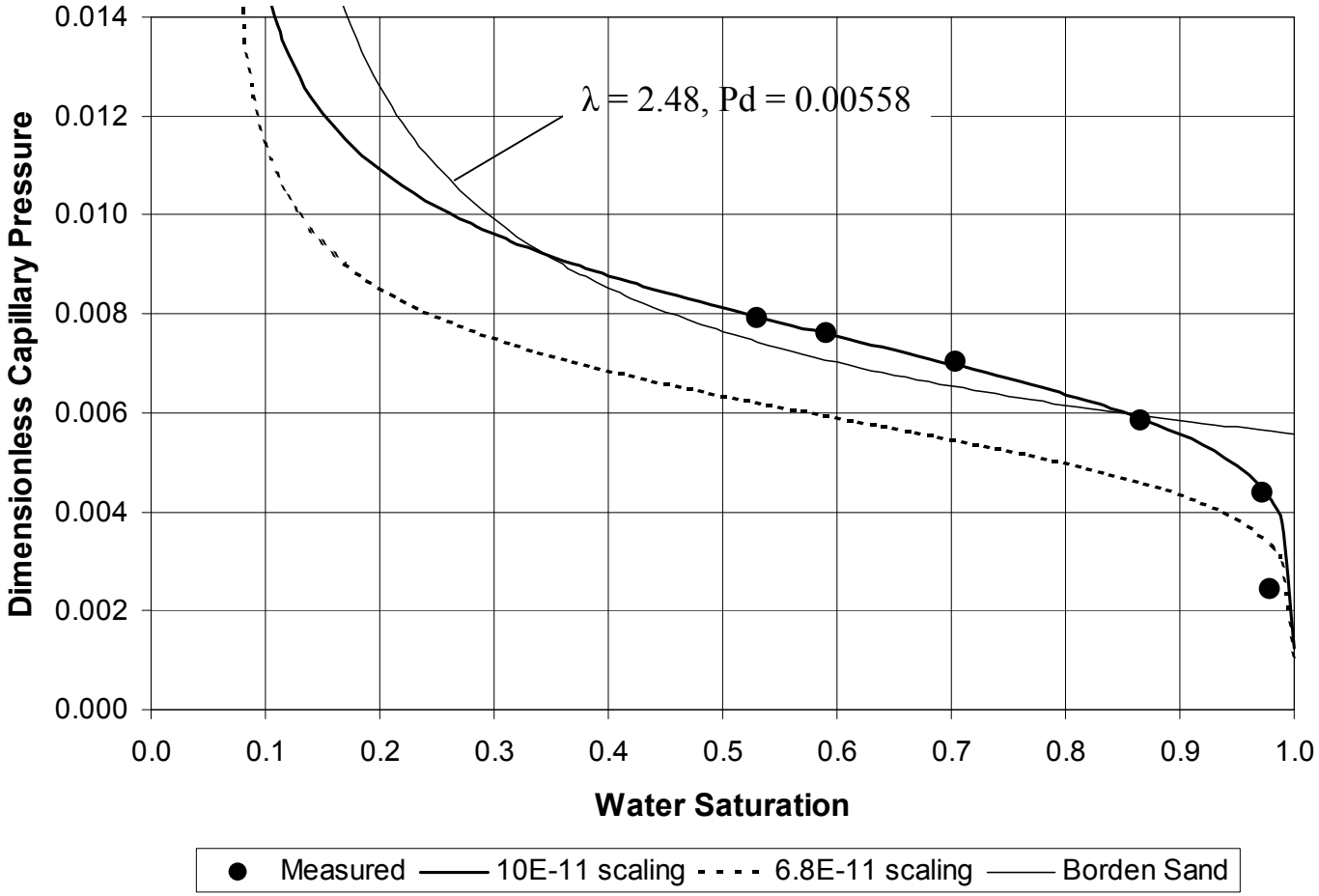

Figure 5.5: Dimensionless measured capillary pressure-saturation curves with two different intrinsic permeabilities for scaling, compared to the dimensionless capillary pressure-saturation curve for the Borden sand using the Brooks-Corey relationship (Kueper and Frind, 1991b).

k_{ref} for the measured sand of 10 x 10^{-11} m^2, an α value of 0.0858, and a β of 0.65 to scale the α value in the Leverett function. Equation 5.6 is incorporated in the inverse multiphase flow simulations to determine the capillary pressure-saturation curves associated with different intrinsic permeability values.

5.5 Inverse Multiphase Flow Simulations

The multiphase flow code T2VOC (Falta and others, 1995; Falta and others, 1992a; Falta and others, 1992b) is used in conjunction with the preprocessor PetraSim from Thunderhead Engineering, facilitating model construction. For the simulation of the Borden PCE spill (Johnson and Poeter, 2003b), the multiphase flow code 3D2PHASE (Gerhard and others, 1998) developed at Queen's University was selected because of the efficiency of the solver. At the time of that research, the preprocessor for T2VOC had not been developed. For the simulation of the laboratory-scale HFE injection, the convenience and availability of a preprocessor outweighs the code efficiency. Computational efficiency is exchanged for the efficiency in setting up the simulation and testing different geometries of permeability zones.

The multiphase-flow simulation domain (Figure 5.6) follows the sand/clay interface and the tank walls in the design of the sand tank (Figures 5.7 and 5.8), creating impermeable boundaries. Cell sizes are generally 12.5 cm^3 with sides ranging from 2 to 2.5 cm, with larger sizes at the edges of the tank. The domain is assumed to be water-saturated; however, GPR data (Johnson and Poeter, 2003a) indicate a thin unsaturated zone at the top of the tank. In the experiment, the water table rises to meet the Plexiglas and water flows from the outlet ports within two minutes after injection starts, so the influence of the unsaturated zone (possibly entrapped air) is assumed to be minimal. The injection cell pressure is specified to be 104,108 Pa to account for the 19.05 cm column of HFE above the sand-filled injection tube, with an assumed saturation of HFE at 0.93

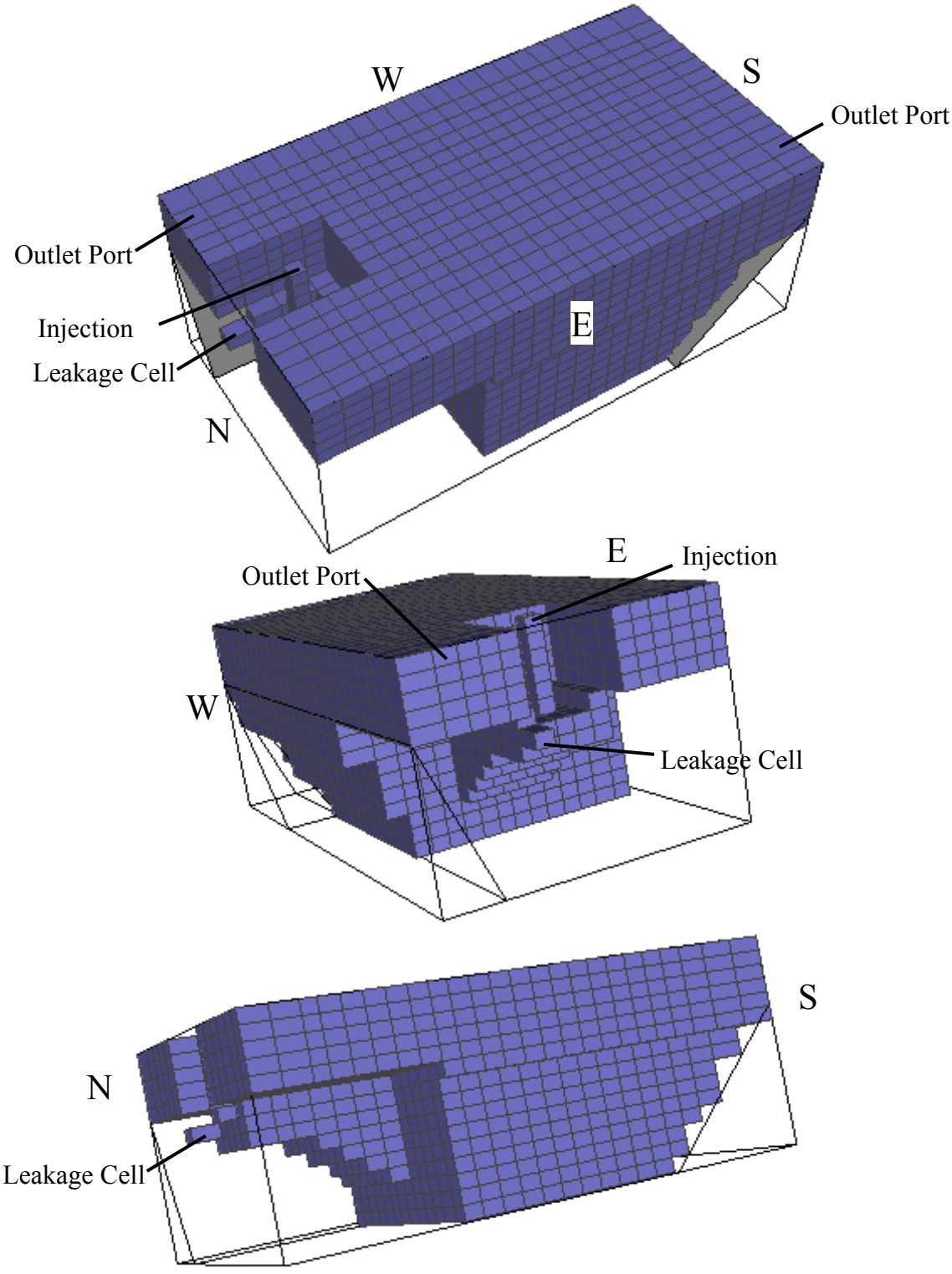

Figure 5.6: Initial multiphase flow simulation grid (inactive cells are white).

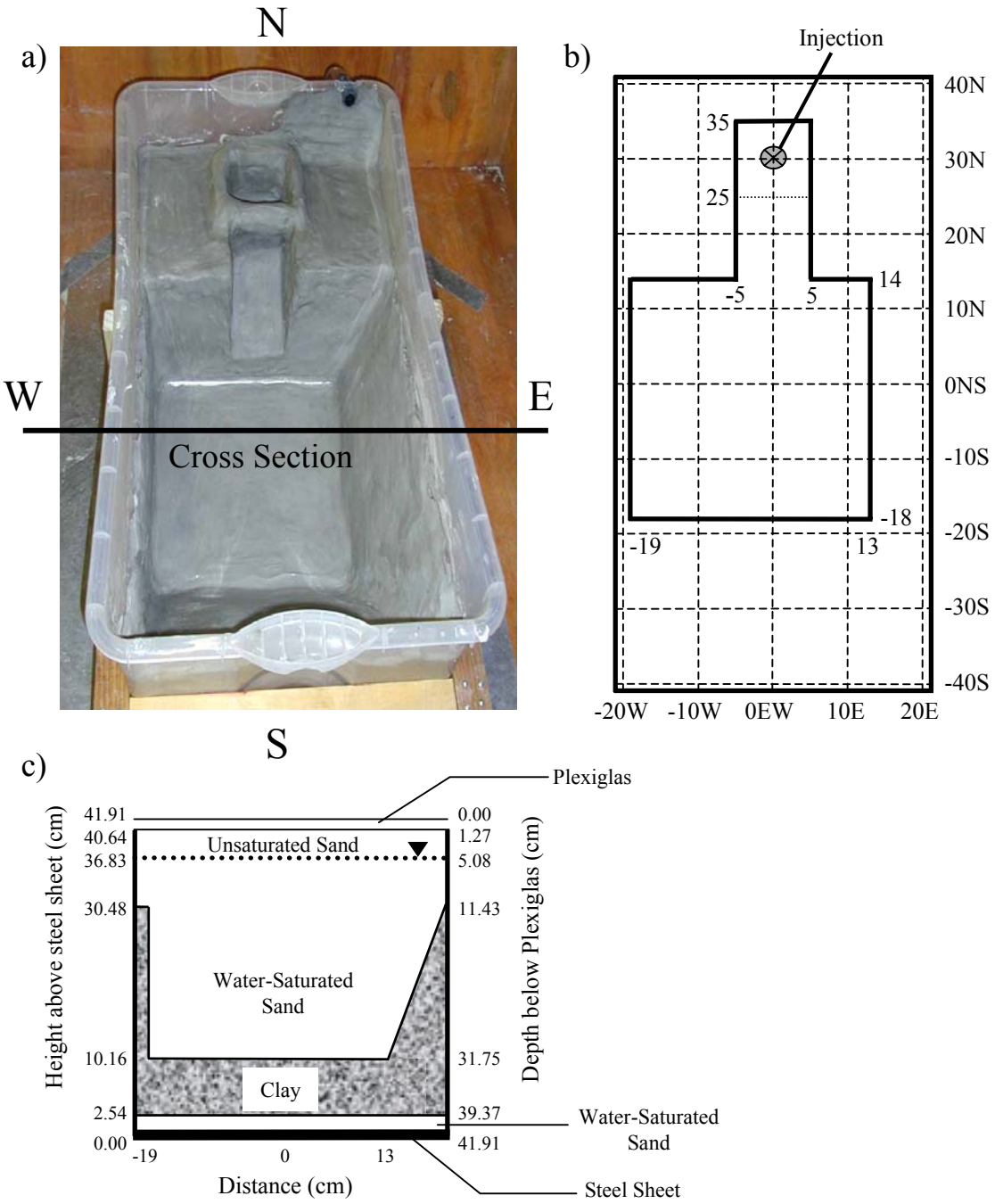

Figure 5.7: Dimensions of sand tank drawn to scale:
a) overhead photo of unfilled tank;
b) overhead dimensions where total tank area is 42 cm x 82 cm; and
c) cross section looking north.

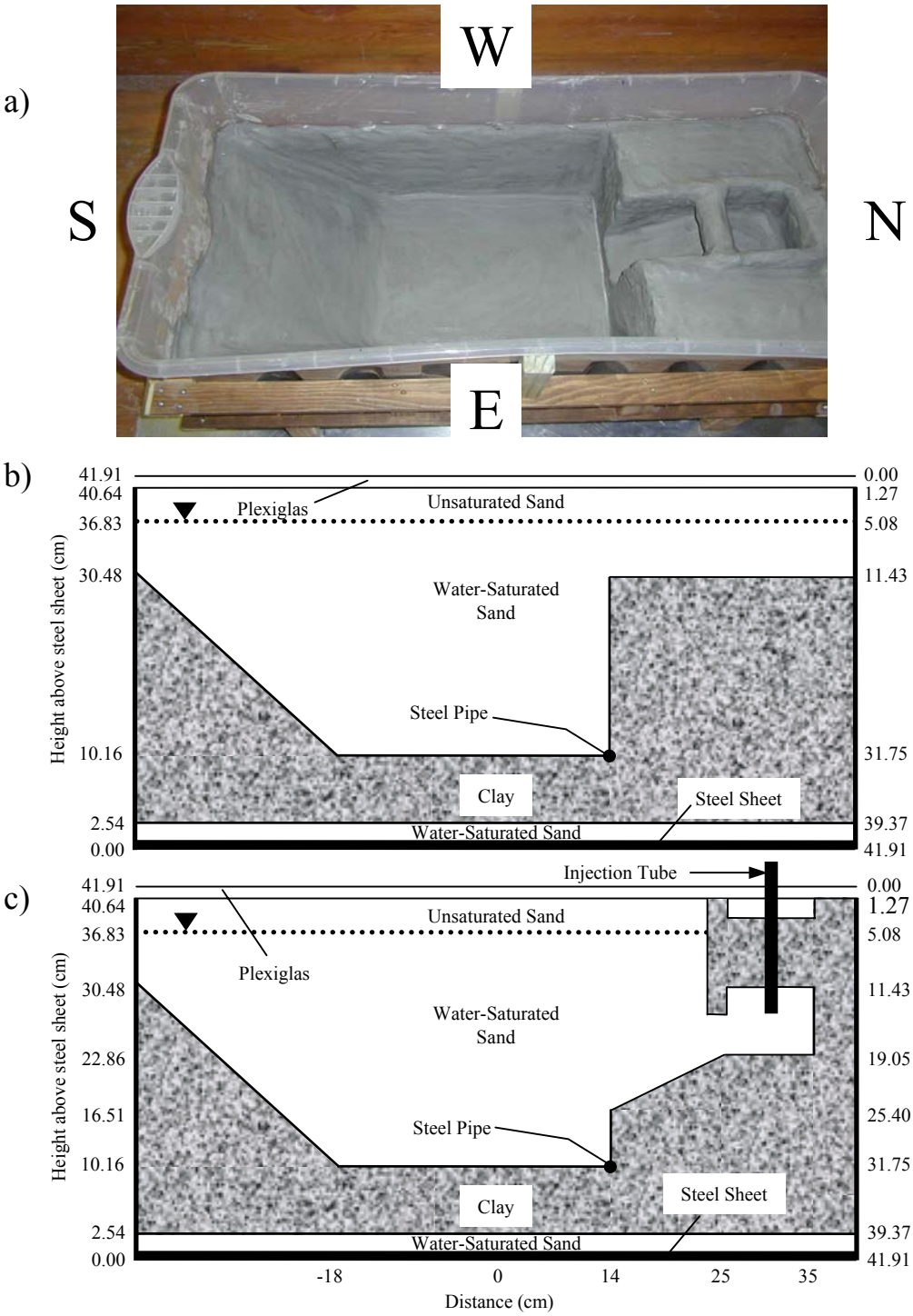

Figure 5.8: Side view of sand tank with dimensions drawn to scale: a) photo of unfilled tank; b) non-center cross section; and c) center cross section.

(or a residual water saturation of 0.07). Two cells represent the outlet ports with a pressure specified as atmospheric using the well-on-deliverability option in T2VOC (see Falta and others, 1992a for details). As the simulated pressure in the cell exceeds the specified pressure, fluid leaves the domain, with a discharge calculated from the pressure difference and the productivity index which represents the skin effect. This index is specified such that the "skin" has the same properties as the sand. An additional well-on-deliverability cell is used next to the clay in the injection zone to represent leakage that occurred in a fracture within the clay, with a pressure controlled by the height of water above the cell.

Model calibration is automated using UCODE (Poeter and Hill, 1998) and follows the same procedure described in Johnson and Poeter (2003b) for the Borden simulation, using residuals and overall fit statistics to evaluate the quality of the conceptual model. Observations of HFE saturations and injection rates with time are used to estimate intrinsic permeability and the productivity index of the leakage through the fracture in the clay. The van Genuchten (1980) capillary pressure-saturation relationship is used in T2VOC via the option of three-phase capillary functions of Parker and others (1987), where gas is specified as immobile, thereby reducing the equations to the original two-phase systems of the van Genuchten equations. Likewise, the relative permeability function uses the three-phase functions of Parker and others (1987), which are obtained from the van Genuchten capillary curve parameters using the procedure of Mualem (1976). The van Genuchten pore size fitting parameter (α) is calculated using the Leverett function via the function file in UCODE with updated permeability values and Equation 5.6. This function file is not needed for the Borden simulations when using 3D2PHASE because this parameter scaling is built into that program.

5.6 Simulation Results

5.6.1 Homogeneous sand tank simulation

An inverted simulation assuming homogeneous sand yields an optimized permeability value of 2.9 x 10^{-11} m^2 for the sand in the tank and a productivity index of 1.3 x 10^{-11} m^3 for the leakage through the clay fracture. This permeability value compares well with the column-measured vertical permeability of 3.4 x 10^{-11} m^2 and the tank-measured permeability of 3.9 x 10^{-11} m^2. The column-measured horizontal permeability of 6.8 x 10^{-11} m^2 is higher than the simulated optimal permeability value, but the measured value is limited in areal extent, thus representing a maximum expected permeability value. In addition, the simulated HFE injection rate is constant, whereas the measured injection rate decreases dramatically with time (Figure 5.9).

HFE saturations are compared as the saturation of HFE in a one square centimeter column of a specified thickness, which provides a value of HFE volume (cm^3) within that column. The measured HFE saturations are slightly greater than the simulated values as indicated by the bias toward positive residuals (measured minus simulated) and the simulated volumes falling below the 45º line in Figure 5.10. Residuals are positively biased at higher HFE volumes (Figure 5.10), but this is more apparent in time and space (Figures 5.11 and 5.12). The front of the free-phase HFE occurs at the correct location and time. However, at later times, the simulation underpredicts the volume of HFE near the injection and overpredicts the amount of HFE at distal locations (Figures 5.11 and 5.12).

The residual bias in space and time indicates that homogeneous sand is not the best conceptual model of the permeability distribution. Although the free-phase HFE front at the sand/clay interface is adequately simulated, the simulation does not show the changing injection rate with time and more HFE mass needs to be retained closer to the injection. Little information is available on the detailed geometry of sand layering within

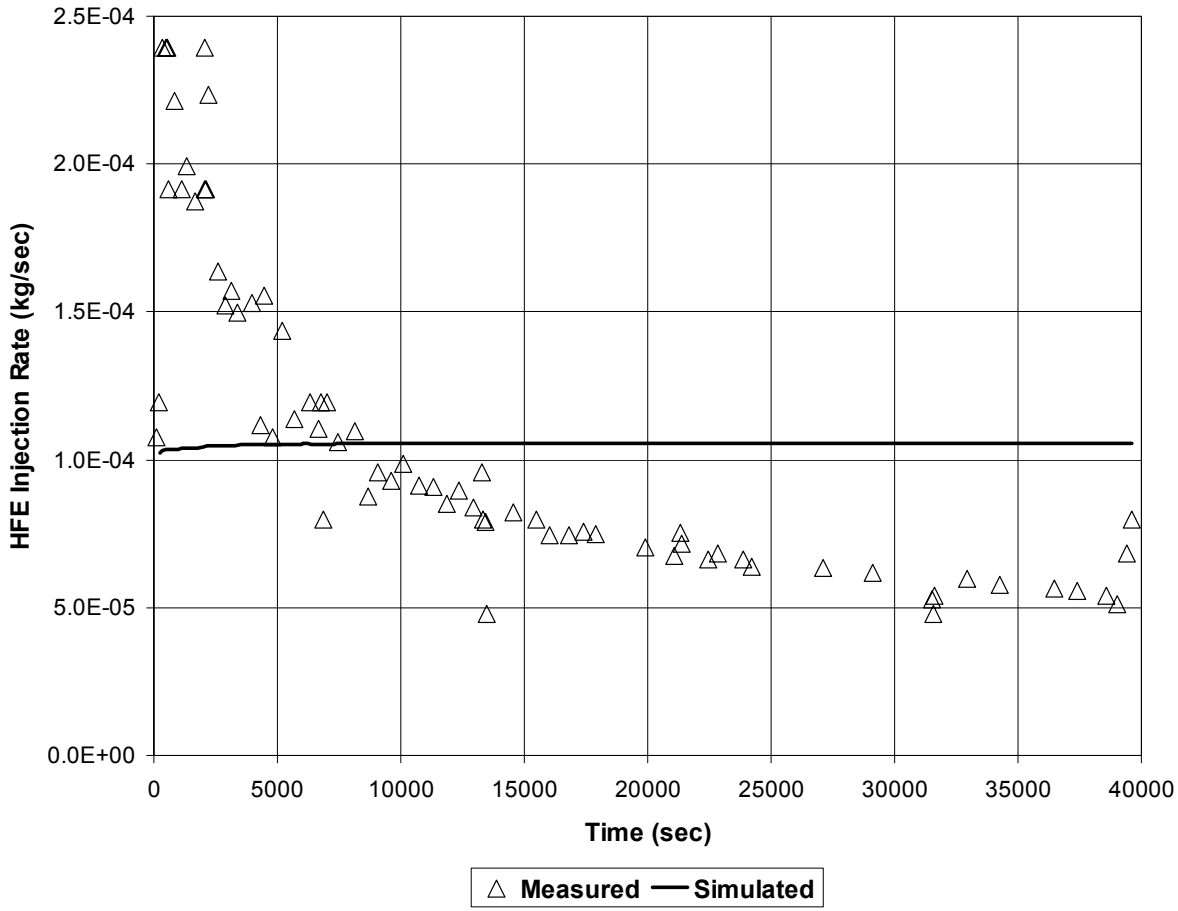

Figure 5.9: Measured and simulated HFE injection rates.

a)

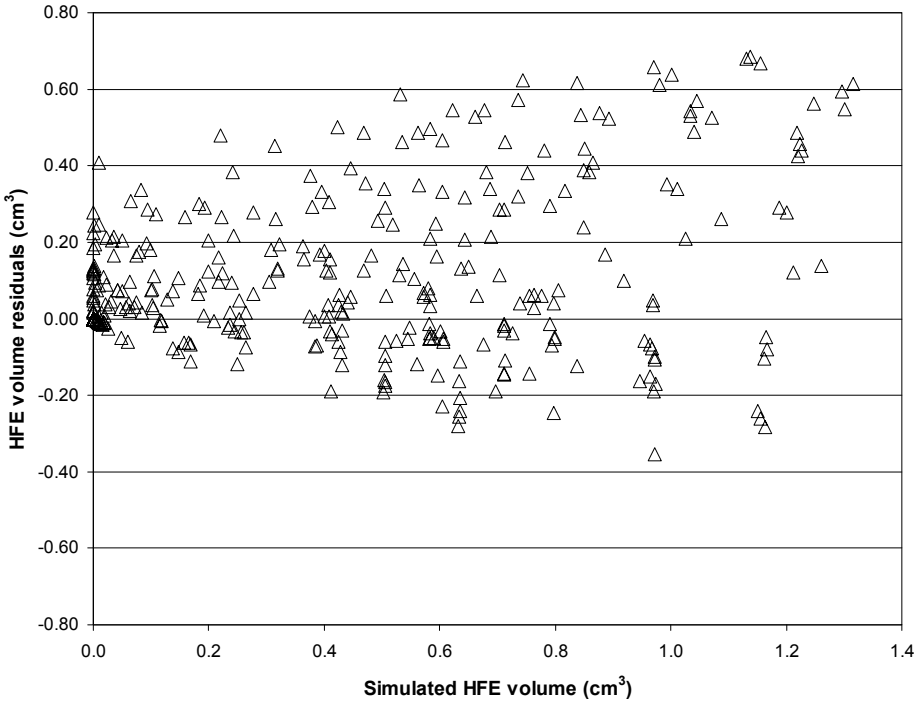

b)

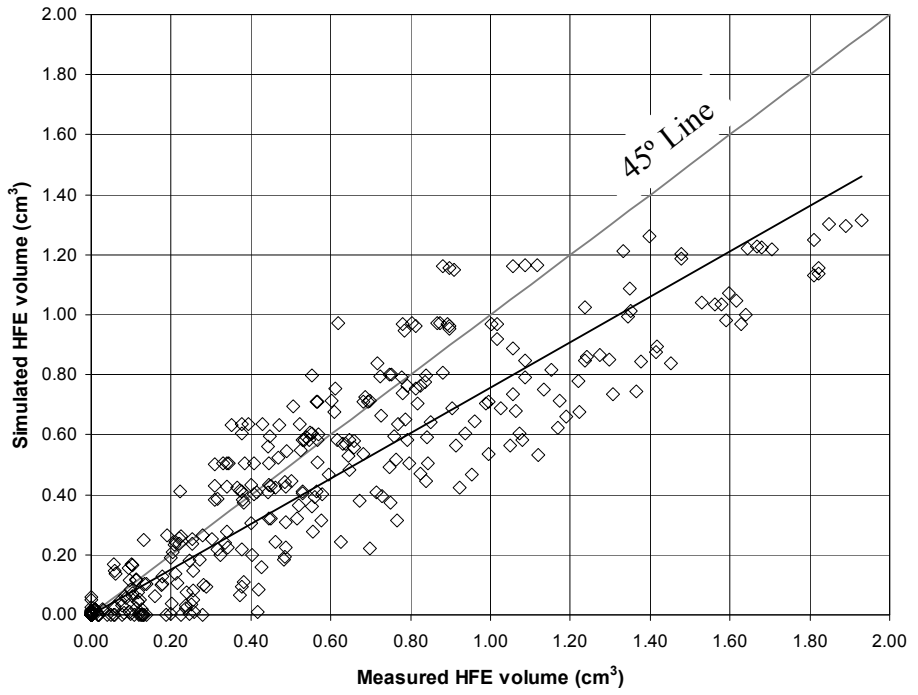

Figure 5.10: Comparison of measured and simulated HFE volumes for the homogeneous sand tank simulation: a) residuals versus measured; and b) simulated versus measured.

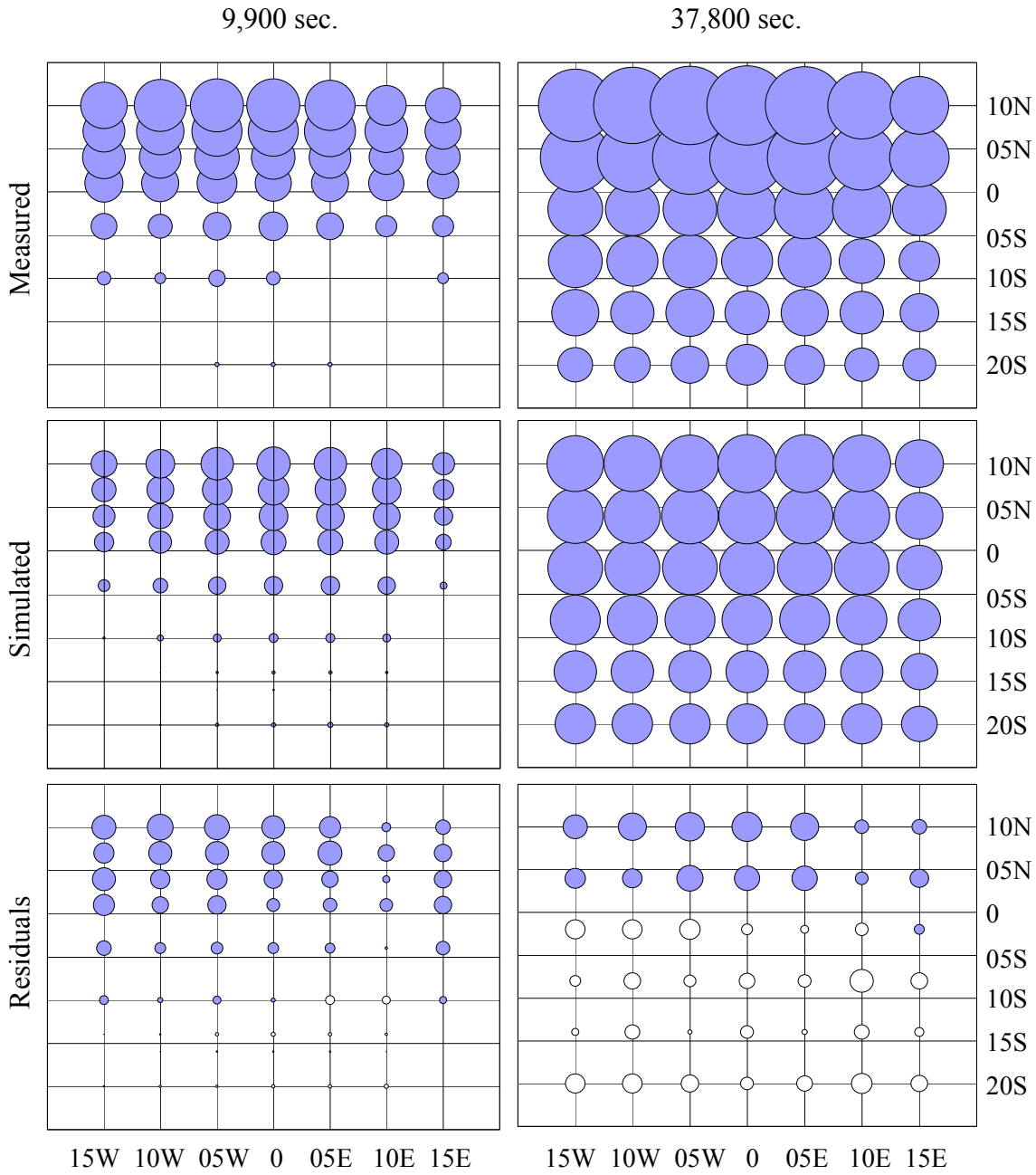

Figure 5.11: Measured, simulated, and residual (measured - simulated) HFE volumes for the homogeneous sand tank simulation at 9,900 seconds and 37,800 seconds. Bubble sizes are proportional. The largest bubble represents 1.93 cm^3 of HFE in a 1 cm^2 column of sand. Coordinate system and injection location are indicated on Figure 5.7b.

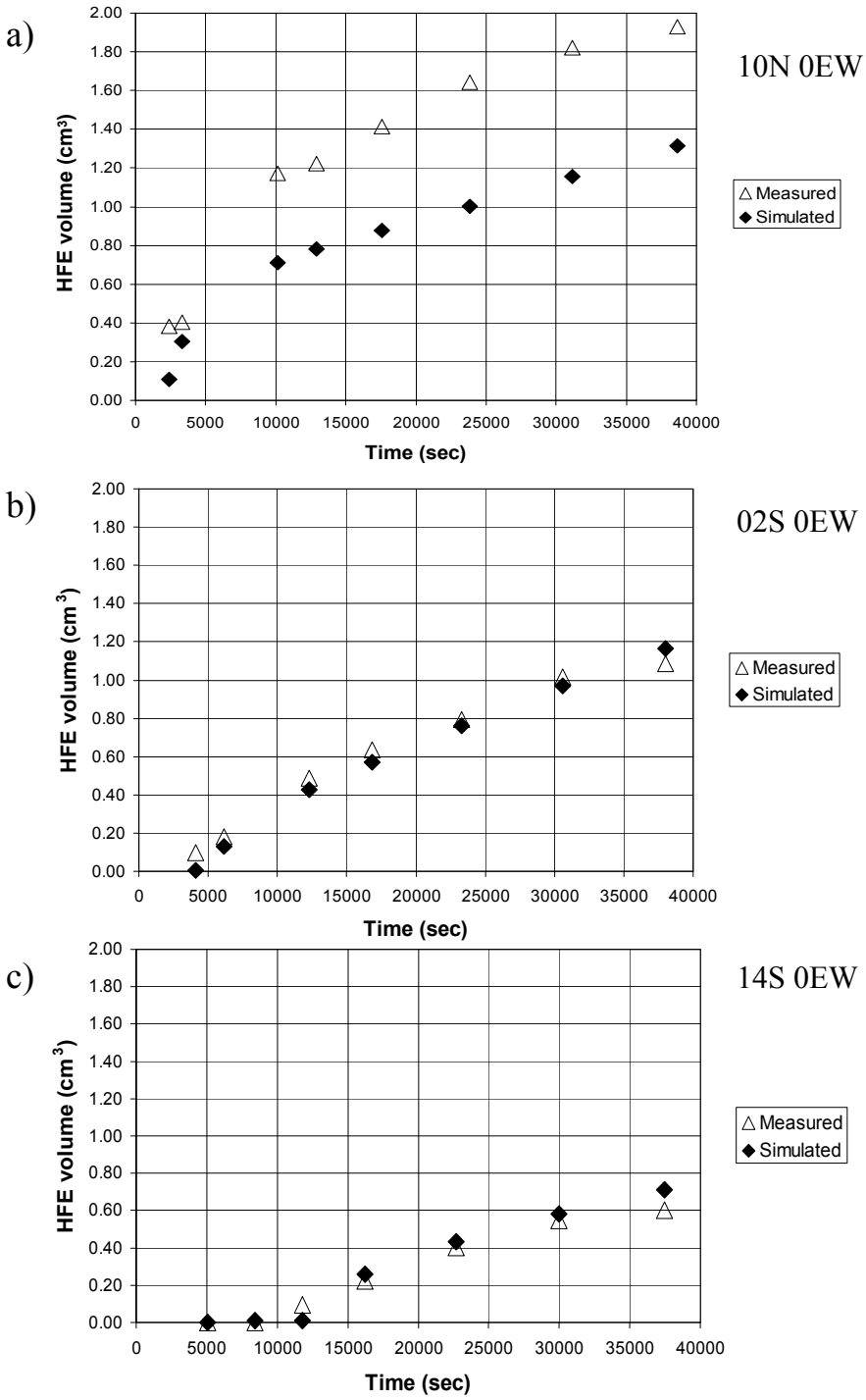

Figure 5.12: Time series graphs of HFE volume (cm^3) at three locations: a) 10N 0EW; b) 02S 0EW; and c) 14S 0EW. The coordinate system and injection location are shown on Figure 5.7b, where 10N 0EW is closest to the source.

the tank, but the inclusion of variable permeability zones is necessary to obtain the observed HFE injection rate and HFE distribution.

5.6.2 Sand layering and T2VOC limitations

Although the #45 Ottawa sand has a narrow grain size distribution, layering of grain sizes occurs as the sand is sifted into the tank through the water (Johnson and Poeter, 2003a). Visual inspection of these layers indicates that coarser-grained sand occurs in lenses that are surrounded by finer-grained sand. Layering is generally horizontal, but sloped slightly in some areas, producing locations where the coarse sand lenses interconnect. HFE flow follows these permeability interfaces, at early times, before the HFE flows along the sand/clay interface (Johnson and Poeter, 2003a). Visual observations of the sand layering and HFE flow patterns indicate a greater correlation length for permeability in the horizontal direction than the vertical direction, consistent with the measured ratio of the horizontal to vertical permeability (2:1). However, the horizontal permeameter tests are limited in extent and may not represent the permeability on the scale of the entire tank. As discussed earlier, the permeability on the centimeter scale may be quite variable. It is difficult to represent this variability in a simulation in which a limited number of cells is necessary to maintain reasonable simulation times, making simulation with a homogeneous, yet anisotropic sand, an attractive alternative.

In T2VOC, different permeability values can be specified in the x, y, and z directions for a "homogeneous" material that exhibits anisotropy. However, for multiphase flow, the DNAPL distribution is primarily dependent on the capillary pressure-saturation relationship and T2VOC does not allow for anisotropy of the capillary pressure-saturation relationship. An inverse multiphase flow simulation gives an overall 10 to 1 anisotropy ratio (horizontal to vertical) for the permeability, but the DNAPL distribution is not affected by the permeability ratio because the median pore-size fitting parameter in

the capillary pressure-saturation relationship could not be scaled along with the permeabilities. This limitation requires the use of cells with different permeability values and appropriately scaled capillary pressure-saturation relationships.

5.6.3 Alternative conceptual models

Three alternative conceptual models are used to explore spatial distributions of permeability that improve the match between simulated and observed injection rates. These configurations are guided by the observed sand layering within the tank, which suggests higher permeability sand lenses surrounded by thin zones of lower permeability sand, and improvements in the calibration with observed HFE injection rates and overall mass distribution. These models are identified as "cube", "modified", and "sub-domain" (Figure 5.13).

The "cube" simulation utilizes fewer cells, resulting in reduced simulation time. It has one injection cell with a constant DNAPL head of 104,000 Pa and an outlet cell set at atmospheric conditions (Figure 5.13a). The total domain is 0.5 m on each side. Thin horizontal and vertical cells (labeled as inner and outer on Figure 5.13a) are set to different permeability values and geometric arrangements in order to analyze the effects on the injection rate. Thin horizontal cells have a permeability of 1×10^{-11} m^2, which inhibits DNAPL entry and thin vertical cells (except at the horizontal crossing) have a higher permeability of 2×10^{-11} m^2. The remaining cells have a higher permeability of different values depending on the numerical experiment. The conceptual model just described is hereafter referred to as the "original" cube model. Slight variations of this geometry yield different injection rates with time (Figure 5.14). The simulation time is limited to 5,000 seconds because of the small domain. The original cube experiment evaluates a permeability of 8×10^{-11} m^2 for the larger cells. The injection rate decreases dramatically at early times (Figure 5.14a). A homogeneous case is also simulated where

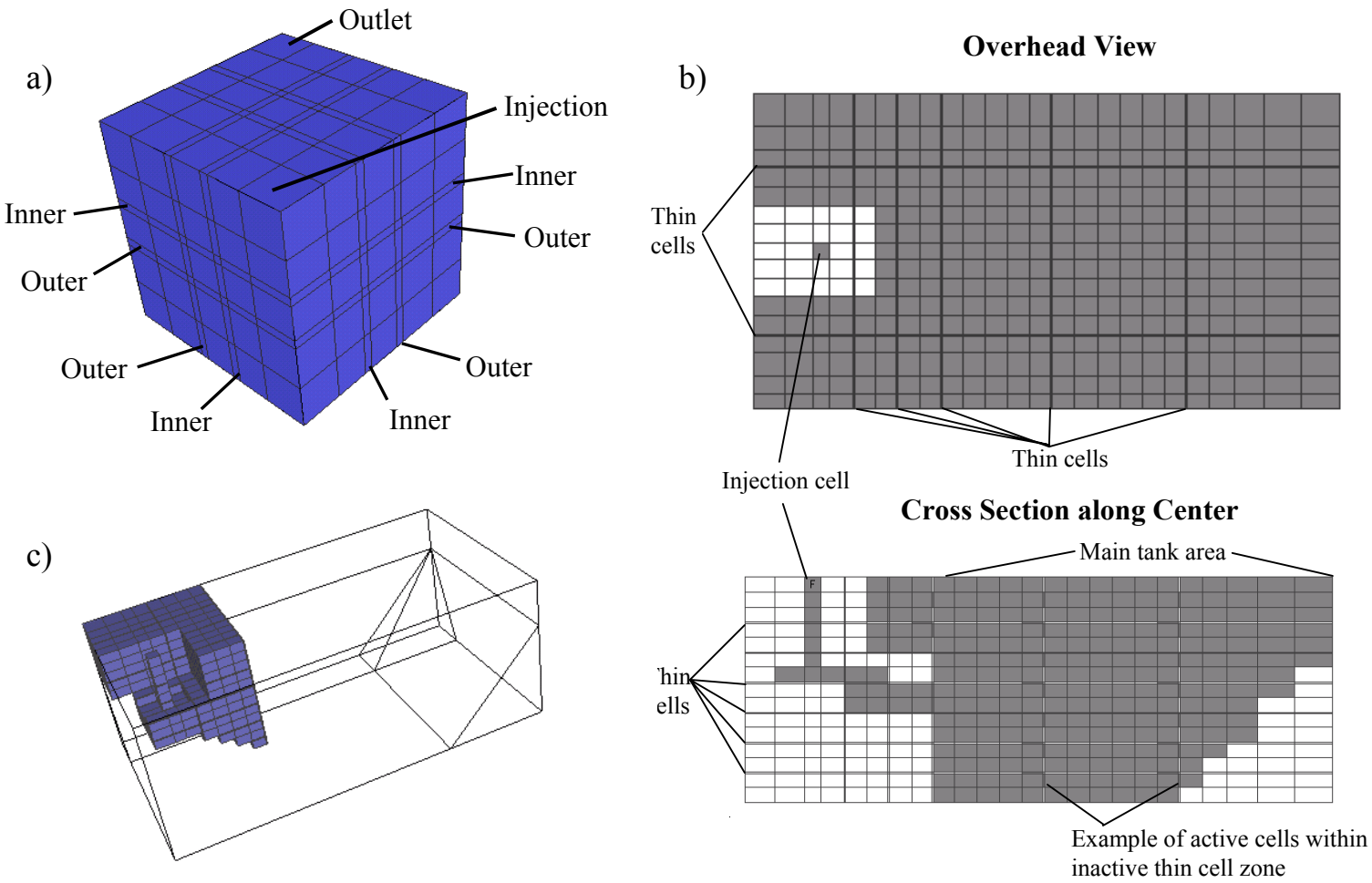

Figure 5.13: Alternate cell and domain layouts: a) test cube; b) modified sand tank simulation; and c) sub-domain of modified sand tank simulation.

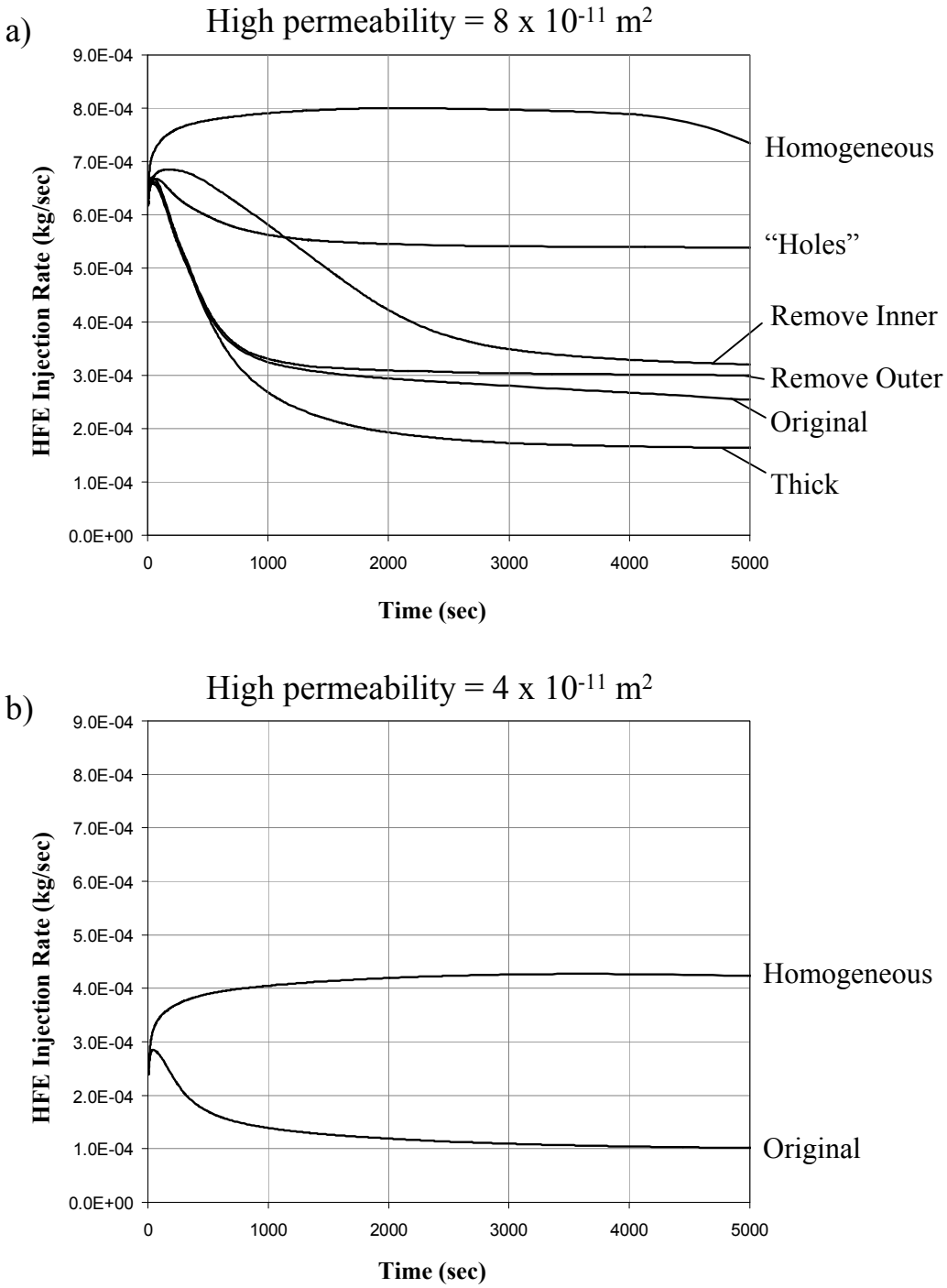

Figure 5.14: Effects of different permeability configurations on HFE injection rates as simulated in the "cube" model.

all the cells are given a permeability of 8×10^{-11} m^2. The injection rate for this case is relatively constant until later times. The slight injection decrease at late time for the homogeneous simulation with a permeability of 8×10^{-11} m^2 occurs because the entire domain fills with DNAPL due to the larger injection rate, which decreases the overall DNAPL injection pressure gradient. With a permeability of 4×10^{-11} m^2 for the larger cells and the entire domain, similar trends occur (Figure 5.14b). In this case, the overall injection rate is lower and the injection rate decline with two permeability zones is less dramatic. Conceptually, the injection rate decrease occurs as the cells close to the injection location fill with DNAPL and result in a decreased pressure gradient near the injection cell.

Additional cases for the "cube" simulation are designed to evaluate the affect of permeability distributions on the HFE injection rate. These include: 1) removing the outer thin-cell "shell" by setting these cells to the same permeability value as the thicker cells; 2) removing the inner thin-cell "shell" in the same manner; 3) creating a thicker overall "shell" by setting the larger cells in between the inner and outer cells to the lower permeability value; and 4) creating "holes" of discontinuity by setting a few of the cells in both the inner and outer "shells" and the horizontal thin cells to the higher permeability value. The results (Figure 5.14a) show that the magnitude of the decreasing injection rate is controlled by the "strength" of the lower permeability zones. This "strength" of the lower permeability zones is controlled by its permeability, thickness, and continuity. That is, the stronger the zone, the greater the decrease in the injection rate. The location of the lower permeability zone influences when the injection rate begins to decrease.

The DNAPL distribution in the various cube simulations is greatly influenced by the strength of the horizontal low permeability barrier. In the homogeneous simulation DNAPL sinks directly to the bottom of the cube, whereas simulations with horizontal low permeability cells do not allow DNAPL to migrate to the bottom of the domain; rather, all of the DNAPL is retained in the top two layers. The "hole" simulation has a DNAPL

distribution throughout the domain, which is also reflected in the intermediate decrease in injection rate.

A similar approach to creating larger blocks of higher permeability sand surrounded by lower permeability sand is used for the full sand tank simulation. The refined grid is shown in Figure 5.13b (called the "modified" model) where the thinner cells are given a lower permeability value. Unfortunately, once DNAPL flows beyond the main injection zone (approximately 10,000 seconds), T2VOC becomes unstable, even with permeability contrasts as low as 2:1. Consequently, the cells in the main tank area (Figure 5.13b) are modified by defining all the thin cells as inactive, except for one active thin cell between each higher permeability block to allow for continued DNAPL flow. This new simulation is referred to as the "modified" sand tank simulation. In addition, a "sub-domain" model simulation (Figure 5.13c) is created by inactivating all of the cells in the main tank area in order to reduce computation time and more easily investigate the affect of the heterogeneous permeability zones on the HFE injection rate. The simulation time for the sub-domain simulation is limited to 10,000 seconds because of the smaller domain. Using a higher permeability of 4×10^{-11} m^2 for the larger cells and 2×10^{-11} m^2 for the smaller cells in both of these new simulations, the HFE injection rates are improved (Figure 5.15), especially for the sub-domain simulation. In the modified sand tank simulation, the injection rate increases slightly and then becomes constant after 5,000 seconds because the DNAPL flow is beyond the low permeability cell zone and into the main tank area with the non-continuous inactive cells. It appears that the openings in the inactive cells are either not small enough, or their permeability is not low enough, to reduce HFE flow, decrease the pressure gradient, and produce a resulting decrease in the HFE injection rate. The HFE distribution indicates that this arrangement of inactive cells retains slightly greater mass near the injection than the homogeneous sand tank simulation.

Although the early time character of the injection rate with time is captured by this new geometric configuration, the late time is not. Yet, the test cube simulations indicate

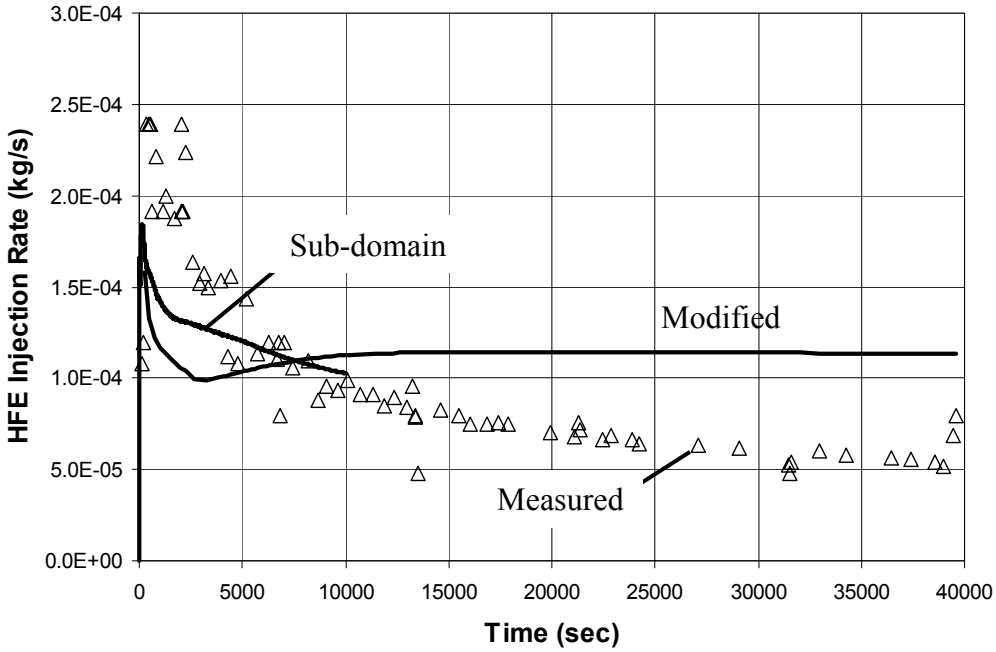

Figure 5.15: Measured HFE injection rates compared to simulated rates for the modified and sub-domain sand tank simulations

that a decreasing injection rate can be simulated with non-unique combinations of the permeability arrangements (thickness and continuity) and the magnitude of permeability contrast. Further improvement in the simulation of observed injection rates and DNAPL saturations requires adjustment of both the fine-scale geometry of units and their associated permeability. Given only the HFE injection rate curve, bulk HFE saturations, and limited observations of layering at the tank walls, the arrangement of permeability zones is difficult to establish and should be incorporated in the inversion process. Computational time using T2VOC for the modified sand tank simulation, which requires a large number of cells to represent the fine-scale geometry and becomes unstable when the permeability contrasts are large, is intensive. Using a personal computer with a 2.53 GHz Pentium 4 processor and 1 GB of RAM, forward simulation time is approximately one day. The simulation time to complete one parameter-iteration, using UCODE, for three parameters is approximately one week. If the simulation converges to a maximum parameter change of 0.01 in 8 to 10 iterations, the full inverse simulation time would be about 2 months. Consequently, further inversion is impractical. Future studies could improve this situation by gathering data to predetermine the geometry of the fine-scaled units, automating the estimation of the placement and size of those units, and developing a more efficient multiphase flow simulator. Without additional data defining the geometry, it is unlikely that the available data contain sufficient information to obtain a unique solution, even with an automated geometric definition and an improved simulator.

5.7 Conclusions

Geometric configuration of fine-scale permeability and their associated capillary pressure-saturation relationships affect the accuracy of simulations. While overall DNAPL flow rates along larger-scaled permeability variations (i.e., sand/clay interface) are adequately predicted using a homogeneous sand, a heterogeneous sand is required to

correctly match the DNAPL injection rates. Fine-scaled geometries of different permeability zones can dramatically change the DNAPL injection rates and mass distributions. Test simulations show the potential for improving the match to the measured DNAPL injection rates using blocks of higher permeability sand surrounded by thin shells of lower permeability sand. This conceptual model is similar to the layering observed in the tank. Estimation of the detailed arrangement of permeability zones and their magnitude requires unreasonable computation times. Future efforts will be improved by more efficient multiphase flow codes, methods that can identify the fine-scaled permeability distribution, and inverse algorithms that can adjust those distributions.

5.8 References

Brooks, R. H., and Corey, A. T., 1966, Properties of porous media affecting fluid flow, *J. Irrig. Drain. Div.*, ASCE, **92**, pp. 61-88.

Demond, A.V. and Roberts, P.V., 1991, Effect of interfacial forces on two-phase capillary pressure-saturation relationships, *Water Resources Research*, 27(3), pp. 423-437.

du Nouy, P.L., 1926, Surface Equilibria of Biological and Organic Colloids; The Chemical Catalog Company, Inc.: New York.

Falta, R. W., Pruess, K., Finsterle, S., and Battistelli, A., 1995, *T2VOC User's Guide*, Lawrence Berkeley Laboratory, LBL-36400.

Falta, R. W., Pruess, K, Javandel, I., and Witherspoon, P. A., 1992a, Numerical modeling of steam injection for the removal of nonaqueous phase liquids from the subsurface, 1. Numerical formulation, *Water resources Research*, **28**(2), pp. 433-449.

Falta, R. W., Pruess, K, Javandel, I., and Witherspoon, P. A., 1992b, Numerical modeling of steam injection for the removal of nonaqueous phase liquids from the subsurface, 2. Code validation and application, *Water resources Research*, **28**(2), pp. 451-465.

Gerhard, J. I., B. H. Kueper, and G. R. Hecox, 1998, The influence of waterflood design on the recovery of mobile DNAPLs. *Ground Water*, **36**(2), pp. 283-292.

Johnson, R. H. and Poeter, E. P., 2003a, Interpreting DNAPL saturations in a laboratory-scale injection with GPR data and direct core measurements, U. S. Geological Survey Open File Report, in review.

Johnson, R. H. and Poeter, E. P., 2003b, Inverse multiphase flow simulation to evaluate conceptual models, estimate intrinsic permeabilities and identify bias in field data, for a field-scale DNAPL injection in Borden sand given time-lapse GPR, in review.

Klute, A. (ed.), 1986, Methods of Soil Analysis Part I, *in* Physical and Mineralogical Methods (2nd edition), Soil Science Society of America, Madison, WI.

Kueper, B. H. and Frind, E. O., 1991, Two-phase flow in heterogeneous porous media: 1. Model development, *Water Resources Research*, **27**(6), pp. 1049-1057.

Leverett, M.C., 1941, Capillary behaviour in porous solids, *Transactions AIME*, **142**, pp. 152-169.

Mualem, Y., 1976, A new model for predicting the hydraulic conductivity of unsaturated porous media, *Water Resources Research*, **12**, pp. 513-522.

Parker, J. C., Lenhard, R. J., and Kuppusamy, T., 1987, A parametric model for constitutive properties governing multiphase flow in porous media*, Water Resources Research*, **23**(4), pp. 618-624.

Paul, G.W. and de Chazal, L.E.M., 1967, *J. Chem. Eng. Data*, **12**(1), pp. 105-107.

Poeter, E. P. and Hill, M. C., 1998, Documentation of UCODE, A computer code for universal inverse modeling, U.S. Geological Survey: Water-Resources Investigations Report 98-4080, 116 p.

van Genuchten, M.T., 1980, A closed-form equation for predicting the hydraulic conductivity of unsaturated soils, *Soil Sci. Soc. Am. J.*, **44**, pp. 892-898.

van Genuchten, M.Th., 1987, Documented Computer Programs – Part 1. USDA-ARS, U.S. Salinity Lab, Riverside, CA.

Chapter 6

SUMMARY, CONCLUSIONS AND FIELD-SCALE APPLICATIONS

6.1 Summary and Conclusions

The goal in using GPR data to calibrate inverse multiphase flow simulations is to adequately characterize subsurface DNAPL movement. Prediction of DNAPL flow is improved through the coupled use of the GPR interpretation and inverted multiphase flow simulations. In most cases, inversion statistics and bias in residuals indicate error in the conceptual models when the observations are straightforward, but uncertain, measurements. For this research, inversion statistics and bias in the residuals are used to create more accurate conceptual models of the location of permeability contrasts and the capillary pressure-saturation functions. However, because the observations of DNAPL saturations are determined using geophysical modeling, bias in the residuals can remain if the GPR interpretation is biased by multidimensional influences. As a result, inversion statistics are a good tool for identifying both possible areas of interference in the GPR interpretation and errors in the conceptual models. The conclusions from the four related investigations (Chapters 2, 3, 4 and 5) that addressed the given objective and lead to the results summarized above are presented below, along with a guide for applying the presented procedures to future field-scale investigations.

Chapter 2 demonstrates that the Bruggeman-Henai-Sen mixing model can be applied successfully to a three-material system with air, water and sand. For accuracy, an iterative BHS model with an air/water/sand system must consider which two-material end member (air/sand or water/sand) to use as the matrix. For a given porosity, a new weighted BHS model provides the best match to measured data. Two BHS curves, one

with air/sand as the matrix and one with water/sand as the matrix, are weighted based on the water saturation.

In Chapter 3, synthetic test cases show that saturation data alone are sufficient to estimate optimal intrinsic permeability values when other model parameters are known. However, the character and magnitude of error in the observation data are critical to accurately estimating permeability values. If observation errors indicate physically improbable trends in the dependent variable (e.g., DNAPL saturation decreases with time during constant injection) at critical locations, or the errors are large, then permeability values will not be accurately estimated. Synthetic simulations of the Borden injection illustrate that artificially biased observation data produce biased residuals similar to those observed in this evolution of conceptual models, yet still produce accurate optimal permeability values. Accurate optimal permeability values are also produced in a case where no channel observations are provided. These findings indicate that the resulting optimal permeability values are not substantially influenced by bias in the observation data within the channel. Exploration of the source of residual bias using flow simulation experiments, GPR modeling experiments, and laboratory experiments, reveal that DNAPL saturations are overestimated in the channel due to GPR ray focusing which results in biased residuals in flow model calibration. Reasonable optimized permeability values (based on laboratory measurements of core samples) are estimated for all conceptual models, but the effort to improve fit and reduce residual bias yielded optimal permeability values closer to the field measurements. Consequently, an effort to improve model fit and reduce residual bias is useful in decreasing conceptual model error even though it cannot compensate for bias in observations. The remaining bias can then be used as a tool to identify possible errors in the observations, especially when the bias in observation data is difficult to assess. In this way, the use of inverse multiphase flow simulations provides a unique opportunity for improving the GPR interpretation.

In Chapter 4, the collection of GPR data over a DNAPL spill zone efficiently produces a detailed image of the bulk DNAPL distribution in time and space. GPR data

can be used to quantitatively determine the volume of DNAPL as indicated by interpretation of GPR response to a DNAPL spill (HFE) in a small sand tank. This was achieved using the two-way travel time of radar waves reflected from a steel sheet placed below the sand tank, where increasing DNAPL volumes are indicated by decreasing travel times. The known depth to the steel sheet allows for the calibration of the permittivity of the intervening material based on the arrival time of the steel sheet reflection. One-dimensional GPR modeling of the DNAPL sub-layers within a specified thickness was non-unique due to an absence of data and a reliance upon reflection amplitudes; thus, identification of varying DNAPL saturation with depth could not be achieved. Two- and three-dimensional influences within the tank were minimal, except in the southeast corner of the tank, where the intersection of the sloping clay walls produced an amplified reflection of the DNAPL zone. This multidimensional nature of GPR data biased the results from 1D GPR modeling because the tank walls influenced the reflection from the sand/clay interface. Chapter 4 confirms that biased DNAPL saturations calculated from 1D GPR model calibration (Sneddon and others, 2002) and used for a multiphase flow model calibration in Chapter 3 are likely due to 2D influences within a channel that are not accounted for in the 1D GPR modeling. For a field setting where a DNAPL spill has already occurred, the identification or careful emplacement of targets (i.e., steel pipes, steel sheets, underground conduits, and geologic features) with a known depth can improve the GPR interpretation. A target placed in areas where DNAPL is not present can be used to obtain permittivity of the natural materials at the site. The DNAPL volume above a target can be calculated by calibrating a 1D GPR model to the depth of the known feature. Flat lying targets are ideal, but other target configurations could also be used if their position is known and multidimensional influences are appropriately modeled.

In Chapter 5, the knowledge of fine-scaled variations in permeability is important to simulating and understanding multiphase flow in a laboratory-scale DNAPL injection. These fine-scaled variations affect the permeability values used to scale capillary

pressure-saturation relationships and affect the accuracy of simulations. While the overall front of free-phase DNAPL flow rates along larger-scaled permeability variations (i.e., sand/clay interface) are adequately predicted using a homogeneous sand, a heterogeneous sand is required to correctly match the DNAPL injection rates. Fine-scaled geometries of different permeability zones can dramatically change the DNAPL injection rates and mass distributions. Test simulations show the potential for improving the match to the measured DNAPL injection rates using blocks of higher permeability sand surrounded by thin shells of lower permeability sand. However, estimation of the detailed arrangement of permeability zones and their magnitude requires unreasonable computation times with non-unique results. Future efforts will be improved by more efficient multiphase flow codes, methods that can identify the fine-scaled permeability distribution, and inverse algorithms that can adjust those distributions.

6.2 Future Field-scale Applications

Future field-scale research with the use of GPR data and inverse multiphase flow simulations can include: 1) characterization and prediction of DNAPL flow during a controlled or uncontrolled release; 2) identification of the DNAPL distribution after it has reached a near static condition; 3) prediction of DNAPL movement during remediation efforts, and 4) identification of DNAPL movement with GPR during remediation.

The strength of using GPR as a characterization technique in a field setting is the avoidance of using direct detection, such as core holes, which can remobilize DNAPLs. In addition, GPR images provide much greater spatial detail in an efficient manner. At a DNAPL spill site, GPR data can be used in conjunction with any existing data from well logs or core holes. Existing data will clarify the interpretation of reflections seen in the GPR images and will assist in the determination of whether or not reflections are related to geology or DNAPLs. Even if no existing data are available, using GPR first before

installing any core holes will reduce the risk of DNAPL remobilization. After a GPR survey is conducted, the GPR data can be used as a guide for the installation of monitoring wells and/or core holes based on the interpreted location of the DNAPL source zones. These additional direct coring methods will then verify that the GPR data is interpreted correctly and will allow for a more efficient design of remedial strategies.

Successful use of GPR surveys at uncontrolled field-scale sites will depend on the nature of the DNAPL distribution and the quality of subsurface characterization, including a unique interpretation of reflective materials. In general, the maximum depth of penetration for GPR waves is approximately 3 to 5 m, which will vary depending on the electrical conductivity of the subsurface (higher electrical conductivity reduces the penetration depth) and the frequency of the GPR antenna. Lower frequency antennas have a greater penetration depth than higher frequency antennas in the same material. However, lower frequency antennas produce images with a lower resolution and the GPR signal is more prone to a reduction in penetration depth due to high electrical conductivities of the subsurface materials. In addition, multidimensional influences in the GPR data must be interpreted correctly. At the present time, use of 1D GPR modeling programs can be practically applied to quantitatively interpret GPR data. Geophysicists are presently developing 2D and 3D GPR modeling techniques that will quantitatively account for multidimensional influences when the geometry is known. These future procedures will use techniques developed for seismic wave reflection interpretations (Powers, 2003).

Accurate identification of DNAPL source zones with GPR and prediction of DNAPL movement with multiphase flow simulations will depend upon the geometry of subsurface permeability contrasts. At a site where DNAPL pools on relatively flat, large-scale permeability contrasts, the characterization of the DNAPL distribution and the predictions of DNAPL movement are likely to be successful as long as the geometry is known. DNAPL pools on large-scale permeability contrasts with sloping or variable elevation interfaces could also be successfully characterized, but would require contact

depth information and a GPR interpretation that accounts for multidimensional influences. At a site where DNAPL exists in zones controlled by fine-scale variations in permeability, the unique determination of fine-scaled variations in DNAPL saturations with depth will be limited without additional data. However, using GPR data and appropriate known-depth targets, the spatial distribution of bulk DNAPL volumes can be accurately determined using the procedures discussed in Chapter 5. Prediction of future DNAPL movement under remedial scenarios with multiphase flow simulations will depend upon the knowledge of the detailed geometry of fine-scale permeability distributions and their relative location to large-scale variations. Resulting influences on DNAPL flow could be simulated using a variety of conceptual models of permeability distributions based on available information. Finally, the actual progress of any applied remedial strategies can be continuously monitored using GPR. Changes in DNAPL distributions will be seen in the GPR images and reductions in DNAPL saturations with time can be monitored using a series of GPR images through time.

REFERENCES

ASTM, 1998, Standard test methods for AC loss characteristics and permittivity (dielectric constant) of solid electrical insulation, ASTM method D-150, 19 p.

Bolha, J., 1986, A sedimentological investigation of a prograding foreshore sequence: C.F.B. Borden, M.Sc. Thesis, University of Waterloo, Waterloo, Ontario, Canada.

Brewster, M. L., Annan, A. P., Greenhouse, J. P., Kueper, B. H., Olhoeft, G. R., Redman, J. D. and Sander, K. A., 1995, Observed migration of a controlled DNAPL release by geophysical methods: *Ground Water*, **33**, pp. 977-987.

Brooks, R. H., and Corey, A. T., 1966, Properties of porous media affecting fluid flow, *J. Irrig. Drain. Div.*, ASCE, **92**, pp. 61-88.

Bruggeman, D. A. G., 1935, Berechnung verschiedener physikalischer konstanten von hetarogenen substanzen: *Ann. Phys. Lpz.*, **24**, p. 636-679.

Canan, Birsen, 1999, Dielectric properties of mixtures of clay-water-organic compounds, M.Sc. Thesis, Dept. of Geophysics, Colorado School of Mines, Golden, 332 p.

Demond, A.V. and Roberts, P.V., 1991, Effect of interfacial forces on two-phase capillary pressure-saturation relationships, *Water Resources Research*, **27**(3), pp. 423-437.

Doherty, J., PEST: Corinda, Australia, Watermark Computing, 122 p., 1994.

du Nouy, P.L., 1926, Surface Equilibria of Biological and Organic Colloids; The Chemical Catalog Company, Inc.: New York.

Falta, R. W., Pruess, K., Finsterle, S., and Battistelli, A., 1995, *T2VOC User's Guide*, Lawrence Berkeley Laboratory, LBL-36400.

Falta, R. W., Pruess, K, Javandel, I., and Witherspoon, P. A., 1992a, Numerical modeling of steam injection for the removal of nonaqueous phase liquids from the subsurface, 1. Numerical formulation, *Water resources Research*, **28**(2), pp. 433-449.

Falta, R. W., Pruess, K, Javandel, I., and Witherspoon, P. A., 1992b, Numerical modeling of steam injection for the removal of nonaqueous phase liquids from the subsurface, 2. Code validation and application, *Water resources Research*, **28**(2), pp. 451-465.

Gerhard, J. I., B. H. Kueper, and G. R. Hecox, 1998, The influence of waterflood design on the recovery of mobile DNAPLs. *Ground Water*, **36**(2), pp. 283-292.

Greenhouse, J., Brewster, M., Schneider, G., Redman, D., Annan, P., Olhoeft, G.,Lucius, J., Sander, K. and Mazzella, A., 1993, Geophysics and solvents: The Borden experiment, *Leading Edge*, **12**(4), pp. 261-267.

Hanai, T., 1968, Electrical properties of emulsions, *in* Sherman, P., Ed., Emulsion science, Academic Press.

Hasted, J. B., 1973, *Aqueous dielectrics*, London, Chapman & Hall, 302 p.

Hill, M. C., 1992, A computer program (MODFLOWP) for estimating parameters of a transient, three-dimensional, ground-water flow model using nonlinear regression, U.S. Geological Survey Open File Report 91-484, 102 p.

Hill, M. C., 1998, Methods and guidelines for effective model calibration, U.S. Geological Survey Water-Resources Investigations Report 98-4005, 90 p.

Hill, M.C., Banta, E.R., Harbaugh, A.W., and Anderman, E.R., 2000, MODFLOW-2000, the U.S. Geological Survey modular ground-water model -- User guide to the Observation, Sensitivity, and Parameter-Estimation Processes and three post-processing programs: U.S. Geological Survey Open-File Report 00-184, 210 p.

Huang, F. S. C., and Shen, L. C., 1983, Analysis of error due to presence of gaps in the measurement of rock samples in a coaxial line, *Geophysics*, **48**, pp. 206-212.

Johnson, R. H. and Poeter, E. P., 2003b, Inverse multiphase flow simulation to evaluate conceptual models, estimate intrinsic permeabilities and identify bias in field data, for a field-scale DNAPL injection in Borden sand given time-lapse GPR, in review.

Johnson, R. H. and Poeter, E. P., 2003 in Chapters 2 and 3, 2003a in Chapter5, Interpreting DNAPL saturations in a laboratory-scale injection with GPR data and direct core measurements, U. S. Geological Survey Open File Report, in review.

Johnson, R. H. and Poeter, E. P., 2003b in Chapter 4, Accuracy of the iterative use of the Bruggeman-Hanai-Sen mixing model to determine the proportions of a mixture of water, air and sand, in review.

Klute, A. (ed.), 1986, Methods of Soil Analysis Part I, *in* Physical and Mineralogical Methods (2nd edition), Soil Science Society of America, Madison, WI.

Kueper, B. H. and Frind, E. O., 1991a, Two-phase flow in heterogeneous porous media: 1. Model development, *Water Resources Research*, **27**(6), pp. 1049-1057.

Kueper, B. H. and Frind, E. O., 1992a, Two-phase flow in heterogeneous porous media: 2. Model application, *Water Resources Research*, **27**(6), pp. 1057-1070.

Kutrubes, D. L., 1986, Dielectric permittivity measurements of soils saturated with hazardous fluids: M.Sc. Thesis, Dept. of Geophysics, Colorado School of Mines, Golden, 300 p.

Leverett, M.C., 1941, Capillary behaviour in porous solids, *Transactions AIME*, **142**, pp. 152-169.

Lucius, J. E. and Powers, M.H., 1997, Multi-frequency GPR surveys, *in* SAGEEP '97 Proceedings, Symposium on the Application of Geophysics to Environmental and Engineering Problems, Environmental and Engineering Geophysics Society, **1**, pp. 355-364.

Mualem, Y., 1976, A new model for predicting the hydraulic conductivity of unsaturated porous media, *Water Resources Research*, **12**, pp. 513-522.

McCray, J.E. and Brusseau, M.L, 1998, Cyclodextrin-enhanced in-situ flushing of multiple-component immiscible organic-liquid contamination at the field scale: Mass removal effectiveness, *Environ. Sci. Tech*., **32**(9), pp. 1285-1293.

National Research Council (NRC), 1994, *Alternatives for Ground Water Cleanup*, National Academy Press, Washington, D. C.

Olhoeft, G.R., 1981, Electrical properties of rocks, *in* Physical Properties of Rocks and Minerals, in Touloukian, Y. S., Judd, W. R., and Roy, R. F., eds., New York, McGraw-Hill, pp. 257-330.

Olhoeft, G.R., 1987, Electrical properties from 10-3 to 10+9 Hz --physics and chemistry, *in* Physics and Chemistry of Porous Media II, American Institute of Physics Conf. Proc. 154, Ridgefield, CT, 1986, J.R. Banavar, J. Koplik, and K.W. Winkler, eds., NY, AIP, pp. 281-298.

Olhoeft, G. R., 1998, GRORADAR™: Acquisition, processing, modeling, and display of ground penetrating radar data: ver. 4.0, software distributed on CD-ROM at Seventh International Conference on Ground Penetrating Radar, (http://g-p-r.com).

Parker, J. C., Lenhard, R. J., and Kuppusamy, T., 1987, A parametric model for constitutive properties governing multiphase flow in porous media, *Water Resources Research*, **23**(4), pp. 618-624.

Paul, G.W. and de Chazal, L.E.M., 1967, *J. Chem. Eng. Data*, **12**(1), pp. 105-107.

Poeter, E.P. and M.C. Hill, 1996, Unrealistic parameter estimates in inverse modeling: A problem or a benefit?, Proceedings of ModelCare'96, Golden CO, IAHS/AISH Publication, pp. 277-286.

Poeter, E. P. and Hill, M. C., 1997, Inverse models: A necessary next step in groundwater modeling, *Ground Water*, **33**(6), pp. 889-904.

Poeter, E. P. and Hill, M. C., 1998, Documentation of UCODE, A computer code for universal inverse modeling, U.S. Geological Survey: Water-Resources Investigations Report 98-4080, 116 p.

Powers, M.H., 1995, Dispersive ground penetrating radar modeling in 2D: Ph.D. Thesis T-4820, Colorado School of Mines, Golden, CO, 198 p.

Powers, M.H., 1997, Modeling frequency-dependent GPR, *Leading Edge*, **16**(11), pp. 1657-1662.

Powers, M.H., 2003, Personal communication.

Powers, M. H., Duke, S. K., Huffman, A. C., and Olhoeft, G. R., 1992, GPRMODEL: One dimensional full waveform forward modeling of ground penetrating radar data, U.S. Geological Survey Open File Report 92-532, 22 p. + floppy disk.

Powers, M. H. and Olhoeft, G. R., 1995, GPRMODV2: one-dimensional full waveform forward modeling of dispersive ground penetrating radar data, version 2.0: U. S. Geological Survey Open File Report 95-58, 41 p. + floppy disk.

Rathfelder, K., and Abriola, L. M., 1998, The influence of capillarity in numerical modeling of organic liquid redistribution in two-phase systems, *Adv. Water Resour*., **21**(2), pp. 159-170.

Redman, J. D., 1992, Geophysics and the solvents-in-groundwater program, *in* Proc. of the Symposium on the Application of Geophysics to Engineering and Environmental Problems, April 26-29, Oakbrook, Illinois, **2**, Society of Engineering and Mineralogy, Golden, CO, pp. 375-382.

Redman, J. D., and Kueper, B. H., 1992, Core permeability data, University of Waterloo and Queen's University, Internal Document.

Sander, K.A., 1994, Characterization of DNAPL movement in saturated porous media using ground penetrating radar, Colorado School of Mines, Master's Thesis, ER-4336.

Sander, K. A., and Olhoeft, G. R., 1994, 500-MHz ground penetrating radar data collected during an intentional spill of tetrachloroethylene at Canadian Forces Base Borden in 1991, USGS Digital Data Series DDS-25, CD ROM.

Sihvola, A. H., 1999, Electromagnetic mixing formulas and applications, *IEEE electromagnetic waves series*, **47**, Institution of Electrical Engineers, London.

Sen, P. N., Scala, C., and Cohen, M. H., 1981, A self-similar model for sedimentary rocks with application to the dielectric constant of fused glass beads, *Geophysics*, **46**, pp. 781-795.

Sneddon, K. W., Powers, M. H., Johnson, R. H., and Poeter, E. P., 2002, Modeling GPR data to interpret porosity and DNAPL saturations for calibration of a 3-D multiphase flow simulation, U.S. Geological Survey Open File Report: 02-451, 29 p.

Sudicky, E. A., 1986, A natural gradient experiment on solute transport in a sandy aquifer: Spatial variability of hydraulic conductivity and its role in the dispersion process, *Water Resources Research*, **22**(13), pp. 2069-2082.

Topp, G. C., Davis, J. L., and Annan, A. P., 1980, Electromagnetic determination of soil water content: Measurements in coaxial transmission lines, *Water Resources Research*, **16**, pp. 574-582.

Turcke, M.A. and Kueper, B.H., 1996, Geostatistical analysis of the Borden aquifer hydraulic conductivity field, *Journal of Hydrology*, **178**, pp. 223-240.

van Genuchten, M.T., 1980, A closed-form equation for predicting the hydraulic conductivity of unsaturated soils, *Soil Sci. Soc. Am. J.*, **44**, pp. 892-898.

van Genuchten, M.Th., 1987, Documented Computer Programs – Part 1. USDA-ARS, U.S. Salinity Lab, Riverside, CA.

von Hippel, A. R., 1954, *Dielectric materials and applications*, NY, Wiley and Sons, Inc. 438 p.